MICROWAVE-FREQUENCY CHARACTERIZATION OF SPIN TRANSFER AND INDIVIDUAL NANOMAGNETS

A Dissertation

Presented to the Faculty of the Graduate School

of Cornell University

in Partial Fulfillment of the Requirements for the Degree of

Doctor of Philosophy

by

Jack Clayton Sankey

August 2007

© 2007 Jack Clayton Sankey

ALL RIGHTS RESERVED

MICROWAVE-FREQUENCY CHARACTERIZATION OF SPIN TRANSFER AND INDIVIDUAL NANOMAGNETS

Jack Clayton Sankey, Ph.D.

Cornell University 2007

This dissertation explores the interactions between spin-polarized currents and individual nanoscale magnets, focusing on the microwave-frequency magnetization dynamics these currents can excite. Our devices consist of two magnetic films (2-40 nm) separated by a nonmagnetic spacer (5-10 nm Cu or 1.25 nm MgO), patterned into a "nanopillar" of elliptical cross-section ∼100 nm in diameter [1]. One magnetic layer (a thicker or exchange-biased "fixed" layer) polarizes electron currents that then apply a spin transfer torque [2, 3] to the other "free" layer. We have developed several high-frequency techniques in which we excite magnetic dynamics with spin-polarized currents and detect the corresponding magnetoresistance oscillations $R(t)$. By applying a direct current I, we can excite both small-angle and new types of large-angle spontaneous magnetic precession of the free layer, inducing a microwave voltage $V(t) = IR(t)$ across the junction that we measure with a spectrum analyzer. By studying the linewidths of the corresponding spectral peaks as a function of bias and temperature, we find the oscillation coherence time (related to the inverse linewidth) is limited by thermal fluctuations: deflections along the precession trajectory for $T < 100$ K, and thermally-activated mode hopping for $T > 100$ K. We have also developed a new form of ferromagnetic resonance (FMR) in which we use microwave-frequency spin currents to excite dy-

namics, and a resonant (DC) mixing voltage to measure the response. With this technique we can directly probe the magnetic damping in both layers, identify the dynamical modes observed in the DC-driven experiment, observe phase locking with these modes, and even probe the physical form of the spin transfer torque. For metallic devices we find the torque is always confined to the plane of the layers' magnetizations, while for (MgO) tunnel junctions we find a new component of the torque perpendicular to this plane, appearing at higher bias voltages [4]. This new FMR technique should be able to probe much smaller devices still, enabling new fundamental studies of even smaller magnetic samples, someday approaching the molecular limit.

BIOGRAPHICAL SKETCH

Jack Clayton Sankey was born on December 5th, 1978 to parents Dorothy and Clayton Sankey in Saint Paul, Minnesota; he was the youngest of three, arriving 18 months after his brother Aaron and five years after his sister Carrie. He spent his entire childhood in North Saint Paul, a short walk from the neighborhood grocery, Minnesota's oldest bar, and the world's largest and most tasteful cement snowman. Through most of elementary school, he wanted most to be a toy designer, knowing in his heart that he could design the awesomest toys ever. In middle school, when good grades, belt packs and sweatpants were no longer cool (and mullets were), he took a bit of abuse, but eventually clawed his way to the floors of North High School, where there was an eerily-broad sense of community and everyone suddenly respected everyone else[1]. He played trombone in jazz and concert band, and eventually picked up the guitar, which he still plays today. He also played tennis heavily, and had a short but brilliant career in soccer, helping countless players score many goals with his unique rendition of "keeper".

Jack attended the University of Minnesota Institute of Technology Honors Program, uncertain if he was going to choose physics or computer science as a major. In his first C-programming course, his obsessive tendencies somewhat overexpressed themselves, depriving him of sleep and thought. Upon realizing that once the class finished so too did his twitching eyelid, he chose physics. He had completely bombed his first physics test, but, vibrating with adrenaline, pulled it together for the rest of the year, and eventually graduated summa cum laude.

During his tenure at the U of M, he tried several initial paths of research,

[1]This was in direct contrast to stereotypes and even other high schools in the area. It was weird.

from the Soudan Collaboration to CLEO, and then down in energy to superfluid helium and liquid crystals. During his tenure with CLEO, he spent some weeks at Cornell University, and instantly fell in love with the place (as opposed to high energy physics, which he did not fall in love with). He applied to Cornell and was accepted with a fellowship. Dan Ralph took him into his group the summer before his first year at Cornell, and that is where he spent the rest of graduate school career.

On September 8th, 2001, there was a hand-grabbing incident with a cute Australian named Nadia Adam. Five years later, they were married and off on some huge boat together. Thus far they have lived happily ever after.

Through all the trials of school and life, Jack has always held firmly the belief that it is ridiculous when people have to write about themselves in the third person.

In loving memory of Grampa Don Nollet

March 22, 1923 - January 21, 2003

ACKNOWLEDGEMENTS

The work presented in this dissertation is the product of an enormous number of people contributing directly and indirectly whether they knew it or not. I am grateful to my family for raising me, my teachers for teaching me, and the world for (despite its troubles) structuring itself in such a way that we can freely inquire about whatever we want, discuss, and learn about the universe around us.

Cornell-wise, I firstly want to thank my advisor, Dan Ralph. He is an exceptional person and an even better advisor. Seriously[2]. He has an excellent sense of humor and was a pleasure to talk to about any random topic, physics or not. He carries a wealth of knowledge that he freely (patiently) disseminates, and also seems to have an uncanny view of the big picture. I have learned an enormous amount from Dan, and on top of this, he paid me. It *often* occurred to me how strange it was that I was not paying him instead (but then the feeling dissipated when he and Bob would scurry by my office giggling and throwing wads of money at each other). On the topic, I'd also like to thank him for finding the funds to buy us so many cool toys in the lab. In all sincerity, I could not have asked to spend my graduate career in a better group.

I would also like to also thank Bob Buhrman, who not only helped fund our enterprise, but also gave me many excellent and interesting conversations. Bob has a knack for instantly seeing my ignorance and then completely embarrassing me about it in a good-natured way.[3] Thanks also to various other Cornell professors for their excellent chats, including Piet Brouwer, Paul McEuen, Chris Henley, and David Lee.

[2]I'm already done so there's no point in me brown-nosing.

[3]I hope it was good-natured, anyway, because I thought it was great and kept coming back for seconds.

Ilya Krivorotov gets his own paragraph too. He came to Cornell as a post-doc, blew the doors off spin transfer, and then rode upon a dragon of solid diamond to California where he is now a professor at Irvine. Early on in my grad school career, Ilya patiently taught me basically everything I know about magnets, and I must say I looked forward to his conversation and extraordinary sense of humor the most in the lab.

I'd also like to take a moment to thank all the helpful and competing groups from around the world for keeping us honest, helping us to understand our systems, and/or lighting a fire under my butt. Specifically, I want to thank Jiang Xiao and Mark Stiles for their beautifully written papers and excellent conversations, and Mark for his discs and the three months of physical therapy[4]. Thanks also to Jacques Miltat, Benoit Montigny, and Giovanni Finocchio for their illuminating papers and discussions. Special thanks to John Slonczewski and Jonathan Sun for interesting conversations, and in particular Jonathan Sun for giving me the glorious MgO samples and, of course, the best day of data-taking I've experienced.[5]

None of this work would have been possible had it not been for all the other amazing scientists living in the basement, either. Nathan Emley took the time to teach the nanopillar fabrication technique to everyone, bridging the gap to the Ralph group, and for that (among many other things) I am deeply appreciative. Thanks to Sergey Kiselev for his enormous help, and for showing me the path to the forest of pigs. Thanks also to Pat Braganca, Andrei Garcia, Kiran Thadani, and Yongtao Cui for their direct contributions and discussions, as well as Greg Fuchs, Eric Ryan, Vlad Pribiag, Zhipan Li, Saikat Ghosh, and Jim Van Howe. I

[4]Sorry, Mark. Of course I know it was my own fault. I shouldn't have called you those things in the first place.

[5]Yes, Dan. The Burger King day was awesome too, but Jonathan and I had *Viva*.

acknowledge support from Kiran's interesting sense of humor, Andrei's explosive laugh[6] and Yongtao's I'm-about-to-say-something stare that I never figured out. Pat the Jacket requires some extra thanks for driving the Beer to Funk Conversion. Given more time, I am certain we could have made it all the way to someone else's basement.

I'd like to thank Ed Myers and Alex Corwin for welcoming me, despite my abrasive personality, into the basement as well as enjoying a delicious chocolate copper cake. Thanks also to Ethan Bernard, Andrew Fefferman, Mandar Deshmukh, Abhay Pasupathy, Alex Champagne, Thiti Taychatanapat, Sufei "Not a Delicious Oven-Baked Meal" Shi, Eugenia Tam, Josh "Pretty Hand" Parks, Marie Rinkoski, Jacob Grose, Kirill Bolotin, and Ferdinand Kümmeth (along with the aforementioned folks) for making life in (and out of) the lab such a pleasure. I have to highlight that I thoroughly enjoyed my conversations with Kirill, who is one of the funniest people I've met, and Ferdinand, who pretty much knows about everything that is interesting (and always delivers said information with an ironic shot to the bag). Special thanks to Jason Petta for the three years of intense G12 occupation, the revealing bachelor party, the drinking, the threats against my well-being, and eventually, the job.

I also acknowledge Y. Nagamine, D. D. Djayaprawira, N. Watanabe, S. Assefa, W. J. Gallagher for MgO sample processing, X. Jiang and S. S. P. Parkin for invaluable sample fabrication assistance, and the support of the IBM MRAM team as a whole. Special thanks to J.-M. L. Beaujour, A.D. Kent, and R. D. McMichael for performing FMR on the extended films of composition described in chapter 4, and Rob Schoelkopf for teaching us so many microwave techniques.

[6]We eventually dropped the A-bomb on California.

We acknowledge support from DARPA through Motorola, the Office of Naval Research, the Army Research Office, and from the NSF (DMR-0605742) and NSF/NSEC program through the Cornell Center for Nanoscale Systems. We also acknowledge NSF support through use of the Cornell Nanofabrication Facility/NNIN and the Cornell Center for Materials Research facilities.

Many other people supported me throughout this process by making life outside the lab enjoyable. I'd like to specifically thank my good friends Dan Betes Goldbaum[7] for always being around for a quick "snack" or chat, plus the countless hours of mindless entertainment and support throughout grad school. Thanks also to James Slezak for Stella's and the occasional credit card tips, Arend van der Zande for his heart of gold, Matt van Adelsberg and Isaac Robinovitz for the heavy drinking end of the spectrum, Adam and Lacy Swanson, and Josh and Heidi Waterfall for many, many high quality days in Ithaca. A big thank you to Andrew Perrella for putting up with me, and his wife Fern for putting up with us. I am lucky to have known you for any length of time, Andrew. I also have to acknowledge the inspirational and excessively fun Minnesota friends that somehow continue to seek my company today, despite my best efforts. Thanks to Nate Davey and the Rohöl that ensues, Vince and Kristi Chan (and of course the boat ill-equipped for Sankey colons), Kevin "DR" Oie, Dave Kam and his odd ability to make me look *forward* to Denny's, Alanna Barry, Luke "A Perfectly Ordinary Number of Cheese Puffs" Kuhl, and his wife/owner Renee. Kevin, Nate, and Luke really require some kind of medal for their sheer endurance.

My deepest gratitude, however, goes to my parents Dorothy and Clayton who (with love and a dry sense of humor) raised me, and always encouraged my random

[7]and its proboscis

questions and aspirations[8]. These feats alone are worth at least seven or eight nursing home visits. At *least.* I love you both! Thank you!

Thanks also for encouragement (both intentional and unintentional) from my sister Carrie, her husband Allen, and especially from my brother Aaron of whom I have grown very fond of over the years, perhaps to the point of socially unacceptable.

At the end of the day, though, I could not have gotten through this process without the support and love of my best friend and wife Nadia. She helps me through all the most difficult moments, and is with me to share the beautiful ones as well. She's always up for a deep or complex conversation, and always slaps me back in line when I lose touch with reality. On top of all this, she's frickin hilarious and I love her.

Along these lines I'd also like to thank Australia, Nadia's friends Nic and Prerena, and especially Nadia's parents Mike and Gillian for raising such a talented, insightful woman, and then letting her live on the other side of the world.

Respect.

[8]Of specific relevance to Physics, they gave me Carl Sagan in VHS form many years ago. I would also like to thank Carl Sagan in VHS form.

TABLE OF CONTENTS

1 Introduction **1**
- 1.1 Overview . . . 1
- 1.2 Background Information: A Section for Parents . . . 2
- 1.3 Spin Transfer Basics . . . 6
  - 1.3.1 Magnetoresistance and Spin Transfer . . . 6
  - 1.3.2 Spin Transfer's Effect on Tiny Ferromagnets . . . 12
- 1.4 Context of This Dissertation . . . 20

2 Microwave Oscillations of a Nanomagnet Driven by a DC Spin-Polarized Current **29**
- 2.1 Introduction . . . 29
- 2.2 Devices and Apparatus . . . 30
- 2.3 Data and Analysis . . . 33
- 2.4 Conclusions . . . 39

3 Mechanisms Limiting the Coherence of Spontaneous Magnetic Oscillations Driven By DC Spin-Polarized Currents **41**
- 3.1 Introduction . . . 41
- 3.2 Sample Geometry . . . 42
- 3.3 Data and Analysis . . . 43
- 3.4 Conclusions . . . 55

4 Spin-Transfer-Driven Ferromagnetic Resonance of Individual Nanomagnets **56**
- 4.1 Introduction . . . 56
- 4.2 Devices and Apparatus . . . 57
- 4.3 Data and Analysis . . . 59
- 4.4 Conclusions . . . 68
- 4.5 Appendices . . . 70
  - 4.5.1 Device Details and Circuit Calibration . . . 70
  - 4.5.2 Relationship Between Linewidth and Damping . . . 71
  - 4.5.3 Simulation Parameters . . . 72
  - 4.5.4 Regarding Another Proposed Mechanism for DC Voltages Produced by Magnetic Precession . . . 72

5 Direct Measurement of the Spin Transfer Torque and its Bias Dependence in Magnetic Tunnel Junctions **74**
- 5.1 Introduction . . . 74
- 5.2 Devices and Apparatus . . . 76
- 5.3 Conclusions . . . 87
- 5.4 Appendices . . . 90
  - 5.4.1 ST-FMR Artifacts Due to the Leads . . . 90

5.4.2 Derivation of the ST-FMR Signal (Eq. 5.2) 90
5.4.3 Details of the Calibration of I_{RF}^2 93
5.4.4 Regarding a Possible Alternative Mechanism for the Anti-symmetric Lorentzian Component of the ST-FMR Signal 96
5.4.5 Regarding the Effects of Heating on Measurements of the Perpendicular Torkance 98

6 Appendices **100**
6.1 A Quick Note on Microwave Coupling in Our System 100
6.2 A Quick Note on Pulsed RF Measurements 100

Bibliography **106**

LIST OF FIGURES

1.1 Cartoon of our devices, which consist of two elliptical magnetic pancakes (roughly $5 \times 50 \times 100$ nm^3) separated by a non-magnetic spacer. Electrical contact is made at the top and bottom of the device with normal metal leads. Current flows vertically through the wire. 5

1.2 An illustration of magnetoresistance in our devices (assuming magnetic layers are perfect polarizers). (a) When the two magnetizations **M** and **m** are parallel, electrons (labeled) of one spin can pass through both layers. This is the low resistance configuration. (b) When the magnetizations are antiparallel, neither spin is allowed through. This is the high-resistance configuration. 7

1.3 An illustration of the spin transfer torque in our devices. The magnetizations of the layers are labeled **m** and **M**. (a) A single magnetic layer with a spin-polarized electron passing through it. The magnet transmits and scatters the the collinear component of the spin ($s_{||}$) and absorbs the transverse component ($s_{\perp}$). (b) Schematic of one of our devices, consisting of two magnetic layers separated by a non-magnetic spacer. One magnetic layer (the layer that is less susceptible to spin transfer, due to larger size or exchange bias) generates spin-polarized electrons that then apply a spin transfer torque to the other magnetic layer. This sign of current stabilizes the parallel configuration. (c) Spin transfer for the opposite sign of current. The reflected electrons have the opposite spin, so the free layer feels a torque in the opposite direction, destabilizing the parallel configuration. This torque can work against the damping (labeled) to reverse **m** or excite magnetic precession. 9

1.4 Hysteretic switching using spin transfer in device 1 of chapter 2 (no applied magnetic field). Starting in the parallel state and increasing the current, the system passes a critical point (0.75 mA) and switches to the antiparallel state, which has higher resistance. Decreasing the current through a similar critical point on the negative side, the system switches back. 11

1.5 A very large, very flat magnetic disc, with the magnetization uniformly pointed out of the plane under no applied field. What is the field at the center? 13

1.6 (a) Sketch of one of the magnetic layers in our devices, with the vector **M** denoting the magnetization. (b) The contours of constant magnetic potential energy (for the nanomagnet above) projected on the unit sphere. The magnetization **M** precesses along these contours, while while magnetic damping slowly relaxes it to the energy minimum, wherein **M** points in either direction along the long magnetic easy axis (labeled). Point A is a potential well, and point B is a saddle point. 16

2.1 Resistance and microwave data for sample 1. (a) Schematic of the sample and the heterodyne mixer circuit. (b) (offset vertically) dV/dI versus I for H = 0, 0.5, 1.0, 1.5, 2.0, and 2.5 kOe, with current sweeps in both directions. At H = 0, the switching currents are I_c^+ = 0.88 mA and I_c^- = -0.71 mA, and ΔR_{max} = 0.11 Ω between the P and AP states. Colored dots on the 2 kOe curve correspond to spectra in (c). (inset) dV/dI near $I = 0$. (c) (offset vertically) Microwave spectra with Johnson noise P_{JN} subtracted at H = 2 kOe, for several values of I. (inset) Spectrum at H = 2.6 kOe and I = 2.2 mA, where f and $2f$ peaks are visible on the same scan. (d) (offset vertically) Spectra at H = 2.0 kOe, for I = 1.7 to 3.0 mA in 0.1 mA steps, showing the growth of the small-amplitude precessional peak and then a transition to the large-amplitude regime (2nd harmonic). (e) Field dependence of the low-bias peak frequency (top) and the large-amplitude regime (first harmonic) at I = 3.6 mA (bottom). The line is a fit to Eq. 2.1 (f) Microwave power versus frequency and current at H = 2.0 kOe. The black line shows dV/dI versus I from (b). 32

2.2 Data from sample 2, which has (at $H = 0$) I_c^+ = 1.06 mA, I_c^- = -3.22 mA, P-state resistance (including leads) 17.5 Ω, ΔR_{max} = 0.20 Ω, and $4\pi M_{eff}$ = 12 kOe. (a) Broadband (0.1-18 GHz measured with a detector diode directly after amplification) power versus I and H, for I swept negative to positive. The white dots show the position of the AP to P transition for I swept positive to negative. (b) dV/dI at the same values of I and H. A smooth I-dependent, H-independent background (similar to that of Fig. 2.1b) is subtracted emphasize the different regimes. Resistance changes ΔR are measured relative to P. (c) Dynamical stability diagram extracted from (a) and (b). P/AP indicates bistability, S and L the small- and large-amplitude dynamical regimes, and W a state of intermediate resistance and only small microwave signals. The colored dots in (c) correspond to the microwave spectra at H = 500 and 1100 Oe shown in (d). 36

2.3 Results of numerical solution to the Landau-Lifshitz-Gilbert equation for a single-domain nanomagnet at zero temperature. The parameters are: $4\pi M_{eff} = 10$ kOe, $H_{an} = 500$ Oe, Gilbert damping parameter $\alpha = 0.014$, and effective polarization $P = 0.3$, which produce $H_c = 500$ Oe and $I_c^+ = 2.8$ mA. (a) Theoretical dynamical stability diagram. The pictures show representative precessional trajectories of the free-layer moment vector **m** (the fixed layer moment vector **M** and applied field **H** remain static). For the "out-of-plane" case, the system chooses (depending on initial conditions) one of two equivalent trajectories above and below the sample plane. (b) Dependence of precession frequency on current in the simulation for $H = 2$ kOe, including both the fundamental frequency and harmonics in the measurement range. The vertical dividing lines correspond to the phase diagram boundaries of (a). . 38

3.1 (a) A far narrower spectral peak from a nanopillar device than those reported prior to the original publication of this work (FWHM = 5.2 MHz) [54]. The device has the same composition as device 3, described in the text. (Inset) Schematic of a nanopillar device. (b) Differential resistance of device 1 as a function of I and H at $T = 4.2$ K, obtained by increasing I at fixed H. AP denotes static antiparallel alignment of the two magnetic moments, P parallel alignment, P/AP a bistable region, SD small-angle dynamics, and LD large-angle dynamics. 44

3.2 Measured linewidths vs T for (a) device 1 and (b) device 2. The dashed line is a fit of the low-T data to Eq. 3.2 and the solid line is a combined linewidth from Eqs. 3.2 and 3.3, obtained by convolution. (Inset) Dependence of linewidth on I for device 1, with estimates of precession angles. 46

3.3 (Main plot and lower inset) Squares: Linewidth calculated directly from the Fourier transform of $R(t)$ within a macrospin LLG simulation of the dynamics of device 1. Triangles: Linewidth calculated from the same simulation using the right-hand side of Eq. 3.2. The discrepancy at high temperature hints that motional narrowing is worth pausing to consider, but not over the temperature range reported here. Line in inset: Fit to a $T^{1/2}$ dependence. (Top inset) Simulated probability distribution of the precession angle at 15 K. At higher temperatures, the distribution in θ becomes more complicated than a simple peak and the $T^{1/2}$ behavior begins to break down. 49

3.4 Measured (a) frequencies and (b) linewidths of large-angle dynamical modes in device 3 for $T = 40$ K, $\mu_0 H = 63.5$ mT applied in the exchange-bias direction, 45° from the free-layer easy axis. When two modes are observed in the spectrum simultaneously, both linewidths increase. 53

4.1 (a) Room-temperature magnetoresistance as a function of field perpendicular to the sample plane. (inset) Cross-sectional sample schematic, with arrows denoting a typical equilibrium moment configuration in a perpendicular field. (b) Schematic of circuit used for FMR measurements. (c) FMR spectra measured at several values of magnetic field, at I_{DC} values (i) 0, (ii) 150 μA, and (iii) 300 μA, offset vertically. Symbols identify the magnetic modes plotted in (d). Here $I_{RF} = 300$ μA at 5 GHz and decreases by $\sim 50\%$ as f increases to 15 GHz (refer to appendix 4.5.1). (d) Field dependence of the modes in the FMR spectra. The solid line is a linear fit, and the dotted line would be the frequency of completely uniform precession. 60

4.2 Comparison of FMR spectra to DC-driven precessional modes. (a) Spectral density of DC-driven resistance oscillations for different values of I_{DC} (labeled), with $\mu_0 H = 370$ mT and $I_{RF} = 0$. (b) FMR spectra at the same values of I_{DC}, measured with $I_{RF} = 270$ μA at 10 GHz. The high-f portions of the 305, 445, and 505 μA traces are amplified to better show small resonances. The $I_{DC} = 0$ curve is the same as in Fig. 4.1c. 62

4.3 (a) FMR peak shape for mode A_0 at $I_{DC} = 0$ and different values of I_{RF}: from bottom to top, traces 1-5 span $I_{RF} = 80$-340 μA in equal increments, and traces 5-10 span 340-990 μA in equal increments. (b) Bottom curve: spectral density of DC-driven resistance oscillations for mode A_0, showing a peak with half width at half maximum = 13 MHz. Top curve: FMR signal at the same bias conditions, showing the phase-locking peak shape. (inset) Evolution of the FMR peak for mode A_0 at 370 mT, $I_{DC} = 0$, for I_{RF} from 30 μA to 1160 μA. (c) Evolution of the FMR signal for mode A_0 in the phase-locking regime at $I_{DC} = 0.5$ mA, $\mu_0 H = 370$ mT, for (bottom to top) I_{RF} from 12 to 370 μA, equally spaced on a logarithmic scale. (d) Results of macrospin simulations for the DC-driven dynamics and FMR signal 4.5. 65

4.4 (a) Detail of the peak shape for mode A_0, at $I_{DC} = 0$, $I_{RF} = 180$ μA, $\mu_0 H = 535$ mT, with a fit to a Lorentzian line shape. (b) Dependence of linewidth on I_{DC} for modes A_0 and B_0, for $\mu_0 H = 535$ mT. For the PyCu layer mode A_0, Δ_0/f_0 is equal to the magnetic damping α. The critical current is $I_c = 0.40 \pm 0.03$ mA at $\mu_0 H = 535$ mT, as measured independently by the onset of DC-driven resistance oscillations. 66
4.5 Estimated RF current coupled into our device as a function of frequency, relative to the value at 5 GHz. 71

5.1 Magnetic tunnel junction geometry and magnetic characterization. (a) Schematic of the sample geometry. (b) Bias dependence of differential resistance at room temperature for the parallel orientation of the magnetic electrodes ($\theta = 0°$) and antiparallel orientation ($\theta = 180°$), along with intermediate angles. The angles are determined assuming that the zero-bias conductance varies as $\cos(\theta)$. (Left inset) Layout of the electrical contacts (cropped), showing where the top electrode is cut to eliminate measurement artifacts. (Right inset) Zero-bias magnetoresistance for H along $\hat{z}$. 77
5.2 ST-FMR spectra at room temperature. (a) Spin-transfer FMR spectra for $I = 0$, for magnetic fields (along $\hat{z}$) spaced by 0.2 kOe. I_{RF} ranges from 12 μA at low field (high resistance) to 25 μA at high field. The curves are offset by 250 μV. (b) Details of the primary ST-FMR peaks at $H = 1000$ Oe and $I_{RF} \approx 12\mu$A for different DC biases. Symbols are data, lines are Lorentzian fits. These curves are not artificially offset; the frequency-independent backgrounds for nonzero DC biases correspond to the first term on the right of Eq. 5.2. A DC bias changes the degree of asymmetry in the peak shape vs. frequency. 78
5.3 Fit parameters for the ST-FMR signals at room temperature, for three values of magnetic field in the $\hat{z}$ direction and $I_{RF} \approx 12\mu$A. (a) Amplitude of the symmetric and antisymmetric Lorentzian component of each peak. (b) The linewidths $\sigma/2\pi$. (c) The center frequencies $\omega_m/2\pi$. (d) Non-resonant background component. . . . 81

5.4 Bias dependence of the spin-transfer torkances and magnetic damping. (a) Magnitudes of the in-plane torkance $d\tau_{||}/dV$ and the out-of-plane torkance $d\tau_{\perp}/dV$ determined from the room temperature ST-FMR signals, for three different values of applied magnetic field in the $\hat{z}$ direction. The overall scale for the torkances has an uncertainty of $\sim 15\%$ associated with the determination of the sample's magnetic volume. (Inset) Angular dependence of the torkances at zero bias. (b) Comparison of the bias dependences of $d\tau_{||}/dV$ and $dI/dV(\mathrm{P})$, scaled by the zero-bias values. To aid the visual comparison of the variations, small linear background slopes (discussed in appendix 5.4.2) are subtracted from the torkance values. (c) Symbols: Effective damping determined from the ST-FMR linewidths. Lines: Fit to Eq. 5.5, for $|V| < 300$ mV. 83
5.5 Magnitudes of the in-plane and out-of plane differential torques $d\tau_{||}/dI$ (black symbols) and $d\tau_{\perp}/dI$ (lighter symbols) vs. I, determined from fits to room-temperature ST-FMR spectra. The overall scale for the y-axis has an uncertainty of $\sim 15\%$ associated with the determination of the free-layer's magnetic volume. (Inset) Angular dependence of the differential torques at zero bias. 84
5.6 ST-FMR signals for a metallic spin valve, (in nm) Py 4 / Cu 80 / IrMn 8 / Py 4 / Cu 8 / Py 4 / Cu 2 / Pt 30, with $H = 560$ Oe in the plane of the sample along $\hat{z}$ and with an exchange bias direction 135 from $\hat{z}$. We estimate $\theta = 77^{\circ}$ from the GMR. The average anti-symmetric Lorentzian component is $2 \pm 3\%$ the size of the symmetric Lorentzian component over this bias range. Accounting for the out-of-plane anisotropy $4\pi M_{eff} \sim 1$ T in Eq. 5.2 of the main paper, we estimate that the ratio $\tau_{\perp}/\tau_{||} < 1\%$. 88
5.7 Test of the calibration for I_{RF} and the non-resonant background, for $H = 1.0$ kOe in the $\hat{z}$ direction. Circles: Magnitude of non-resonant background measured from fits to the ST-FMR peaks. Squares: the background expected from equations 5.14 and 5.15 after determining $I_{RF} = 11.7$ μA at $I_0 = -30\mu$A. 95
5.8 Representative examples of the bias dependence of I_{RF} and $\partial^2 V/\partial\theta\partial I$ for H in the $\hat{z}$ direction. Values of I_{RF} and $\partial^2 V/\partial\theta\partial I$ at $V = 0$ are labeled. I_{RF} is determined using the procedure described above. $\partial^2 V/\partial\theta\partial I$ is determined by measuring $\partial V/\partial I$ vs. I at a sequence of magnetic fields in the $\hat{z}$ direction, by assuming that the conductance changes at zero bias are proportional to $\cos(\theta)$ and that θ depends negligibly on I, and then by performing a local linear fit to determine $\partial^2 V/\partial\theta\partial I$ for given values of I and H. 97

6.1 Sketch of the photolithographically-defined leads for making high frequency electrical contact to our devices. The whole structure is much smaller than the wavelengths of interest, so we treat it as a lumped-element termination. 101
6.2 Diagram of the sequencing to generate a pulse of RF current. The output of the sweeper is divided to a MHz-frequency TTL square-wave that is fed into the DAQ card as a reference clock. When we tell the computer to fire, it sends a message to the DAQ logic to output a pulse that is 2 cycles long, which is fed into the pulser's gate. When the gate is high, the pulser uses the next descending edge to trigger. By adding delay to the frequency divider prior to the pulse trigger, we can increase the sensitivity of the RF phase to small changes in frequency. 104

Chapter 1

Introduction

1.1 Overview

In this dissertation, we explore the interactions between ferromagnetism and the electron's intrinsic spin in nanoscale systems.

Over the past decade, we have learned to not only *control* the average spin carried by electrons flowing through nanoscale structures, but also how to *use* this spin current to manipulate nanoscale magnets far more efficiently than is possible with magnetic fields alone.[1] As systems continue to shrink, the impact of spin currents on nanomagnets (the "spin transfer" effect) increases, making it attractive for future applications such as spin-transfer-driven magnetic RAM (ST-MRAM) for computers. In one bit of ST-MRAM, spin currents are used to swap the north and south poles of a nanomagnet. One orientation corresponds to the logical bit state "1" and the other corresponds to "0". The major advantage of this technology is that the magnetic bits require no power to retain their information (unlike leaky transistor-based RAM found in computers today). If one were to unplug a computer equipped with ST-MRAM and then plug it back in a year later, it would remember its previous state and not need to reboot.

We have also recently discovered that spin transfer from DC electrical currents can be use to drive new types of spontaneous gigahertz-frequency[2] magnetic os-

[1] Magnetic fields require relatively large currents to generate, and are not easy to localize.

[2] One gigahertz (GHz) is 1,000,000,000 Hz, a billion cycles each second. The highest frequency your ear can detect is about 20,000 Hz, FM radio is broadcast at roughly 50,000,000 Hz, and computers process logic at a few gigahertz. We have measured oscillations from our magnetic devices in excess of 35 GHz [5].

cillations, and that these oscillations can in turn generate a reasonable amount of microwave power (discussed in chapters 2 and 3). While practical applications involving this effect are currently limited by the coherence time of the oscillations (studied in chapter 3), similar devices may one day be used in communications applications such as microwave sources and resonators.

We can also perform the inverse experiment; as described in chapters 4 and 5, we can drive resonant magnetic oscillations with *gigahertz*-frequency spin currents, and then measure the response through a DC voltage generated by our device. With this technique we can now directly probe many physical parameters that were previously hidden from us, such as the magnetic damping and the actual form of the spin transfer effect itself. In addition, we can use this technique to further understand the oscillations driven by DC currents and how they interact with spin polarized current. The inherent ability of these devices to resonantly convert microwave power into a DC voltage may very well be applied in microwave signal processing applications such as frequency-tunable detection diodes or mixers.

1.2 Background Information: A Section for Parents

When electrical current flows into a magnetic material, the electrons are selectively filtered or "polarized" based on the orientations of their spins (relative to the direction the material is magnetized). The effect of central importance to this dissertation occurs when these polarized electrons rush out of one magnet and into another, causing the unique brand of mayhem termed "spin transfer". Of course, big chunks of magnetic material that you could hold in your hand will also polarize electrical current, but due to various scattering mechanisms (electrons bounce around *a lot* as they're pushed through most wires), the polarization fades

over very short distances once electrons leave a magnetic material. If we wish to study these effects, we must therefore make the system small. Furthermore, the smaller a magnet is, the fewer electrons are required to affect it, so we also make the systems small in the interest of exploring this unique branch of physics without dimming the lights in the building.

Before we continue, we should take a moment to introduce some of the basic concepts we will need in our discussion. First of all, what is magnetism, exactly? Generally we're all familiar with the magnets we hold in our hands generating magnetic fields that can push or pull on other magnets, but what is causing this magnetic behavior in the first place? As mentioned above, electrons each carry with them a small amount of angular momentum called "spin". It's the same stuff that a spinning top or a rotating planet carry in bulk, only for an electron it is such a small amount that quantum mechanical weirdness[3] comes into play. Still, as with a slowly rotating galaxy or a rapidly twirling Aaron Sankey, it is intuitively useful to think of electron spin as representing some small amount of circulating *stuff*. Some of this circulating stuff is (negative) charge, which generates a small magnetic field. Electrons are fated to carry this field with them wherever they go.

In a ferromagnetic material such as iron, due to some of the aforementioned quantum weirdness [6], the electrons feel a substantial amount of peer-pressure to lock together with their spins aligned. To be an electron with spin aligned in opposition to the neighborhood consensus requires quite a bit of extra energy. Consequently, a lot of electrons whose spins would otherwise balance any net cir-

[3]For example, you, I and other large bulky things have well-defined logical concepts like "up" or "down". A top spins clockwise (rotation axis points up) or counter-clockwise (rotation axis points down). Electrons, on the other hand, can have their spin oriented up, down, or *both simultaneously*.

culation in the system spontaneously choose to unbalance it.[4] In such a material, there is then a *spin-dependent* asymmetry in the number (and efficiency) of channels available for electron conduction, and so electrical currents flowing through the material also carry some net spin with them. Furthermore, if an electron has the wrong spin and tries to *enter* a material like iron, it will have much more difficulty getting in than all the other, more popular spins. This spin-dependent conduction is the root of everything we explore in this dissertation.

As emphasized above, the physical system we study is quite small. Figure 1.1 is a cartoon of one of our devices, which consists of two magnetic pancakes (the darker layers in Fig. 1.1) roughly 5 nm thick, separated by a short (roughly 10 nm) nonmagnetic spacer layer through which electrons pass without losing polarization. This stack is patterned into a short wire of diameter roughly one thousand times smaller than a human hair, about 100 nm across. We make electrical contact to the two ends of the wire with normal metal leads (such as copper) so that we can run current vertically through the stack. Spin transfer occurs when electrons, still polarized from passing through one magnet, are forced through the other magnet. In passing, they can deposit some of their angular momentum into the magnet, causing the magnetization[5] to rotate a little. Though this process is much more efficient than trying to rotate it with an external magnetic field (which requires a lot of current), and though the device is incredibly small, it still takes a substantial electrical current for these interactions to become significant. Generally we push

[4]When this happens, all the little circulating currents can work together to generate the macroscopic magnetic field that you feel tugging on your refrigerator magnets.

[5]The magnetization is just an arrow pointing from the south pole to the north pole.

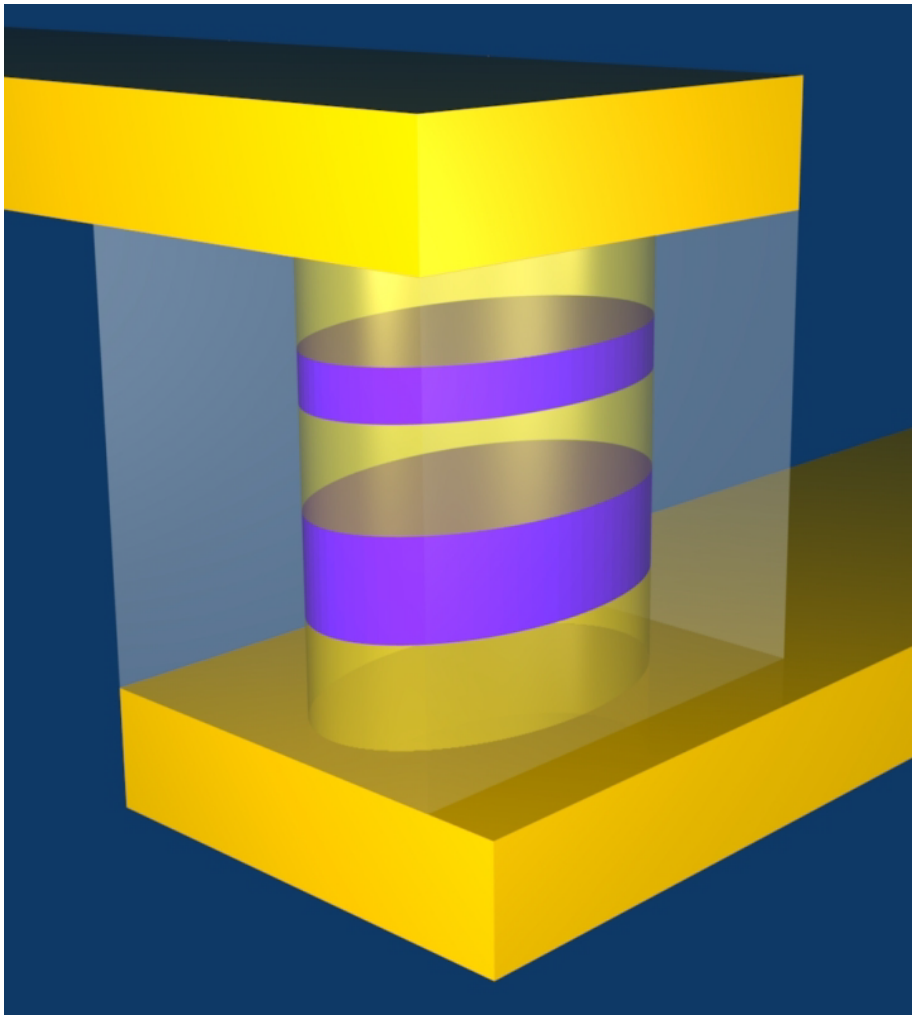


Figure 1.1: Cartoon of our devices, which consist of two elliptical magnetic pancakes (roughly $5 \times 50 \times 100$ nm^3) separated by a non-magnetic spacer. Electrical contact is made at the top and bottom of the device with normal metal leads. Current flows vertically through the wire.

currents on the order of a *milliamp* through these tiny wires.[6]

1.3 Spin Transfer Basics

Understanding the literature on spin transfer and nanoscale magnetism can be quite challenging. By way of papers and talks, I personally suffered a barrage of statements and intuitions that were often conflicting, misleading, and in some cases, incorrect. Needless to say, there is a daunting amount of information to sift through. This section attempts to arm new magnetists with the basic intuitions we have constructed in the past years through numerous discussions, papers, and hair pulling. Hopefully it will also give the reader enough qualitative intuition to understand the rest of the dissertation.

1.3.1 Magnetoresistance and Spin Transfer

As discussed above, magnetic materials tend to filter passing electrons based on their spins. The first interesting effect arising from this property is magnetoresistance; the resistance of the device depends on the relative orientations of the two layers' magnetizations. To motivate how this comes about, we appeal to the commonly-used cartoon picture shown in Fig. 1.2. We assume for simplicity that each magnet *only* allows through spins parallel to the magnetization, and rejects all antiparallel spins. If the two magnetizations (denoted **M** and **m** in Fig. 1.2) are in the parallel (P) configuration (Fig. 1.2a), half the spins are rejected at the first layer and the other half are allowed through both layers, giving a relatively low

[6] If you were somehow able to scale the system to the size of an ordinary 12-gauge wire running through your walls, this current density would correspond to roughly a *million* amps. The study of such a device would require a small, dedicated nuclear power plant.

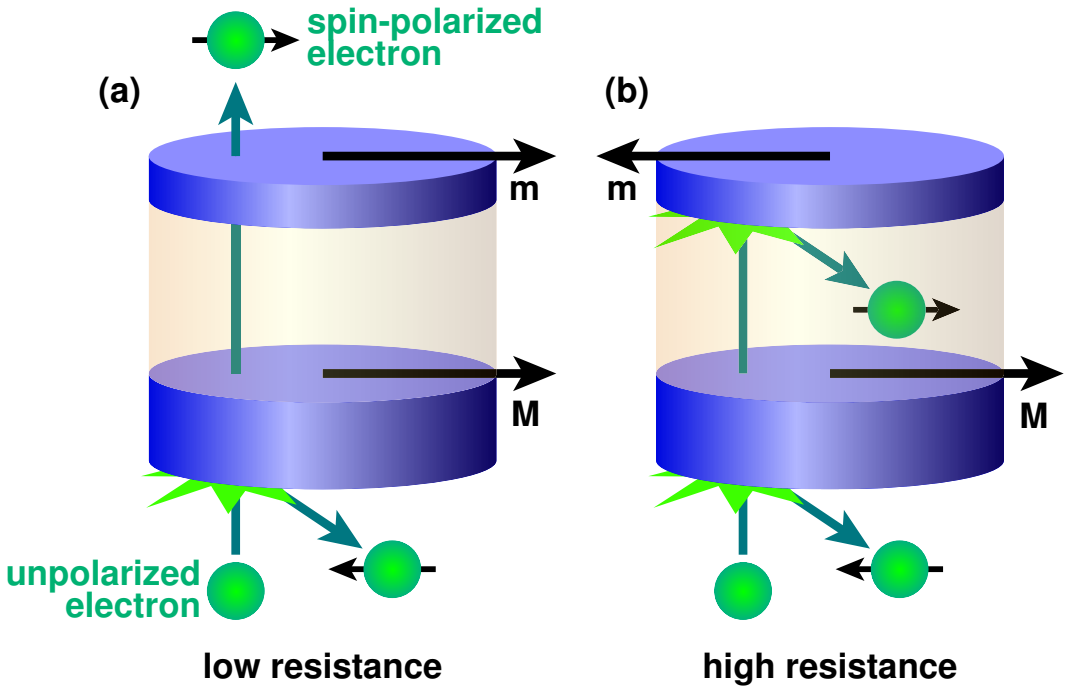


Figure 1.2: An illustration of magnetoresistance in our devices (assuming magnetic layers are perfect polarizers). (a) When the two magnetizations **M** and **m** are parallel, electrons (labeled) of one spin can pass through both layers. This is the low resistance configuration. (b) When the magnetizations are antiparallel, neither spin is allowed through. This is the high-resistance configuration.

value of resistance. In the antiparallel (AP) state (Fig. 1.2b), neither sign of spin is allowed through the junction, giving a high value of resistance. As expected, states in between P and AP have intermediate resistance values. This effect is currently used in hard drives to sense the small fields generated by the disk's magnetic domains; a small magnetic element with a freely rotating magnetization is held closely above the disk, and its orientation, influenced by the small fields from disk surface, is "read" resistively.

A second interesting effect arising from spin filtering is the spin-transfer torque. Whereas magnetoresistance is the influence of magnetic materials on passing electrons, spin transfer is the influence of passing electrons on magnetic materials. To motivate this effect, we appeal once again to the simple physical picture described above. As shown in Fig. 1.3a if a spin-polarized electron passing through a magnetic layer has its spin at some finite angle θ (labeled) relative to the magnetization, then by decomposing this spin state relative to $\mathbf{m}$ ($|\theta\rangle$ into $|\uparrow\rangle$ and $|\downarrow\rangle$ with quantization axis $\mathbf{m}$), we see that the magnet will let through the part of the electron that is parallel and reflect the part that is antiparallel. Interestingly, the expected angular momentum of the electron before and after scattering is not the same. Before scattering there is a spin component $s_\perp$ (labeled) perpendicular to $\mathbf{m}$ (of magnitude $(\hbar/2)\sin(\theta)$), while after scattering the expected spin angular momentum points either parallel or antiparallel to $\mathbf{m}$. This perpendicular component that seems to have vanished is actually deposited into the magnet, applying a small torque[7] (labeled τ) to the magnetization. Essentially, the magnetization recoils a little whenever it rotates a passing electron's spin.

Of course this simple model only qualitatively captures the physics of our sys-

[7]One electron carries very little angular momentum compared to the millions of spins in our nanomagnets, which is why we require "large" currents.

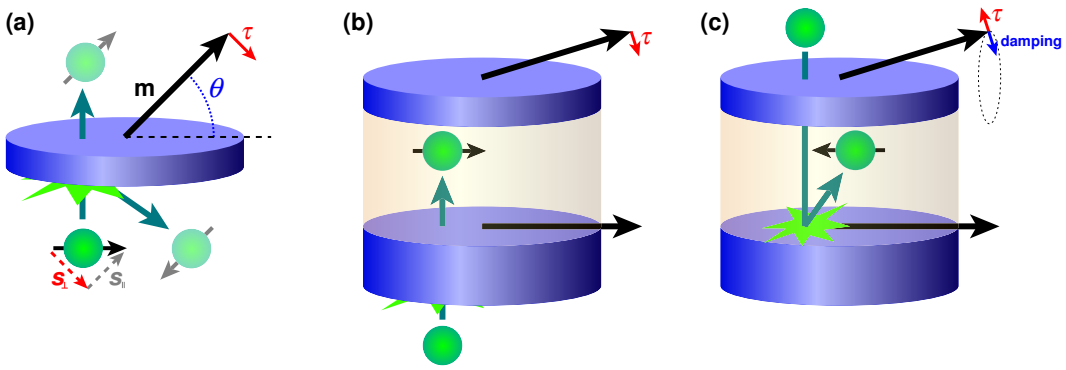


Figure 1.3: An illustration of the spin transfer torque in our devices. The magnetizations of the layers are labeled **m** and **M**. (a) A single magnetic layer with a spin-polarized electron passing through it. The magnet transmits and scatters the the collinear component of the spin ($s_{||}$) and absorbs the transverse component ($s_{\perp}$). (b) Schematic of one of our devices, consisting of two magnetic layers separated by a non-magnetic spacer. One magnetic layer (the layer that is less susceptible to spin transfer, due to larger size or exchange bias) generates spin-polarized electrons that then apply a spin transfer torque to the other magnetic layer. This sign of current stabilizes the parallel configuration. (c) Spin transfer for the opposite sign of current. The reflected electrons have the opposite spin, so the free layer feels a torque in the opposite direction, destabilizing the parallel configuration. This torque can work against the damping (labeled) to reverse **m** or excite magnetic precession.

tem. If we wanted to try and predict the quantitative details of magnetoresistance and spin transfer, we would need to include a spin polarization that is less than 100% perfect[8] along with the mixing conductances throughout the device. For metallic spacers [7] we would also need to calculate the average effect of all the electron wave functions including the boundary conditions from all the layers in our devices. For tunnel junctions [4] we would need to include the effects of large junction voltages and the density of states. To make the models very accurate[9] we would also have to take into account surface roughness, disorder, the finite spin diffusion length, and edge effects, to name a few. It is very difficult to consider all of these things together, but work has been done on spin transfer in the diffusive transport limit for similar systems [8, 9].

In our devices, one magnetic layer is thicker than the other (or it is pinned with an exchange biasing layer), making it less susceptible to spin transfer effects for a given amount of current. We use this "fixed" layer to generate the polarized electrons that can then apply torques to the thinner "free" layer as shown in Fig. 1.3b. By reversing the sign of the current (Fig. 1.3c), we can generate the opposite sign of torque on the free layer, because in this case it is the *reflected* electrons (which have the opposite spin) that carry the spin information from the fixed layer.

The direction of electron flow in Fig. 1.3c tends to destabilize the P state. It points in a direction that opposes the magnetic damping (labeled, which always pushes the system downhill in energy). If the current is large enough, it can overcome the damping, and the free layer will begin to precess to increasing angles (perhaps along the dotted line). If the AP state is stable, then beyond some critical

[8] It is more like 30-80% in our devices, depending on the materials.

[9] A theory with all these things included has not been assembled to my knowledge.

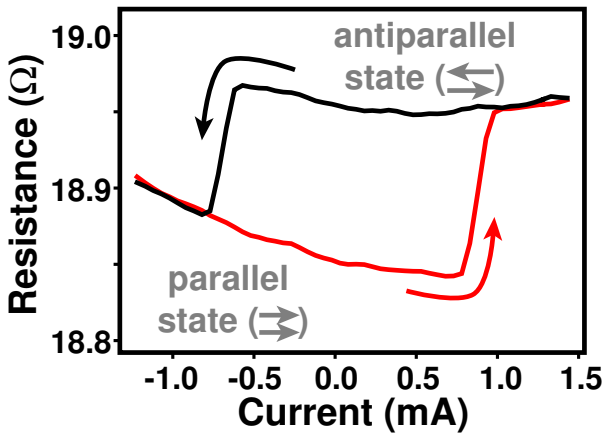


Figure 1.4: Hysteretic switching using spin transfer in device 1 of chapter 2 (no applied magnetic field). Starting in the parallel state and increasing the current, the system passes a critical point (0.75 mA) and switches to the antiparallel state, which has higher resistance. Decreasing the current through a similar critical point on the negative side, the system switches back.

angle **m** will reverse entirely. This sign of current ("positive" by our convention) favors the AP state while the opposite current (Fig. 1.3b) favors the P state. If both states are stable, this leads to magnetic hysteresis under applied currents [10,11] and enables the ST-MRAM application mentioned above. Figure 1.4 shows this hysteresis in action for one of our devices (device 1 of chapter 2). Starting in the parallel state (labeled) and increasing the current, at a critical value of 0.75 mA, the free layer switches to the antiparallel state, marked by an abrupt jump to higher resistance. Decreasing the current through a similar critical point on the negative side, the free layer switches back to parallel.

If we apply enough of a magnetic field parallel to **M** so that the AP state is no longer stable, then beyond the critical current the free layer magnetization can spontaneously precess to very large angles at microwave frequencies. This new,

steady-state dynamical regime full of interesting physics and possible applications that we begin to explore in chapters 2 and 3. We can also apply high-frequency currents to resonantly drive the precession, and then measure the response through a DC voltage generated by mixing of the oscillating current and magnetoresistance. This new form of ferromagnetic resonance (discussed in chapters 4 and 5) allows us to directly measure the damping parameter and the actual form of the spin-transfer torque itself, as well as helping us to understand the dynamical modes driven by DC spin-polarized currents.

1.3.2 Spin Transfer's Effect on Tiny Ferromagnets

Before we describe what spin transfer does to a nanomagnet, we first describe what a nanomagnet does to itself. We begin by discussing a simple but excellent question posed to me by my favorite magnetist, Ilya Krivorotov. Figure 1.5 shows a very thin magnetic disc with an enormous radius, and a uniform magnetization (arrows) pointing vertically out of the plane (no applied external field).[10] Let $\mu_0\mathbf{H} = \mathbf{B} - \mu_0\mathbf{M}$ (SI units) as defined in most introductory texts. The question is this: In the limit where the disc is very large and flat, what is the direction and magnitude of the real magnetic field (that you would measure with a hall probe) at the center (a) inside the disc, and (b) just above the disc? I personally guessed the wrong answer, and wish I had thought harder about the problem before blurting it all over myself. The answer, as it turns out, is that both fields (a) and (b) are the same, pointing vertically, with magnitude approaching zero. This can be explained in several ways, but I feel the safest, most physical intuition comes from looking

[10] This configuration is often attained in neodymium magnets, which have strong crystalline anisotropy.

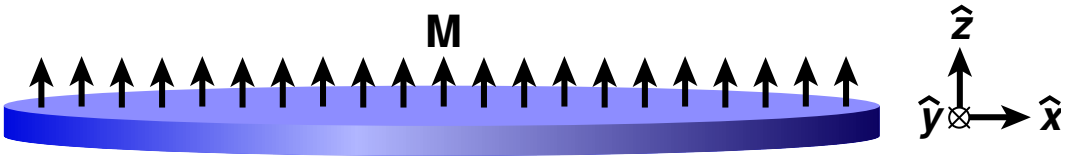


Figure 1.5: A very large, very flat magnetic disc, with the magnetization uniformly pointed out of the plane under no applied field. What is the field at the center?

at the surface currents.[11] With the magnetization uniformly pointing up, all the spins point down.[12] Stokes' theorem says that all the internal circulating currents associated with these spins cancel (more or less), and what remains is a loop of current running around the outside edge of the disc. As the radius of this disc approaches infinity, the field at the center (pointed vertically, as generated by this current) approaches zero.

This simple question illustrates an important and often forgotten point. The real magnetic field generated by a ferromagnet comes from the cooperating currents of its constituent electrons. If the magnetization of Fig. 1.5 lies *in* the plane of the disc, the surface currents along the top and bottom generate a much larger internal field, and as a result, the spins all have a lower potential energy. This *real* field generated by the geometry of the magnet is referred to as the "shape anisotropy" field. When **M** points out of plane (along $\hat{z}$ in Fig. 1.5), this field is zero, and as **M** rotates into the plane (toward $\hat{x}$), this field (always in the plane for this geometry), increases toward a saturation value equal to $\mu_0 M_s$[13], where M_s is the saturation magnetization. The material parameter M_s ($\mu_0 M_s \approx$ 1-2 T,

[11] I share in many people's distaste for fictitious surface charges and the unphysical quantities **M** and **H** that can lead to strange intuitions.

[12] They're negatively charged after all, a point that is usually ignored in spin transfer talks.

[13] This can quickly be shown by symmetry.

depending on the ferromagnet) represents the maximum field the spins are capable of generating by themselves. The surface current density in this geometry for $\mathbf{M} = M_x\hat{x} + M_z\hat{z}$ is proportional to M_x, so the anisotropy field $\mathbf{B}_{anisotropy}$ inside the magnet is

$$\mathbf{B}_{anisotropy} = \mu_0 M_x \hat{x}. \tag{1.1}$$

Or, for arbitrary $\mathbf{M}$ in Fig. 1.5,

$$\mathbf{B}_{anisotropy}/\mu_0 = (1.0)M_x\hat{x} + (1.0)M_y\hat{y} + (0.0)M_z\hat{z}. \tag{1.2}$$

We have written this equation in a way suggestive of the fact that this geometry is a simple case of a more general formalism we will discuss shortly. Because of this self-generated field, the magnet has potential energy density $U_{anisotropy} = -(1/2)\mathbf{M} \cdot \mathbf{B}_{anisotropy}$.[14] We emphasize here that $\mathbf{B}_{anisotropy}$ is the physical field that the spins (and everything else in the neighborhood) experience.[15] Due to the spins' own angular momentum, they tend to precess around this field, and through various dissipation mechanisms (referred to as "magnetic damping") they tend to relax to the minimum-$U_{anisotropy}$ configuration, as discussed momentarily.

The field $\mathbf{B}_{anisotropy}$ is not what is quoted in literature, however. To put Eq. 1.2 in the traditional literature form, we introduce a fictitious field $\mathbf{B}_{fiction} = -\mu_0\mathbf{M}$ to the system, which exists only inside the ferromagnet (and somehow *stops* at its boundaries). Since by our definition it always points antiparallel to $\mathbf{M}$ everywhere, its only effect on the system is to redefine the zero point of the potential energy.[16]

[14]The factor of 1/2 comes from the fact that $\mathbf{B}_{anisotropy}$ depends on $\mathbf{M}$. An externally applied field $\mathbf{B}_{external}$ does not, and the energy is $-\mathbf{M} \cdot \mathbf{B}_{external}$.

[15]Outside a nanomagnet, this field (which can influence other nanomagnets nearby) is often referred to as the "dipole field".

[16]This trick of adding $\mathbf{B}_{fiction}$ will go a long way in converting between the different notations in literature.

Combining this with the real field $\mathbf{B}_{anisotropy}$ defines the "demagnetizing" field[17]

$$\mathbf{B}_{demag}/\mu_0 = -N_{xx}M_x\hat{x} - N_{yy}M_y\hat{y} - N_{zz}M_z\hat{z}, \tag{1.3}$$

where $N_{xx} = 0$, $N_{yy} = 0$, and $N_{zz} = 1$ in this case. As it turns out, the N's defined in this way are the diagonal elements of a very general anisotropy tensor N_{ij} describing the demagnetization field for any shape and arbitrary $\mathbf{M}$.

For the simple case of a magnetic ellipsoid (which we generally use to approximate our magnetic layers), the anisotropy tensor is exactly diagonal and very easy to deal with. We can quickly get intuition about the magnet by looking at the relative magnitudes of the diagonal elements N_{ii}. If N_{xx} is the smallest, $\mathbf{M}$ will prefer the $\pm\hat{x}$-direction. If N_{zz} is the largest, the $\pm\hat{z}$-direction will be the direction of highest energy for $\mathbf{M}$. Figure 1.6a shows a sketch of one of the magnetic layers in our devices, an elliptical thin disc. For this geometry, N_{zz} is close to 1, N_{xx} is less than N_{yy}, and $\mathbf{M}$ will prefer to lie along the long, magnetically "easy" axis, as labeled. For $\mathbf{M}$ to rotate from $+\hat{x}$ to $-\hat{x}$, the smallest energy barrier to overcome is along the $\pm\hat{y}$, and it can be quickly shown that a coercive field of $\mu_0 M_s(N_{yy} - N_{xx})$ along $\pm\hat{x}$ is required to switch it.

It is also very illuminating to plot the contours of constant potential energy for $\mathbf{M}$, and project them onto the unit sphere, as shown in Fig. 1.6b. In the absence of magnetic damping, these contours are precisely the trajectories along which $\mathbf{M}$ will precess ($\mathbf{B}_{anisotropy}$ cannot do work on $\mathbf{M}$). Mathematically, this torque has the form

$$\partial\mathbf{m}/\partial t = -\gamma_0\mathbf{m} \times \mathbf{B}_{anisotropy} \tag{1.4}$$

[17]The term "demagnetizing" appeals to the notion that a given chunk of spins of a ferromagnet always apply a field $\mu_0 M_s$, and the geometry demagnetizes them by applying an opposing field. Since this formalism includes $\mathbf{B}_{fiction}$, we should pay attention to possible pitfalls of intuition when dealing with it.

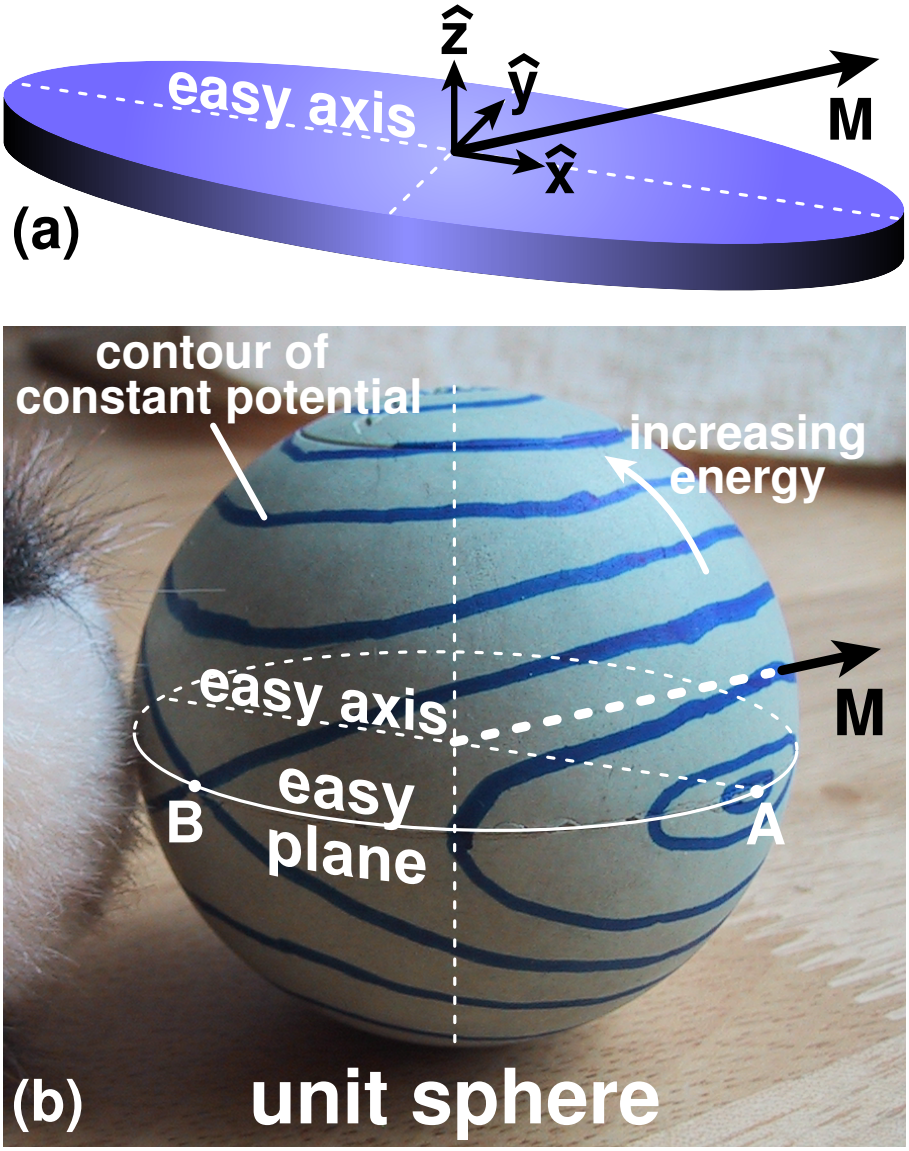


Figure 1.6: (a) Sketch of one of the magnetic layers in our devices, with the vector **M** denoting the magnetization. (b) The contours of constant magnetic potential energy (for the nanomagnet above) projected on the unit sphere. The magnetization **M** precesses along these contours, while while magnetic damping slowly relaxes it to the energy minimum, wherein **M** points in either direction along the long magnetic easy axis (labeled). Point A is a potential well, and point B is a saddle point.

where $\mathbf{m}$ is a unit vector pointing along $\mathbf{M}$, and γ_0 is a constant, the magnitude of the gyromagnetic ratio[18]. If we now apply an external field $\mathbf{B}_{external}$, we get a different set of contours (a deformation of those in Fig. 1.6b), and

$$\partial\mathbf{m}/\partial t = -\gamma_0\mathbf{m} \times \mathbf{B}_{total} \tag{1.5}$$

with $\mathbf{B}_{total} = \mathbf{B}_{anisotropy} + \mathbf{B}_{external}$. In addition to this precession torque there is a magnetic damping torque that tends to relax the system. Damping points perpendicular to the contours, always downhill in energy. Mathematically, this behavior can be represented by a second, phenomenological term:

$$\partial\mathbf{m}/\partial t = -\gamma_0\mathbf{m} \times \mathbf{B}_{total} + \alpha\mathbf{m} \times (-\gamma_0\mathbf{m} \times \mathbf{B}_{total}) \tag{1.6}$$

Here α is a unitless parameter that is generally much smaller than unity. It can be shown that this form of the damping torque pushes $\mathbf{M}$ downhill at a rate proportional to the potential gradient. Roughly speaking, $1/\alpha \sim 100$ is the number of precession cycles it takes for the magnetization to ring down. The damping is also often written in a nearly equivalent "Gilbert" form

$$\partial\mathbf{m}/\partial t = -\gamma_0\mathbf{m} \times \mathbf{B}_{total} + \alpha\mathbf{m} \times \partial\mathbf{m}/\partial t, \tag{1.7}$$

which is the "Landau-Lifshitz-Gilbert" (LLG) equation of magnetic dynamics quoted in literature. While the damping parameter is phenomenological, I still personally prefer the previous form, the Landau-Lifshitz (LL) equation. In the LL form, the damping torque always physically represents energy dissipation, and when we add other terms to $\partial\mathbf{m}/\partial t$, this meaningful behavior is not affected. Of

[18]Intuitively speaking, the gyromagnetic ratio $\gamma = ge/2m_e$ (with e the electron charge, m_e the electron mass, and g the Landau g-factor) is the conversion factor between the torque on the electron's circulating charge ($\propto e$) and this torque's effect on the electron angular momentum ($\propto m_e$).

course, these are all generally small corrections ($\sim \alpha^2$) to the behavior of our systems, so I will not bore you further with my detailed feelings on the matter, except to mention that Mark Stiles *et al.* have recently flushed out a theoretical argument based on domain wall motion that predicts substantially different behavior from the two forms, concluding that the LL interpretation is likely more accurate [12].

Finally, including the spin transfer torque $\boldsymbol{\tau}$ discussed above, we have the generalized Landau-Lifshitz-Slonczewski "LLS" equation

$$\frac{\partial \mathbf{m}}{\partial t} = -\gamma_0 \mathbf{m} \times \mathbf{B}_{total} - \gamma_0 \alpha \mathbf{m} \times (\mathbf{m} \times \mathbf{B}_{total}) + \boldsymbol{\tau}. \tag{1.8}$$

At this point, we can begin to predict what will happen in our devices under different bias conditions. All of the measurements reported in this dissertation are performed at DC currents comparable to or less than the critical current, and so the spin transfer torque is always comparable to or less than the damping. Consequently, all of the torques in Eq. 1.8 are small compared to the precession term, and any steady-state magnetic trajectories we expect to excite should be only *tiny* distortions of the energy contours predicted by this formalism. This notion is at the heart of a nice paper using bifurcation theory in our systems [13], which is an excellent way to quickly understand our magnetic dynamics.

In chapters 2 and 3, we apply a magnetic field along the easy axis of the device (in the $\hat{x}$-direction of Fig. 1.6). At zero (net[19]) field, both directions along the x-axis are stable, and we indeed see magnetic switching. Increasing the field from zero, the potential well marked "A" in Fig. 1.6 deepens, and the saddle point "B" (along with the one on the opposite side of the sphere) moves backwards along the equator toward $-\hat{x}$, shallowing the potential well at $-\hat{x}$ until it finally becomes

[19]The fixed layer tends to apply a static fringe field on the free layer (the dipole field) that favors the AP alignment.

unstable. This generates a set of contours predicting small-angle precession as well as the larger "clam-shell-shaped" and the out-of-plane trajectories discussed in chapter 2. To find out if these trajectories are theoretically stable, we could simply integrate the average effect of the damping and spin torque over each energy contour, and construct a complete dynamical stability phase diagram as in Ref. [13].

We can also use Eq. 1.8 to quickly estimate the small-angle dynamical behavior by linearizing about the equilibrium. This is precisely what is done in chapters 4 and 5 to extract useful information from our ferromagnetic resonance spectra.

Finally, we should note that magnetic materials often also contain an additional anisotropy energy due to the underlying atomic lattice's effect on the electron orbitals. In alloys like nickel-iron or cobalt-iron, this is not a large effect, so we mostly ignore it. Just be aware that there are other sources of anisotropy that can distort the energy contours of Fig. 1.6.

The picture outlined here is great for getting fast qualitative insight into the system, but we should also keep in mind that the magnetization is generally not uniform, and cannot be represented by a single vector $\mathbf{M}$ as we have assumed. In reality, nanomagnets such as that of Fig. 1.6a consist of many strongly-coupled spins distributed across the layer. Similar to a drumhead, the normal oscillatory modes we expect from such a system are actually spin waves confined by the (open) elliptical boundary conditions we define lithographically. Only the fundamental, lowest frequency mode (which is the most uniform) behaves much like a single spin on any quantitative level (chapters 4 and 5). The higher-order modes contain more and more variations in $\mathbf{M}(x, y, z)$ and, due to the exchange field, precess at higher frequency. Furthermore, complicated phase relationships can develop

between different pieces of the magnet, which in turn can affect a mode's coupling to spin currents. Needless to say, a system of many coupled spins is quite difficult to deal with, and the formalism presented above is only a starting point.

1.4 Context of This Dissertation

The field of spin transfer is full of rich and varied work in theory and experiment alike. This section attempts to highlight some of the important developments in the field, focusing specifically on work relevant to this dissertation. Hopefully it will provide a reader new to the field with a reasonable understanding of the predictions, questions, and answers central to our experiments.

In 1996, Slonczewski and Berger [2, 3] predicted a new effect in which electrons flowing through nanoscale magnetic multilayers could transfer spin angular momentum from one magnetic layer to another, thereby applying a substantial torque to the magnetizations. The efficiency of this "spin transfer" process was expected to increase as magnetic structures shrank, so that if the magnetic volumes involved were small enough, a reasonable amount of electrical current could reverse a magnetization entirely or excite spontaneous microwave-frequency magnetic oscillations. Two years after these initial predictions, the first experimental demonstrations of this spin transfer began to appear.

In 1998, Tsoi *et al.* [14] drove large DC currents (up to 10^9 A/cm^2, at 4.2 K) through a needle-tip point contact to extended magnetic multilayers, and observed peaks in the device's differential resistance, appearing at bias values that shifted linearly with the applied magnetic field. Based on this and a comparison with microwave absorption spectra on the thin films alone) they argued these changes in resistance corresponded to spontaneous magnetic oscillations driven by spin trans-

fer. The following year, J. Z. Sun demonstrated the first current-driven bistable magnetic switching in magnetite trilayer junctions (patterned to several microns in diameter) at < 20 K [15], and Myers *et al.* demonstrated the same effect in point contacts to extended Py- and Co-based multilayers [10]. Myers *et al.* even observed stable room-temperature switching in one Py/Cu/Co device, but generally the active magnetic grains in such systems were thermally unstable, and varied in character from sample to sample. In 2000, Katine *et al.* [11] demonstrated current-driven switching at room temperature in magnetic Co/Cu/Co thin film multilayers, patterned into well-defined "nanopillars" roughly 100 nm in diameter. Similar results were subsequently seen by other groups in similar systems [16, 17] the following year. These seminal experiments both demonstrated the validity of spin transfer theory and demonstrated the possibility of such device applications as ST-MRAM discussed above.

Both point contacts and nanopillars exhibited behavior like that observed by Tsoi *et al.* At higher magnetic fields and large enough currents, the devices underwent reversible transitions in resistance to values in between that of the antiparallel and parallel configurations. At the time, such transitions were attributed to the spontaneous magnetic oscillations driven by spin transfer, but there was no direct evidence to support this. In the year 2000, Tsoi *et al.* [18] first began to probe this regime by bathing their point contacts in microwave radiation, thereby coupling $\sim$ 50-GHz microwave current into the contact via the antenna action of the needle. By turning on the microwaves, new peaks in differential resistance appeared that were associated with magnon excitations. This experiment demonstrated that large DC current combined with microwave fields and currents could excite magnetic oscillations in these systems, but did not directly prove that the

system precessed spontaneously under DC current alone.

By this time it was generally accepted that spin transfer could be used to switch and manipulate nanoscale magnets, and also that the intermediate resistance states under high bias and field corresponded to changes in the magnetization. It was not clear, however, whether these DC-driven states corresponded to steady magnetic oscillations or something else entirely (perhaps rapid thermally-activated switching [19] or a static non-uniform magnetic state). Also, if this regime did in fact correspond to magnetization dynamics it was not clear whether the oscillations were spatially uniform and coherent [20] or non-uniform [21] and/or quasichaotic [22]. Additionally, there was still some confusion about the actual form of the spin transfer torque, whether it pointed in the plane defined by the two magnetizations involved [2, 3] or perpendicular to the plane [23].[20]

In order to test these different possibilities, in 2003 we developed a new microwave technique to unambiguously measure the magnetic oscillations in this regime electrically (should they exist, of course). The technique was straightforward: We applied DC current through a Co/Cu/Co magnetic nanopillar (similar in composition to Katine's) and measured the spectrum of magnetoresistance oscillations induced by magnetic precession. Using only DC current and field, we successfully demonstrated that the intermediate resistance regime corresponded to spontaneous magnetic precession, expressed in our measurement as peaks in the microwave spectra emitted by the sample. Furthermore, by comparing the peak frequencies and amplitudes to the results of a uniform-magnetization simulation, we were able to qualitatively identify steady-state small- and large-angle magnetic precession. The peaks in differential resistance, however, turned out to

[20]See also Ref. [24] from 2004

correspond to *transitions* between different dynamical and static magnetic states. These results are the focus of chapter 2.

Our observation of coherent large-angle magnetic precession was quite a surprising result, since magnetic precession in larger thin films was previously limited to small angles due to the instability (where large-angle uniform precession parametrically pumps energy into higher-order spin waves) predicted by Suhl [25]. In this experiment, we had directly observed a new type of magnetic oscillation never seen before. Furthermore, a spin-transfer torque pointing entirely perpendicular to the magnetization plane most likely would not have driven such oscillations, so we had also indirectly provided evidence that there must be a substantial component of the torque in the direction predicted by Slonczewski.

Our 2003 measurement raised a few new questions, too. First, our simulation predicted two distinct types of large-angle dynamical modes, whereas we observed only one experimentally. At fields and currents where the simulation predicted the second large-angle mode we found only a strange intermediate-resistance state that generated very little microwave signal. This could not be explained by our macrospin model, and was most likely due to the non-uniform character of the magnetization. Berkov *et al.* [26] has since made progress in explaining this regime with full micromagnetic simulations, and more recent measurements on Py-based samples has demonstrated the second large-angle mode [27].

Another discrepancy between our experiment and simulation was the coherence time of the oscillations. The measured spectral peak linewidths (related to the inverse coherence time) were broad, between 0.5 and several gigahertz, while our zero-temperature macrospin simulation predicted oscillations that were perfectly coherent, with zero linewidth. In 2004, Rippard *et al.* performed this spectral

measurement on point contact devices, and observed linewidths orders of magnitude narrower. It was not well understood why some devices or dynamical modes exhibited more coherent dynamics than others, or what mechanisms were involved in the decoherence. The origins could have been micromagnetic in nature, or due to thermal fluctuations [28, 29], or both.

In order to try and understand what mechanisms were important in decoherence, we studied the temperature (T) dependence of the linewidth for small-angle precession (discussed in chapter 3). The linewidth decreased substantially upon cooling our samples from room temperature to 20 K. By including temperature in the macrospin model, we derived two expressions for the contributions from thermal fluctuations: one linear in T (negligible in this case, arising from a random walk along the precession trajectory) and one proportional to $T^{1/2}$, derived by assuming a Boltzmann distribution of precession angles. The dominant $T^{1/2}$ term seemed to capture the temperature-dependence for $T < 100$ K with one fitting parameter (the scale), but the observed linewidths were substantially narrower than could be predicted by any reasonable simulation we performed within this model. This led us to the surprising conclusion that the true spatially-nonuniform oscillations in the experiment may be naturally more coherent than the macrospin model suggests. Still, we suspect that the predicted $\propto T^{1/2}$ contribution to the linewidth is fairly general, because it follows from Boltzmann statistics applied to the precession amplitude fluctuating around an (approximately) equilibrium value. Our expressions are certainly useful in predicting general trends in coherence with respect to different system parameters (magnetic volume, damping, precession angle, etc.). For instance, in Rippard's point contact geometry, a much larger magnetic volume (the magnetic films are not patterned) is excited to very large angles, both

of which are predicted to improve coherence.

For $T > 100$ K, however, the linewidth increased much more rapidly than could be captured by this simple model. In the same experiment, we also argued that by also allowing the system to occasionally escape the dominant oscillatory mode (over an effective energy barrier), the full temperature dependence of the observed coherence could be explained with one or two more fitting parameters. We reported direct evidence for this hopping effect from a sample in which, under some bias conditions, more than one mode appeared in the spectrum. Whenever two modes appeared simultaneously, the linewidths of both increased dramatically. By including this effect in the temperature dependence, we had probed the effective barriers separating different magnetic modes without even knowing the details of the modes involved.

At this point, the spin transfer effect was widely accepted; both switching and spontaneous oscillations predicted by the theory had been observed, and we had begun to understand the mechanisms limiting coherence in the oscillations. Meanwhile, several experiments had started to refine estimates the actual strength and form of the spin-transfer torque (along with damping) in these systems. In 2004, Koch *et al.* [28] performed a time-resolved switching measurement, and by comparing with the macrospin model, estimated the magnitude of the spin torque and damping. Braganca *et al.* [30] also estimated these quantities by studying the pulsed-switching probabilities. In magnetic tunnel (as opposed to metallic) junctions, Fuchs *et al.* [31] were able to estimate the magnitude of the torque by measuring changes in the thermally-activated switching lifetime under different bias conditions (2005). In these three switching experiments, the torque (and damping) were rather laboriously and indirectly estimated through comparisons

with the macrospin model, though there were likely many different dynamical modes involved in these (large-angle) switching process. Also in 2005, Krivorotov *et al.* [32] performed time-resolved measurements of both dynamics and switching in metallic junctions, and were similarly able to get a rough estimate of the torque (or spin polarization). They were also able to more directly (but still laboriously) estimate the damping parameter by measuring the decay time of small-angle oscillations under bias and then extrapolating to zero bias. This technique assumed the linear bias-dependence of the effective damping predicted by Slonczewski's theory, which was yet unproven through direct experiment.

At this point, no one had found a way to directly measure these physical quantities, and so it remained a central issue. Additionally, in the wake of improving micromagnetic simulations [26, 33, 34], it was still not clear precisely what set of modes were excited by DC currents. In 2005, Tulapurkar *et al.* [35] and our group independently developed a new form of ferromagnetic resonance (FMR) driven by the spin transfer torque, which would allow us to address these issues, as well as demonstrating the feasibility of FMR in much smaller systems than had been probed before.[21] In these experiments, we applied microwave-frequency spin currents and measured the magnetic response with a resonant (DC) nonlinear mixing voltage.

For metallic spin-valves (discussed in chapter 4), we observed several normal resonance modes, more than appeared in the DC-driven experiment, from both magnetic layers. We achieved an efficient and direct measurement of the magnetic damping parameter from the dominant low-frequency FMR peak linewidth[22], and

[21] We published in 2006.

[22] The linewidth of this ac-driven experiment is proportional to magnetic damping, and not directly related to oscillation coherence.

confirmed over a large bias range (including zero) its predicted linear bias dependence. As predicted, the effective damping approached zero at the critical bias for spontaneous DC-driven oscillations. By monitoring the different normal modes' evolution through this bias point, we were able to confirm that the various DC-driven modes seen before corresponded to a subset of the normal magnetic modes. Using the resonance lineshape we were also able to observe a regime of ordinary FMR (below the critical bias) and a regime of phase-locking between the microwave current and the large-angle DC-driven modes, which was consistent with observations from a different technique performed by Rippard *et al.* [36] in 2005. The most exciting aspect of this measurement, though, is that the observed behavior of the lowest-frequency, dominant resonance mode agreed quite well with predictions for a uniform mode, enabling a very simple physical interpretation of the data. At this time, however, our technique for calibrating the microwave current was not reliable enough to make estimates of the actual magnitude of the spin transfer torque, but our observed resonance line *shapes* implied that the torque in these metallic junctions was strongly confined to the magnetization plane as predicted by Slonczewski, even under bias.

This result contrasted with the conclusions of Tulapurkar *et al.* [35], who observed more complicated FMR line shapes (in MgO-based tunnel junctions), and interpreted this structure as arising from a strong perpendicular component of the torque. Our results suggested that either their lineshapes (most likely) arose from a superposition of two normal modes from the different layers (similar to the modes we had observed) or that the physics behind spin transfer in tunnel junctions was drastically different than Slonczewski's predictions [37]. If Slonczewski was correct, there should have been very little (or zero) perpendicular torque due to small

biases, but this component should have increased as the square of the applied DC voltage (Tulapurkar's measurement was restricted to zero bias). Slonczewski's theory also included parameters such as the spin-dependent conductances that were not well understood experimentally. Different assumptions about the system yielded different expectations for the magnitude and bias-dependence of the spin transfer torque.

In order to address these questions, we performed the spin-transfer-driven FMR technique on MgO-based junctions similar to Tulapurkar's (discussed in chapter 5). Armed with a much improved microwave-current calibration technique, we were able to use our resonance line shapes and magnitudes to make the first direct measurement of both components of the spin transfer torque separately. Our lock-in technique also allowed us to study the bias dependence of the two torque components. Our first major result was that, in contrast to Tulapurkar *et al.*, at zero bias we observed only the predicted in-plane component. Second, upon increasing the bias, the perpendicular component grew to $\sim 30\%$ the size of the in-plane component, scaling as the voltage squared, also as predicted. Interestingly, from this direct measurement (and independently from the bias dependence of the damping) we estimated that the torque is very close to the maximum possible value predicted from elastic scattering processes, implying that further improvements in materials will likely not markedly improve the torque's efficiency. We also observe a substantial increase in the efficiency of the torque at high bias, which might be due to heating, or could be an indication of changes in inelastic scattering due to magnons. This is still a work in progress, and even after we publish, our results will likely prompt substantial new theoretical and experimental study of these nanoscale systems.

Chapter 2

Microwave Oscillations of a Nanomagnet Driven by a DC Spin-Polarized Current

The contents of this chapter are adapted from work originally published as *Nature* (London) **425**, 380, (2003).

2.1 Introduction

As discussed in the introductory chapters, spin-polarized electrons can apply a large and efficient torque to a ferromagnet through direct transfer of spin angular momentum. This offers the possibility of manipulating magnetic-device elements without applying cumbersome magnetic fields (that require large currents to generate and are not easy to localize) [2, 3, 10, 11, 14–16, 18, 38–45]. In this chapter we take the first steps toward understanding what type of magnetic motions can be generated by this torque.

Theory predicts that above a critical value of the applied current (where the spin transfer torque first overcomes the magnetic damping torque [11]), spin transfer can drive a nanomagnet into types of oscillatory magnetic modes not attainable with magnetic fields alone [2, 3, 38]. Before the measurements described in this chapter were performed, however, existing experimental techniques had provided only indirect evidence of such dynamical states [10, 11, 14, 18, 41, 43–45], and the nature of these modes had not been determined.

Here we demonstrate a technique that allows direct electrical measurements of microwave-frequency dynamics in individual nanomagnets, propelled by a DC

spin-polarized current. We show that spin transfer can produce several different types of magnetic excitations, identifiable by the corresponding spectral features' magnitude and the dependence of their frequencies on bias and field. Although there is no mechanical motion, a simple magnetic multilayer structure acts like a nanoscale motor; it converts energy from a DC electrical current into high-frequency magnetic rotations that might be applied in new devices including microwave sources and resonators.

2.2 Devices and Apparatus

We examine samples made by sputtering a multilayer of composition 80 nm Cu / 40 nm Co / 10 nm Cu / 3 nm Co / 2 nm Cu / 30 nm Pt onto an oxidized silicon wafer and then milling through part of the multilayer (Fig. 2.1a) to form a pillar with an elliptical cross-section of lithographic dimensions 130 nm $\times$ 70 nm [1]. Top contact is made with a Cu electrode. Transmission or reflection of electrons from the thicker "fixed" Co layer produces a spin-polarized current that can apply a torque to the thinner "free" Co layer. Subsequent oscillations of the free-layer magnetization relative to the fixed layer change the device resistance [46] so, under conditions of DC current bias, magnetic dynamics produce a time-varying voltage (with typical frequencies in the microwave range). If the oscillations were exactly symmetric relative to the direction of the fixed-layer moment (but confined to the plane), voltage signals would occur only at multiples of twice the fundamental oscillation frequency, f. To produce signals strength at f, we apply static magnetic fields (H) in the sample plane a few degrees away from the magnetically easy axis of the free layer. All data are taken at room temperature, and by convention positive I denotes electron flow from the free to the fixed layer.

In characterization measurements done at frequencies <1 kHz, the samples exhibit the same spin-transfer-driven changes in resistance reported in previous experiments [11, 16] (Fig. 2.1b). For H smaller than the coercive field of the free layer ($H_c \approx 600$ Oe), an applied current produces hysteretic switching of the magnetic layers between the low-resistance parallel (P) and high-resistance anti-parallel (AP) states. Sweeping H can also drive switching between the P and AP states (Fig. 2.1b, inset). For H larger than 600 Oe, the current produces peaks in the differential resistance dV/dI that have been assumed previously to be associated with dynamical magnetic excitations [10, 11, 14, 18]. The resistance values displayed in Fig. 2.1b include a lead resistance of $\approx 6\ \Omega$ from high-frequency (50 GHz) probes and a top-contact resistance of $\approx 9\ \Omega$.

We measure the spectra of microwave power that results from the free layer magnetic motions by using a heterodyne mixer circuit [47] (Fig. 2.1a). This circuit differs from the only previous experiment on spin-transfer-driven magnetic oscillations [18] in that the sample is not exposed to a large high-frequency magnetic field that could alter its dynamics. The filter on the output of our mixer passes 25-100Mhz, giving a frequency resolution of ≈ 200 MHz. We calibrate the circuit by measuring temperature-dependent Johnson noise from test resistors. When we state values of emitted power, they will correspond to the power available to a load matched to the sample resistance, R. To convert to the power delivered to a 50-Ω line, one should multiply our values by the power transmission coefficient $1 - \Gamma^2 = 1 - (R - 50\ \Omega)^2/(R + 50\ \Omega)^2$.

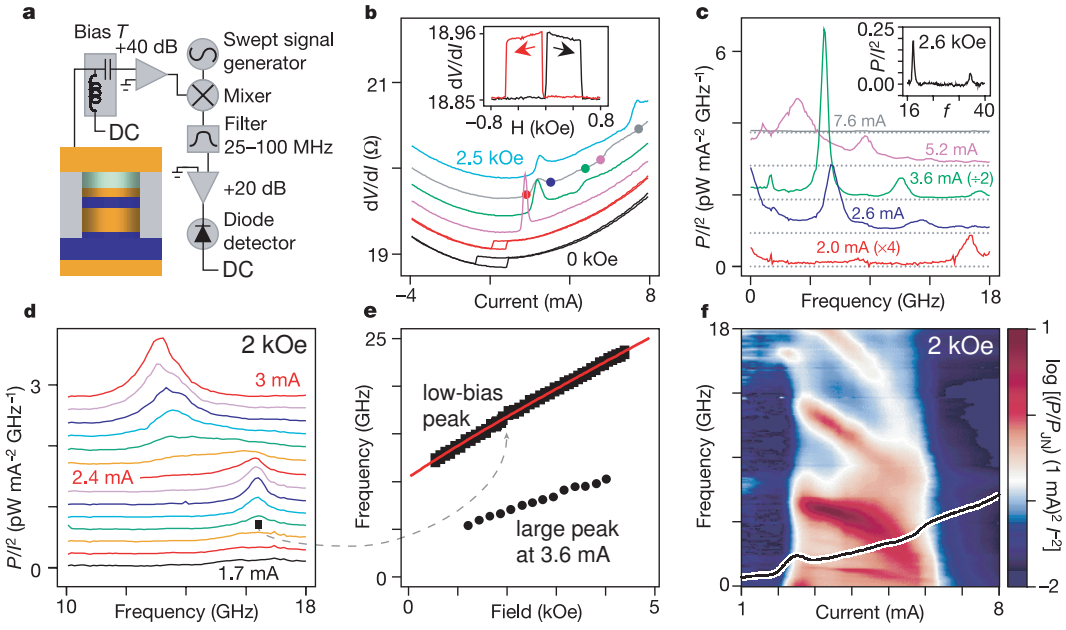


Figure 2.1: Resistance and microwave data for sample 1. (a) Schematic of the sample and the heterodyne mixer circuit. (b) (offset vertically) dV/dI versus I for H = 0, 0.5, 1.0, 1.5, 2.0, and 2.5 kOe, with current sweeps in both directions. At H = 0, the switching currents are I_c^+ = 0.88 mA and I_c^- = -0.71 mA, and ΔR_{max} = 0.11 Ω between the P and AP states. Colored dots on the 2 kOe curve correspond to spectra in (c). (inset) dV/dI near I = 0. (c) (offset vertically) Microwave spectra with Johnson noise P_{JN} subtracted at H = 2 kOe, for several values of I. (inset) Spectrum at H = 2.6 kOe and I = 2.2 mA, where f and $2f$ peaks are visible on the same scan. (d) (offset vertically) Spectra at H = 2.0 kOe, for I = 1.7 to 3.0 mA in 0.1 mA steps, showing the growth of the small-amplitude precessional peak and then a transition to the large-amplitude regime (2nd harmonic). (e) Field dependence of the low-bias peak frequency (top) and the large-amplitude regime (first harmonic) at I = 3.6 mA (bottom). The line is a fit to Eq. 2.1 (f) Microwave power versus frequency and current at H = 2.0 kOe. The black line shows dV/dI versus I from (b).

2.3 Data and Analysis

We first consider the microwave spectrum from sample 1 for $H = 2$ kOe. For both negative I and small positive I we measure only frequency-independent Johnson noise power P_{JN}. We subtract this background from all spectra we display. At $I = 2.0$ mA, we begin to resolve a microwave signal at 16.0 GHz (Fig. 2.1c, d). A second-harmonic peak is also present (Fig. 2.1c, inset). As I is increased, these initial signals grow until $I \approx 2.4$ mA, beyond which the dynamics change to a different regime (Fig. 2.1d). In Fig. 2.1e, we compare the H-dependence of the measured frequency for the initial signals to the formula for small-angle elliptical precession of a thin-film ferromagnet [48]:

$$f = \frac{\gamma}{2\pi}\sqrt{(H + H_{an} + H_d)(H + H_{an} + H_d + 4\pi M_{eff})} \tag{2.1}$$

Here γ is the gyromagnetic ratio, H_{an} accounts for a uniaxial easy-axis anisotropy, H_d models the coupling from the fixed layer, and $4\pi M_{eff} = 4\pi M_s - 2K_u/M_s$, with M_s the saturation magnetization and K_u a uniaxial perpendicular anisotropy [49]. Here we have assumed for simplicity that the free layer behaves as a uniform magnetization (the "macrospin" approximation). The true magnetic excitations in our elliptical devices most likely contain spatial variations in the free layer's magnetization, shifting the precession frequency to higher values through the exchange field [50]. Still, the fit is excellent and gives the values $4\pi M_{eff} = 6.8 \pm 0.1$ kOe and $H_{an} + H_d = 1.18 \pm 0.04$ kOe. The value for $4\pi M_{eff}$ is less than $4\pi M_s$ for bulk Co (16 kOe) as expected due to significant perpendicular anisotropy in Co/Cu(111) films (see Fig. 3 in [51]). Similar fits for other samples yield $4\pi M_{eff}$ in the range 6.7-12 kOe. Superconducting quantum interference device (SQUID) measurements on test samples containing many 3-nm Co layers give $4\pi M_{eff} = 10 \pm 1$ kOe.

On the basis of the agreement with equation 2.1 we identify the initial signals as arising from small-angle elliptical precession of the free layer, thereby confirming pioneering predictions that spin transfer can coherently excite this uniform spin-wave mode [3]. We can make a rough estimate for the amplitude of the precession angle, θ_{max} and the misalignment angle θ_{mis} (induced by the applied field) between the precession axis and the fixed-layer moment based on the integrated microwave power measured about f and $2f$ (P_f and P_{2f}). Because $4\pi M_{eff}$ is large compared to the in-plane anisotropy, the precession is strongly confined to the sample plane. Assuming for simplicity that $\theta(t) = \theta_{mis} + \theta_{max}\sin(\omega t)$, that the angular variation in resistance $\Delta R(\theta) = \Delta R_{max}(1-\cos(\theta))/2$ and that $|\theta_{mis} \pm \theta_{max}| \ll 1$, we calculate:

$$\theta_{max}^4 \approx \frac{512 P_{2f} R}{\Delta R_{max}^2 I^2} \tag{2.2}$$

$$\theta_{mis}^2 \approx \frac{32 P_f R}{\Delta R_{max}^2 I^2 \theta_{max}^2} \tag{2.3}$$

where $R = 12.8\ \Omega$ and $\Delta R_{max} = 0.11\ \Omega$ is the resistance change between the P and AP states. For the spectrum from sample 1 in the inset to Fig. 2.1c, we estimate that $\theta_{mis} \approx 9^\circ$, and the precessional signal first becomes measurable above $\theta_{max} \approx 10^\circ$.

With increasing currents, the nanomagnet exhibits additional dynamical regimes. As I is increased beyond 2.4 mA to 3.6 mA for sample 1, the microwave power grows by two orders of magnitude, peak frequencies shift abruptly, and the spectrum acquires a significant low-frequency background (Fig. 2.1c).[1] In many samples some spectral peaks are difficult to distinguish. Within this large-amplitude regime, peaks shift down in frequency with increasing current (Fig.

[1]Here this is not studied in great detail, but it is most likely a Lorentzian centered at zero frequency, due to rapid thermal activation discussed in chapter 3 and Ref. [52].

2.1f). The large-amplitude signals persist for I up to 6.0 mA, where the microwave power plummets sharply at the same current for which there is a shoulder in dV/dI. The state that appears thereafter has a DC resistance 0.04 Ω lower than the AP state and 0.07 Ω above the P state. At even higher current levels (not shown), we sometimes see additional large microwave signals that are not reproducible from sample to sample. These might be associated with dynamics in the fixed layer.

The regions of I and H associated with each type of dynamical mode can be determined by analyzing the microwave power and dV/dI (Fig. 2.2a, b for sample 2). In all eight samples we have examined in detail, large microwave signals occur for a similarly shaped range of I and H. Samples 1 and 2 exhibit clear structure in dV/dI at the boundaries of the large-amplitude regime, but other samples sometimes lack prominent dV/dI features over part of this border. In Fig. 2.2c we construct a dynamical stability diagram showing the different modes that can be driven by a DC spin-transfer current and a constant in-plane magnetic field. Explaining the existence of all these modes and the positions of their boundaries provides a rigorous testing ground for theories of spin-transfer-driven magnetic dynamics, as discussed below.

As indicated in Fig. 2.2c, d, microwave signals can sometimes be observed not only at large H where dynamical modes have been postulated previously [10, 11, 14, 18, 41, 43–45], but also in the small-H regime of currents at $H = 500$ Oe; for example, microwave peaks corresponding to small-angle precession exist for I within ~ 0.7 mA below the current for P to AP switching. Similar features are also observed before switching from AP to P at negative bias. This precession has also more recently been observed in these regions at low temperature (≈ 10 K) as

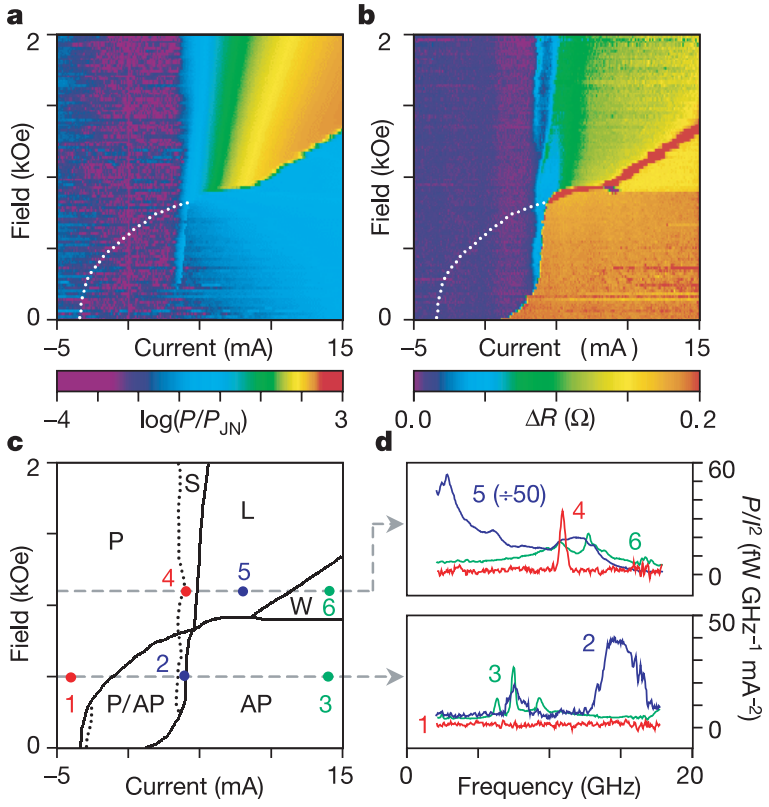


Figure 2.2: Data from sample 2, which has (at $H = 0$) $I_c^+ = 1.06$ mA, I_c^- = -3.22 mA, P-state resistance (including leads) 17.5 Ω, $\Delta R_{max} = 0.20\,\Omega$, and $4\pi M_{eff} = 12$ kOe. (a) Broadband (0.1-18 GHz measured with a detector diode directly after amplification) power versus I and H, for I swept negative to positive. The white dots show the position of the AP to P transition for I swept positive to negative. (b) dV/dI at the same values of I and H. A smooth I-dependent, H-independent background (similar to that of Fig. 2.1b) is subtracted emphasize the different regimes. Resistance changes ΔR are measured relative to P. (c) Dynamical stability diagram extracted from (a) and (b). P/AP indicates bistability, S and L the small- and large-amplitude dynamical regimes, and W a state of intermediate resistance and only small microwave signals. The colored dots in (c) correspond to the microwave spectra at $H = 500$ and 1100 Oe shown in (d).

well [53,54]. As discussed below, stable precession is indeed predicted in this region even excluding the effects of temperature. As discussed in Ref. [55], this precession can also be excited below the critical current by thermal fluctuations, deflecting the free-layer moment away from equilibrium far enough for us to measure but not far enough to excite over the activation barrier for switching [19]. Related signals have been observed recently in magnetic tunnel junctions [56].

To understand what type of motion may be associated with the different dynamical modes, we have computed solutions of the Landau-Lifshitz-Gilbert equation of motion for a single-domain magnet (similar to Ref. [20, 21, 57, 58]). We employ the form of the spin-transfer torque derived in [2]. The calculated zero-temperature dynamical phase diagram is presented in Fig. 2.3a, along with some representative trajectories. We have not attempted to adjust parameters to fit our data, but upon comparing with Fig. 2.2c, the existence and relative positions of the P, AP, and small-angle-precession regimes agree quite well. The exact locations of the boundaries depend strongly on the choice of parameters and the complicated details of the actual micromagnetic modes we excite. More recently, the curvature on the corners of the P/AP region not found in the simulation here has been qualitatively captured within the macrospin approximation by including thermal fluctuations [55], which can excite the magnetization over the potential energy barrier between the P and AP state.

Our simulation suggests that the initial microwave signals correspond to small-angle precession, and that the large-amplitude signals at higher bias correspond to large-angle, approximately in-plane precession of the free-layer moment (labeled "large angle" in Fig. 2.2). As shown in Fig. 2.3b, the simulation reproduces the

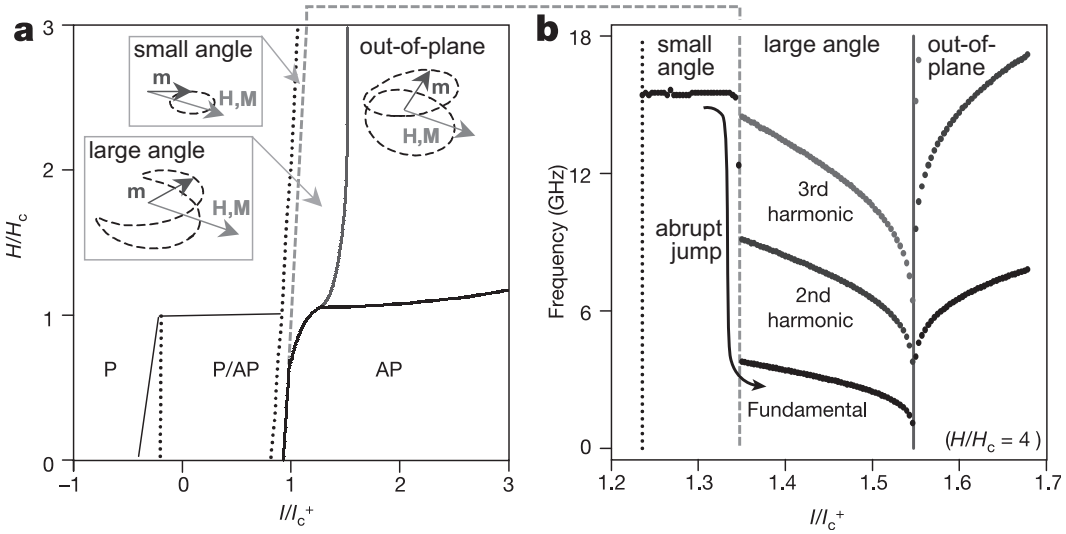


Figure 2.3: Results of numerical solution to the Landau-Lifshitz-Gilbert equation for a single-domain nanomagnet at zero temperature. The parameters are: $4\pi M_{eff} = 10$ kOe, $H_{an} = 500$ Oe, Gilbert damping parameter $\alpha = 0.014$, and effective polarization $P = 0.3$, which produce $H_c = 500$ Oe and $I_c^+ = 2.8$ mA. (a) Theoretical dynamical stability diagram. The pictures show representative precessional trajectories of the free-layer moment vector **m** (the fixed layer moment vector **M** and applied field **H** remain static). For the "out-of-plane" case, the system chooses (depending on initial conditions) one of two equivalent trajectories above and below the sample plane. (b) Dependence of precession frequency on current in the simulation for $H = 2$ kOe, including both the fundamental frequency and harmonics in the measurement range. The vertical dividing lines correspond to the phase diagram boundaries of (a).

abrupt jump[2] to much lower frequency at the onset of this mode, as well as the decreasing frequency with further increases in current (compare with Fig. 2.1f). It also reproduces the large powers in the harmonics; the maximum simulated microwave powers for this mode in the 0-18 GHz bandwidth are 18 pW mA^{-2} for sample 1 and 75 pW mA^{-2} for sample 2 (differing primarily because of different ΔR_{max} values), whereas the measured maxima are 10 and 90 pW mA^{-2}, respectively. Low-frequency backgrounds in the large-amplitude spectra (for example, Fig. 2.2d, spectrum 5) are not reproduced by this simulation, and are likely due to telegraphing between the dominant large-angle dynamical mode and other modes nearby in energy [21, 52, 54]. The simulation also does not explain the state W. We suspect our single-domain approximation becomes invalid in the regime W (perhaps owing to dynamical instabilities [25, 60]), and that different regions of the sample may move in a fashion that tends to cancel the overall resistance oscillations. More recent micromagnetic simulations have been employed with some success in order to qualitatively explain this regime [26].

2.4 Conclusions

In this chapter we discussed the first unambiguous direct measurement of magnetization dynamics driven by DC spin-polarized currents in individual nanomagnets. We applied DC current and measured the corresponding microwave-frequency resistance oscillations with a spectrum analyzer, confirming predictions that the in-

[2]In the simulation for this device, the "jump" appears abrupt, but is actually continuous transition over a very short range. This is generally only true in the macrospin approximation. More recent data and micromagnetic simulations [59] illustrate that as the precession angle changes in these devices, the frequency often makes abrupt jumps corresponding to hops between different dynamical modes. Some evidence of this hopping is also reported in chapters 3 and 4.

termediate resistances correspond to a regime of magnetization dynamics. We compared the frequency and amplitude of the generated spectral peaks to a macrospin simulation and identified both small- and large-angle dynamical modes. We also reported several important discrepancies between the simulation and the observations, providing a rigorous testing ground for future spin transfer theory. The magnetic precession in this system can be quite large, generating a substantial fraction of the maximum possible power. For sample 1, the largest peak in the power spectrum has a maximum of more than 40 times larger than room-temperature Johnson noise. Nanomagnets driven by spin-polarized currents may one day serve as nanoscale microwave sources or oscillators, tunable by I and H over a wide frequency range.

Chapter 3

Mechanisms Limiting the Coherence of Spontaneous Magnetic Oscillations Driven By DC Spin-Polarized Currents

The contents of this chapter are adapted from work originally published as *Phys. Rev. B* **72**, 224427, (2005).

3.1 Introduction

As the previous chapter began to explore, a spin-polarized DC current can excite periodic oscillations in nanometer-scale magnetic multilayers even in the absence of any external oscillatory drive [5, 32, 61, 62] in agreement with predictions [2, 3]. The magnetic motions produce variations of the resistance $R(t)$ that, when measured with a spectrum analyzer, give peaks in the microwave power spectral density versus frequency (Fig. 3.1a). Deviations from perfect periodicity can be characterized by the time scale over which the oscillations lose phase coherence, related to the reciprocal of the linewidth. This scale is important both for a fundamental understanding of the dynamics and for applications including tunable nanoscale microwave sources and resonators [63]. The coherence quality has varied in previous experiments, with room-temperature linewidths ranging from a full width at half maximum (FWHM) of 550 MHz for Co layers in "nanopillars" to 2 MHz for Py ($Ni_{81}Fe_{19}$) films in point-contact devices [62, 64]. Here we investigate the processes that limit the coherence time of spin-transfer-driven precession by mea-

suring the dependence of linewidths on temperature and the proximity of similar magnetic modes. We argue that two fundamental mechanisms contribute: (a) thermal deflection of the magnetization about its equilibrium trajectory at low temperatures, and (b) rapid thermally-activated escape to other magnetic states at higher temperatures. Interestingly, by probing mechanism (b) we are able to estimate the effective energy barriers between different dynamical modes without actually knowing the details of the modes involved. Also, our observed linewidths are narrower than predicted by simple macrospin simulations, indicating that spatial variations in the magnetization may actually improve coherence.

3.2 Sample Geometry

We focus on devices having a nanopillar geometry (Fig. 3.1a, inset). The samples are composed of metal multilayers fabricated into elliptical cross sections using the procedure of Ref. [1, 61]. the devices that we examine have different sequences of layers (noted below), but all contain one thin Py "free" layer (2-7 nm thick) that can be driven into precession by spin-transfer torques and a thicker or exchange-biased "fixed" Py layer, which polarizes the current and does not undergo dynamics in the current range we discuss. When biased with a DC current I, motion of the free-layer magnetic moment results in a spontaneous microwave signal $IR(t)$ that we measure with a spectrum analyzer. Figure 3.1b is a dynamical phase diagram for device 1, determined from microwave measurements as in Ref. [61], with magnetic field H applied in plane along the magnetically easy axis. This device has the layer structure 80 nm Cu / 20 nm Py / 6 nm Cu / 2 nm Py / 2 nm Cu / 30 nm Pt, with an approximately elliptical cross section of 120 nm $\times$ 60 nm and a resistance of 6 Ω (low enough that ohmic heating [53] is negligible above 20 K). We will consider

the dynamical states near bias points corresponding to the dot in Fig. 3.1b where, as a function of increasing I, the sample evolves from a configuration in which the moments of the two magnetic layers are parallel (P) to a regime with small-angle precessional dynamics (SD), to a regime with larger-angle dynamics (LD).

3.3 Data and Analysis

We find that linewidths can vary significantly between samples of similar geometry, to a greater extent than the critical currents or the other aspects of spin-transfer-driven dynamics that have been analyzed previously. The differences between samples might be associated with film roughness, partial oxidation at the sample edges, or other effects. We will focus on the comparatively narrow lines. Figure 3.2a shows the measured temperature dependence of the FWHM of the peak in power density observed at twice the fundamental precession frequency in device 1.[1] Because the linewidth depends on the magnitude of the precession angle θ measured in plane (Fig. 3.2a, inset), as temperature T is changed we keep the average precession angle $\langle\theta\rangle$ approximately constant. For device 1, we do this by monitoring the power in the second harmonic, estimating $\langle\theta\rangle$ by using the procedure of Ref. [61] and adjusting I between 1.1 mA (25K) and 0.9 mA (170 K) to fix $\langle\theta\rangle$ near an estimated value of 32°, where the linewidth is a minimum in this device. The misalignment angle between the precession axis and the fixed layer magnetization (estimated from the first and second harmonic [61]) is $\theta_{mis} \sim 2°$. We find that the linewidth is strongly dependent on T, increasing by a factor of 5 between 25 and 170 K. We have observed qualitatively similar behavior in six

[1]The linewidths for device 1 approach a constant value below ∼20 K, as expected due to ohmic heating. See the heating estimate in Ref. [53].

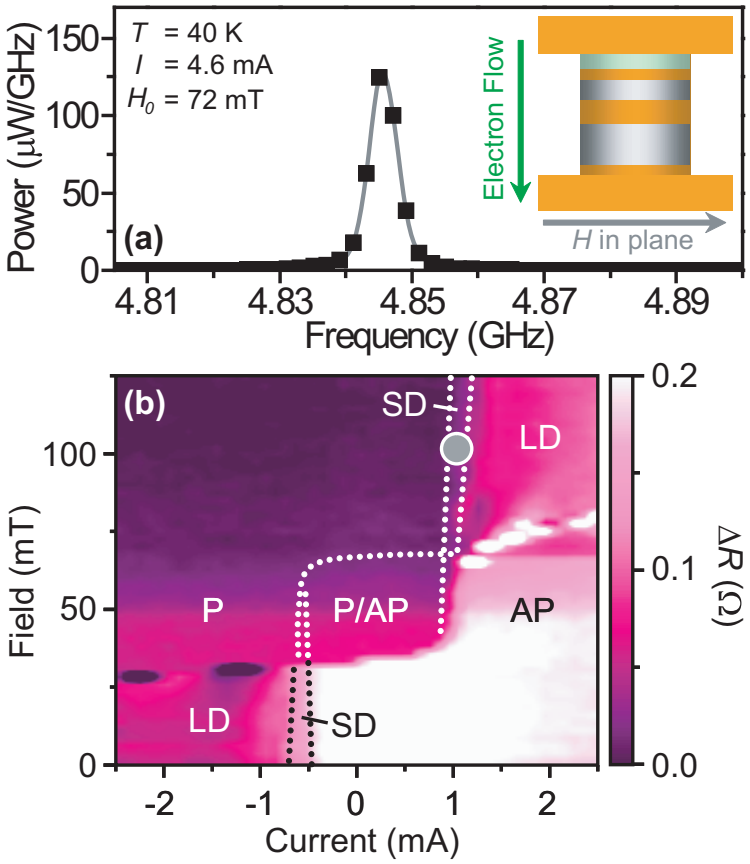


Figure 3.1: (a) A far narrower spectral peak from a nanopillar device than those reported prior to the original publication of this work (FWHM = 5.2 MHz) [54]. The device has the same composition as device 3, described in the text. (Inset) Schematic of a nanopillar device. (b) Differential resistance of device 1 as a function of I and H at $T = 4.2$ K, obtained by increasing I at fixed H. AP denotes static antiparallel alignment of the two magnetic moments, P parallel alignment, P/AP a bistable region, SD small-angle dynamics, and LD large-angle dynamics.

samples, throughout the region of the phase diagram where precessional excitations exist. Figure 3.2b shows results near the fundamental precession frequency for smaller-angle precession in device 2, composed of 80 nm Cu / 20 nm Py / 10 nm Cu / 7 nm Py / 20 nm Cu / 30 nm Pt, with cross section 130 nm × 40 nm, and resistance 20 Ω. The thicker free layer (compared to device 1) reduces some effects of thermal fluctuations and permits studies of the small-angle dynamics up to room temperature. Measurements at the fundamental precession frequency are possible even for small $\langle\theta\rangle$ in device 2, because of larger value of the offset angle θ_{mis} than in device 1. [2] The strong T dependence that we observe in all samples indicates that thermal effects determine the coherence time of spin-transfer-drive precession above 25K.

To analyze these results, we first consider the simplest model, in which the moment of the free layer is assumed to respond as a single macrospin. Theoretical studies of this model have been performed previously [20, 21, 29, 55, 58, 65], and good qualitative agreement has been found with both frequency- and time-domain measurements, with some exceptions at large currents [5, 27, 32, 61]. We integrate the Landau-Lifshitz-Gilbert (LLG) equation of motion with the Slonczewski form of the spin-transfer torque [9]. Thermal effects are modeled by a randomly fluctuating field $\mu_0 H_{th}$, with each spatial component drawn from a Gaussian distribution of zero mean and standard deviation $\sqrt{2\alpha k_B T/\gamma M_s V \Delta t}$, where α is the Gilbert damping parameter, k_B is Boltzmann's constant, γ is the gyromagnetic ratio, M_s and V are the magnetization and volume of the free layer, and Δt is the integration

[2] In this case we control the precession angle by monitoring the power at the fundamental, and estimate $\langle\theta\rangle < 12°$ for these data. At these small angles, we did not see a second harmonic above the noise floor of the measurements. The upper bound is estimated by assuming the second harmonic peak amplitude is the same size as the noise.

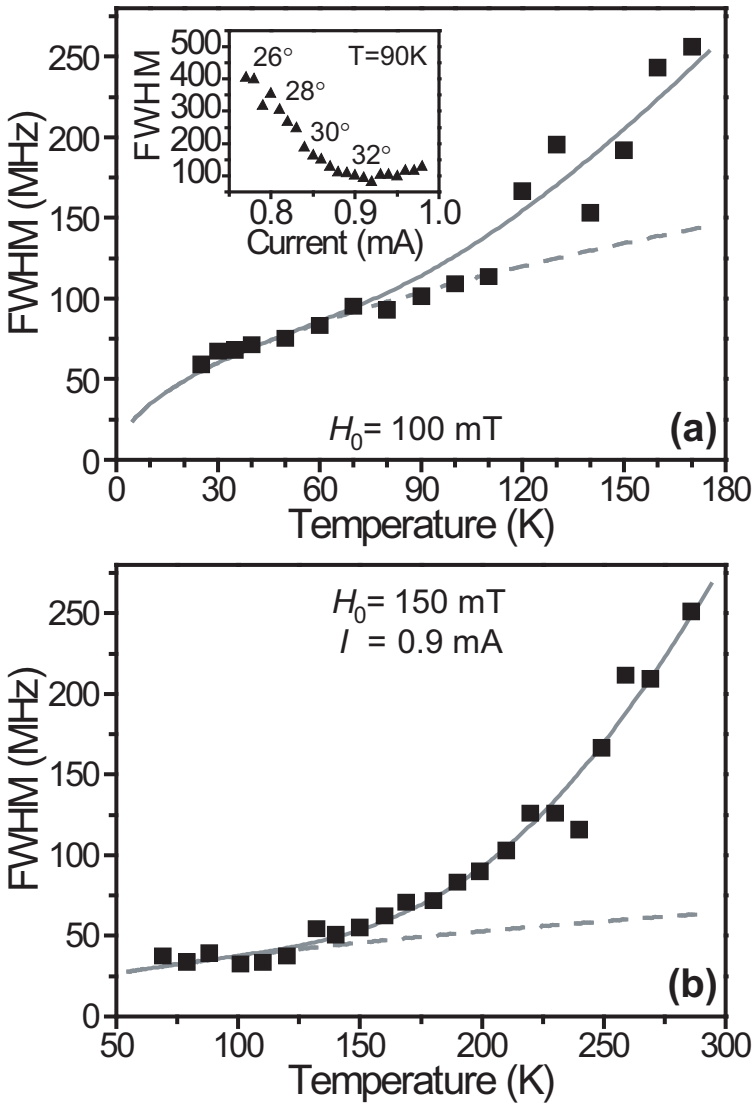


Figure 3.2: Measured linewidths vs T for (a) device 1 and (b) device 2. The dashed line is a fit of the low-T data to Eq. 3.2 and the solid line is a combined linewidth from Eqs. 3.2 and 3.3, obtained by convolution. (Inset) Dependence of linewidth on I for device 1, with estimates of precession angles.

time step [28,66]. Thermal fluctuations displace the moment both (i) along and (ii) transverse to the equilibrium trajectory. Fluctuations along the trajectory speed and slow the moment's progress, directly inducing a spread in precession frequency f. From the time needed for this random-walk process to produce dephasing, we estimate the contribution to the FWHM from mechanism (i) to be

$$\Delta f_{||} \approx \frac{4\pi\gamma\alpha k_B T}{M_s V D^2} n^2 \tag{3.1}$$

where D is the length of the precession trajectory on the unit sphere, and n = 1 or 2 for the first or second harmonic peak.[3] If we substitute parameters appropriate for device 1: $\alpha = 0.025$ [32], $T = 150$ K, $\mu_0 M_s = 0.81$ T [53], $n = 2$, dimensions $2 \times 120 \times 60$ nm^3, and $\theta = 32°$, we predict a contribution from this mechanism of $\Delta f \approx 12$ MHz. This is much less than the measured linewidths at $T = 150$ K, and the linear T dependence also differs from the experiment, so we conclude that the contribution from this mechanism is likely negligible from devices 1 and 2 in this geometry. The second mechanism, (ii) thermal fluctuations of the free-layer moment transverse to the trajectory, will produce fluctuations in θ about $\langle\theta\rangle$ (upper inset, Fig. 3.3). If f depends on θ, this will cause an additional spread $\Delta f_\perp$. Different regimes are possible for the resulting linewidths, depending on the magnitude (and linearity) of $df/d\theta$, the width of the distribution in θ, and the correlation time for fluctuations. However, (as discussed below) our simulations

[3]Without H_{th}, the steady-state precession is perfectly periodic, so the Fourier transform yields a delta function in power at the resonant frequency. The linewidth due to H_{th} is derived by assuming an arbitrary trajectory on the unit sphere of perimeter D, writing down the distribution of fluctuations in the precession's phase at each time step (it's a Gaussian, since it is caused by H_{th}), and taking a Fourier transform of the time-evolution to get a distribution in frequencies (also a Gaussian). As you can imagine, if D is very small, thermal kicks will cause large jumps in phase, broadening the resonance. Interestingly, we do not see a strong linear component in the data from device 2.

suggest that our data correspond to a regime in which the linewidth at low temperature is simply proportional to the FWHM $\Delta\theta$ of the distribution of precession angles, weighted by the magnitude of the resistance oscillations associated with each θ:[4]

$$\Delta f_{\perp} = n \left.\frac{df}{d\theta}\right|_{\langle\theta\rangle} \Delta\theta. \tag{3.2}$$

The simulation parameters used are those corresponding to device 1 (listed above), together with an in-plane uniaxial anisotropy $\mu_0 H_k = 20$ mT, an out-of-plane anisotropy $\mu_0 M_{eff} = 0.8$ T [53], $I = 1.2$ mA, and $\mu_0 H = 50$ mT applied along the easy axis, with the fixed-layer moment in the same direction. We assume that the angular dependence of the Slonczewski torque is simply proportional to $\sin(\theta)$ with an efficiency parameter of 0.2 [29].

The squares in Fig. 3.3 show the FWHM calculated directly from the Fourier transform of $R(t)$ obtained in the simulation, and the triangles display values predicted by the right-hand side of Eq. 3.2 with $\Delta\theta$ and $df/d\theta|_{\langle\theta\rangle} \approx 35$ MHz/deg both determined from the same simulation. The agreement between these two quantities demonstrates that the simulation is not in a regime where motional narrowing is important, and that Eq. 3.2 gives a good description of the linewidths expected from dynamics within this approximation.[5]

The T dependence of the calculated linewidths in Fig. 3.3 is to good accuracy $T^{1/2}$ at low T (Fig. 3.3, inset). We expect that this form is very general (and perhaps even applicable beyond the macrospin case) because it follows from Eq. 3.2, if one assumes that Boltzmann statistics can be applied to this non-equilibrium

[4]For small angles, (discussed in chapter 2) the resistance oscillations are proportional to $\theta_{mis}^2\theta^2$ for the fundamental peak and θ^4 for the second harmonic; see the online supporting material in Ref. [32].

[5]The small systematic deviations at higher temperatures are likely due to nonlinearities in the system occurring when the $\Delta\theta$ becomes comparable to $\langle\theta\rangle$.

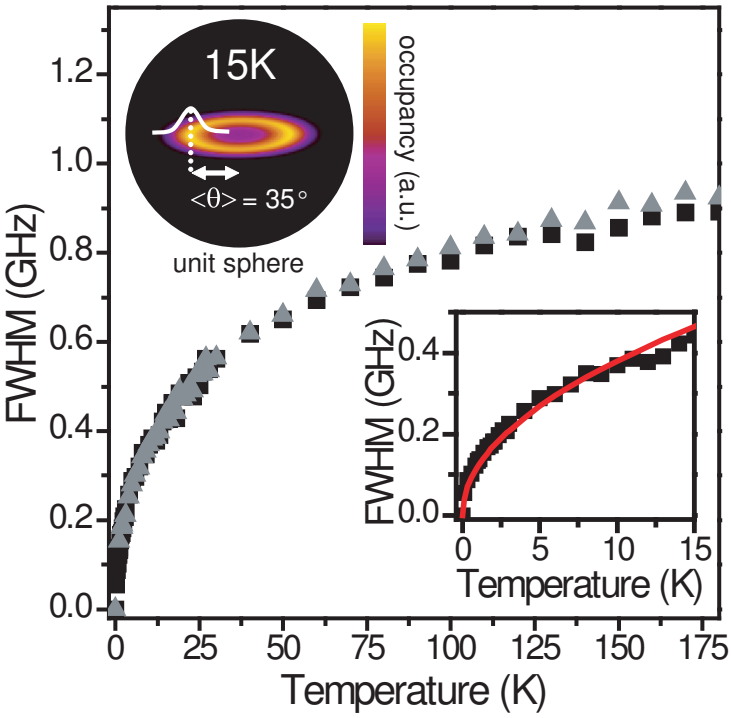


Figure 3.3: (Main plot and lower inset) Squares: Linewidth calculated directly from the Fourier transform of $R(t)$ within a macrospin LLG simulation of the dynamics of device 1. Triangles: Linewidth calculated from the same simulation using the right-hand side of Eq. 3.2. The discrepancy at high temperature hints that motional narrowing is worth pausing to consider, but not over the temperature range reported here. Line in inset: Fit to a $T^{1/2}$ dependence. (Top inset) Simulated probability distribution of the precession angle at 15 K. At higher temperatures, the distribution in θ becomes more complicated than a simple peak and the $T^{1/2}$ behavior begins to break down.

problem. If fluctuations of θ about $\langle\theta\rangle$ are subject to an effective linear restoring term, then both simulations and simple analytical calculations show that $\Delta\theta \approx AT^{1/2}$, where A is a constant.[6]

Consider now the data for device 1 shown in Fig. 3.2a. In the range 25-110 K, Eq. 3.2 with $\Delta\theta \approx AT^{1/2}$ gives a reasonable fit, with one adjustable parameter $Adf/d\theta|_{\langle\theta\rangle} = 2.3$ MHz $\mathrm{K}^{1/2}$. However, the measured widths are approximately a factor of 8 narrower than those predicted by the macrospin simulation with parameters chosen to model this sample (Fig. 3.3). The measured value $df/d\theta|_{\langle\theta\rangle} \sim 30$ MHz/deg is similar to the simulation, so the effective linear restoring term required to model our device ($\propto 1/A^2$) would have to be larger by a factor of ~ 50. We have not been able to account for so large a difference by varying device parameters over a reasonable range or by employing different predictions for the angular dependence of the spin torque [55].

We are therefore led to the surprising suggestion that spin-transfer-driven dynamical modes can generate narrower linewidths at low T than are expected within the macrospin approximation. Initial micromagnetic simulations have been performed in an attempt to account for the possibility of spatially nonuniform magnetizations in spin-transfer devices [26,33,67,68]. However, for the cases analyzed, non-uniformities have thus far led to much broader, not narrower, linewidths. It is possible that the simulations might be improved by including recently proposed mechanisms, whereby different regions of a nanomagnet interact through feedback mediated by the current [8,60,69,70]. At the 2007 APS March Meeting, Kyung-

[6] A is set by the details of the precession and the effective restoring term. If A is small, when a thermal fluctuation kicks θ away from equilibrium, it will take a long time to return. In this case, thermal fluctuations will cause a larger spread in θ and hence a larger linewidth.

Jin Lee reported unpublished simulation results showing that including this effect substantially improves the coherence time of precession in nanomagnets similar to ours [71].

Above $T \approx 120$ K, the measured linewidths (Fig. 3.2) increase with T much more rapidly than the approximate low-temperature $T^{1/2}$ dependence predicted above. The macrospin simulation simply cannot capture this upturn at higher temperatures. As we shall now discuss, a plausible mechanism for the strong T dependence is switching between different dynamical modes, leading to linewidths inversely proportional to the lifetime of the precessional state. Switching between different steady-state precessional modes and static states has previously been identified at frequencies from < 100 kHz [45,53,72] to several gigahertz [52]. The consequences on linewidths have been considered within LLG simulations [29]. Further direct experimental evidence for rapid mode-hopping is reported below. Interestingly enough, without knowing the details of the micromagnetic modes involved, we can estimate the effects of such switching by simply assuming that the average lifetime of a precessional state is thermally activated, $\tau \approx (1/f)exp(E_b/k_BT)$, where E_b is an effective activation barrier. The time-averaged Fourier transform then yields a linewidth[7]

$$\Delta f_{sw} = \frac{1}{\pi\tau} = \frac{f}{\pi} exp(-E_b/k_BT). \tag{3.3}$$

We find that only the combination of Eqs. 3.2 and 3.3 gives a good description of

[7]The linewidth here basically arises from our inability to resolve the frequency; when telegraphing between two dynamical states, the time trace of the resistance oscillations is essentially a series of short sinusoidal blocks of differing lengths t. If one of the modes is short-lived, it will not contribute to the Fourier transform, and what remains are blocks of a single frequency, with uncorrelated phases. The Fourier transform of one of these blocks is a peak (with side-bands) width $\propto 1/t$. Averaging over the distribution of lifetimes (an exponential) yields a Lorentzian with a width given by Eq. 3.3.

the strong T-dependence of the linewidths in Fig. 3.2. For device 1, $Adf/d\theta|_{\langle\theta\rangle} =$ 2.3 MHz K$^{1/2}$ (as before) and $E_b/k_B = 400$ K. For device 2, $Adf/d\theta|_{\langle\theta\rangle} = 3.7$ MHz K$^{1/2}$ and $E_b/k_B = 880$ K.[8] Similar values of E_b were determined from gigahertz-rate telegraph-noise signals by Pufall *et al.* [52]. Note that Eq. 3.3 alone would predict low-T linewidths much smaller than we measure. The effective barriers from the fits are small compared to the static anisotropy barriers (for switching) $\mu_0 M_s H_k V/k_B \sim 10,000$ K in device 1 and 100,000 K in device 2. It is not surprising that the effective barriers for switching between dynamical states are distinct from the static anisotropies.

Direct evidence for the importance of the switching mechanism can be seen in some samples (e.g., device 3, composed of 80 nm Cu / 8 nm IrMn / 4 nm Py / 8 nm Cu / 4 nm Py / 20 nm Cu / 30 nm Pt, with a cross section of 130 $\times$ 60 nm^2) for which, at particular values of I, H, and T, multiple peaks can appear simultaneously in the power spectrum at frequencies that are not related harmonically Fig. 3.4. In these regimes, the widths of both peaks are broader than when only a single mode is visible in the spectrum. We suggest the cause is rapid switching between two different dynamical states.[9]

[8]The common approximation we used in Eq. 3.3, that the activation attempt time is equal to the precession period, is difficult to justify. However, the fit results are fairly insensitive to the attempt time so long as its the right order of magnitude. If we leave the attempt time as a third floating parameter, for device 2 (where $f = 15.9$ GHz) the quality of fit is similar, with attempt time 1/19 GHz and $E_b/k_B = 930$ K. For device 1 ($f = 5.3$ GHz), the attempt time is 1/14 GHz with $E_b/k_B = 550$ K. In both cases, the low-temperature values of $Adf/d\theta|_{\langle\theta\rangle}$ are not affected within the precision of this measurement.

[9]It might be interesting to study this over-barrier process in greater detail by simultaneously monitoring the Lorentzian centered at $f = 0$ that should appear when there is telegraphing between modes. The zero-frequency peak linewidth gives more information about the telegraphing rates and its height gives information about the change in average resistance between the two modes. Spectra containing multiple peaks and broadening tend to show an upturn at low frequency,

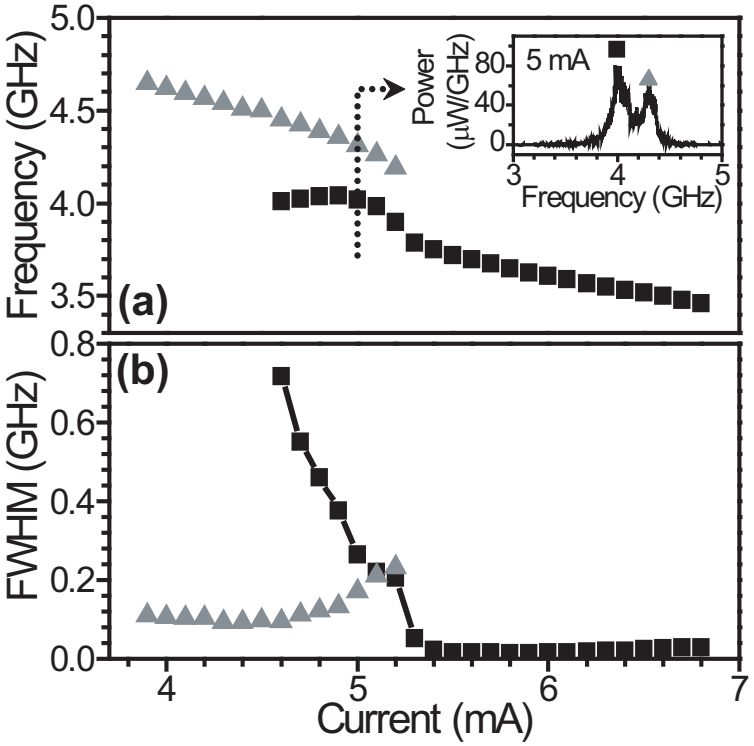


Figure 3.4: Measured (a) frequencies and (b) linewidths of large-angle dynamical modes in device 3 for $T = 40$ K, $\mu_0 H = 63.5$ mT applied in the exchange-bias direction, 45° from the free-layer easy axis. When two modes are observed in the spectrum simultaneously, both linewidths increase.

Macrospin simulations at experimental temperatures do not exhibit switching between metastable states except in narrow regions of the dynamical phase diagram where nearly degenerate modes exist [21, 29]. In contrast, we measure strong thermally activated temperature dependence whenever precessional dynamics are present, for $T > 120$ K. In this regime, transitions involving nonuniform modes [8, 60, 68] therefore appear only to increase the linewidths. Understanding these transitions will provide an important test for future micromagnetic simulations.

The narrowest linewidth that we achieved for any free-layer oscillation (shown in Fig. 3.1a, for a sample composition the same as device 3) in a patterned nanopillar device is[10] 5.2 MHz, corresponding to a coherence time of $1/\Delta f \sim 190$ ns. This is more than a factor of 100 improvement relative to the first measurements in nanopillars of the previous chapter, and is comparable to the lower limit expected from Eq. 3.1.[11] Such narrow linewidths are observed in devices containing an antiferromagnetic layer to exchange bias the fixed magnetic layer 45° relative to the easy axis and with H applied along the exchange-bias direction. We speculate that the reduced symmetry of these conditions may improve the coherence time by reducing both $df/d\theta$ and the likelihood of thermally activated switching between low-energy modes. Also, as discussed in Ilya Krivorotov's upcoming paper [59], when the moments are not collinear (and the spin-torque is not ~ 0), the spatial distribution of the spin-transfer torque across the free layer is not so wildly affected by small changes in the local magnetization. This leads to more spatially uniform and stable rotation of the magnetization.

---

but this has not been studied in detail.

[10] At the time this data was published.

[11] Unfortunately, ohmic heating due to increased critical currents and resistance precludes T dependent studies below $T \approx 200$ K in the samples with these small linewidths.

3.4 Conclusions

In summary, we have studied the spectral linewidth of magnetization dynamics in individual nanomagnets driven by DC spin polarized currents, as a function of temperature and the proximity of nearby modes. Our data indicate that the coherence time of spontaneous spin-transfer-driven magnetic dynamics is limited by thermal effects: thermal fluctuations of the precession angle at low T, and thermally activated mode switching at high T or near bias points where two or more different modes are accessible. Without knowing the exact details of the true micromagnetic modes involved, we have measured the effective energy barriers separating them (roughly 1000 K, which is very small compared to the energy barrier for full reversal). The coherence time can be increased dramatically by cooling samples below room temperature, increasing the magnetic volume, finding regimes where the frequency does not vary with angle, and avoiding the situation where several similar modes are accessible.

Chapter 4

Spin-Transfer-Driven Ferromagnetic Resonance of Individual Nanomagnets

The contents of this chapter are adapted from work originally published as *Phys. Rev. Lett.* **96**, 227601, (2006).

4.1 Introduction

Ferromagnetic resonance (FMR) is the primary technique for learning about the forces that determine the dynamical properties of magnetic materials. However, conventional FMR detection methods lack the sensitivity to measure individual sub-100-nm-scale devices that are of interest for fundamental physics studies and for a broad range of memory and signal-processing applications. For this reason, many new techniques are being investigated for probing magnetic dynamics on small scales, including Brillouin scattering [73] and FMR detected by Kerr microscopy [74], scanning probes [75, 76], X-rays [77], and electrical techniques [78]. Here we demonstrate a simple new form of FMR that uses innovative methods to both drive and detect magnetic precession, thereby enabling FMR studies for the first time on individual sub-100-nm devices and providing a detailed new understanding of their magnetic modes. We excite precession not by applying an AC magnetic field as is done in other forms of FMR, but by using spin-transfer torque from a spin-polarized AC current [2, 3]. We detect the resulting magnetic motions electrically. We demonstrate detailed studies of FMR in single nanomagnets as small as $30 \times 90 \times 5.5$ nm^3, and the method should be scalable to investigate much

smaller samples as well. Our technique is similar to methods developed by Tulapurkar *et al.* [35] for radio-frequency detection, but we will demonstrate that the peak shapes measured there were likely not simple FMR.

We have achieved the following new results: (i) We measure magnetic normal modes of a single nanomagnet, including both the lowest-frequency fundamental mode and higher-order spatially nonuniform modes. (ii) By comparing the FMR spectrum to signals excited by a DC spin-polarized current, we demonstrate that different DC biases can drive different normal modes. (iii) From the resonance line shapes, we distinguish simple FMR from a regime of phase locking. (iv) from the resonance linewidths, we achieve efficient measurement of the magnetic damping in a single nanomagnet.

4.2 Devices and Apparatus

Our samples have a nanopillar structure (Fig. 4.1a, inset), consisting of two magnetic layers – 20 nm of permalloy (Py = $Ni_{81}Fe_{19}$) and 5.5 nm of a $Py_{65}Cu_{35}$ alloy – separated by a 12 nm copper spacer (see details in appendix 4.5.1). We pattern the layers to have approximately elliptical cross sections using ion milling. We focus here on one 30×90 nm^2 device, but we also obtained similar results in 40×120 and 100×200 nm^2 samples.[1] We use different materials for the two magnetic layers so that by applying a perpendicular magnetic field H we can induce an offset angle between their equilibrium moment directions (without an offset angle, both the spin-transfer torque and the small-angle resistance response are zero). The room-temperature magnetoresistance (Fig. 4.1a) shows that the PyCu moment

[1]Generally, in the larger samples, we find the mode spacing is reduced, and it is difficult to find a regime in which to cleanly study a single mode.

saturates out of plane at $\mu_0 H \approx 0.3$ T, while the larger moment of Py does not saturate until approximately $\mu_0 H > 1$ T.[2] All of our FMR measurements in this chapter are performed at low temperature (≤ 10 K),[3] and the direction of H is approximately perpendicular to the layers ($\hat{z}$ direction), tilted 5° along the long axis of the ellipse (in the $\hat{x}$ direction) to stabilize the in-plane component of the Py layer magnetization along $\hat{x}$. Positive currents correspond to electron flow from the PyCu to the Py layer. Using a bias tee, we apply current at both microwave frequencies ($I_f \cos 2\pi f t$) and DC (I_{DC}) while measuring the DC voltage across the sample V_{DC} (Fig. 4.1b). If the frequency f is set near a resonance of either magnetic layer, the layer will precess, producing a time-dependent resistance:[4]

$$R(t) = R_0 + \Delta R(t) = R_0 + Re\left(\sum_{n=0}^{\infty} \Delta R_{nf} e^{in2\pi ft}\right), \tag{4.1}$$

where ΔR_{nf} can be complex. The voltage $V(t) = I(t)R(t)$ will contain a term involving mixing between I_{RF} and $\Delta R(t)$, so that the measured DC voltage will be

$$V_{DC} = I_{DC}(R_0 + \Delta R_0) + \frac{1}{2} I_{RF} |\Delta R_f| cos(\delta_f), \tag{4.2}$$

where δ_f is the phase of ΔR_f. The final term enables measurement of spin-transfer-driven FMR. To reduce background signals and noise, we chop the microwave current bias at 1.5 kHz and measure the DC mixing signal $V_{mix} = V_{DC} - I_{DC} R_0$ using a lock-in amplifier.[5]

[2]The 20 nm Py layer used here has a stronger demagnetizing field than the 3-nm layer of Ref. [5].

[3]At room temperature, this sample is super-paramagnetic, but there is still a small FMR signal. It may be interesting vary the temperature and investigate phase-locking and decoherence in this system.

[4]Resistances are all differential.

[5]Not included in this equation is the term $(1/2)(d^2V/dI^2)I_{RF}^2$ which arises from non-resonant nonlinear mixing in the device. Here we subtract this background from the data when applicable.

4.3 Data and Analysis

In Fig. 4.1c we plot the FMR response V_{mix}/I_{RF} measured for I_{DC} near 0. We observe several resonances, appearing as either peaks or dips in V_{mix}. An applied I_{DC} can decrease the width of some resonances and make them easier to discern as discussed below. By studying the field dependence of the largest resonances (Fig. 4.1d), we identify two groups that we will call normal modes A_0, A_1, and A_2 (solid symbols) and B_0, B_1 (open symbols). Above $\mu_0 H = 0.3$ T, the field required to saturate the PyCu moment along $\hat{z}$, the frequencies of A_0, A_1, and A_2 shift linearly in parallel with slope $df/dH = g\mu_B\mu_0/h$, where $g = 2.2 \pm 0.1$. As expected for the modes of a thin-film nanomagnet [50], the measured frequencies are shifted above that of uniform precession of a bulk film, $f_{film} = (g\mu_B/h)(\mu_0 H - \mu_0 M_{eff})$, with $\mu_0 M_{eff} = 0.3$ T.[6] The linearity of the frequency with respect to H above 0.3 T provides initial evidence that A_0, A_1, and A_2 are magnetic modes of the PyCu layer (additional evidence is presented later). The other two large resonances, B_0 and B_1, also shift together, with weaker dependence of H. This is the behavior expected for modes of the Py layer, because the values of H shown in Fig. 4.1d are not large enough to saturate the Py layer out of plane. To avoid coupling between modes in different layers, we perform our detailed measurements at fields where the mode frequencies are well separated. In addition to these modes, we observe small signals (not shown in Fig. 4.1d) at twice the frequencies of the main modes

[6] Generally, the more nonuniform the mode, the higher the frequency due to the exchange field. We might draw the conclusion that mode A_0 is quite nonuniform based entirely on its frequency shift above macrospin estimations. However, there is also substantial dipolar coupling from the Py on the PyCu layer, which tends to offset the frequency as well. I am quite interested to see what micromagnetic simulations predict in this geometry.

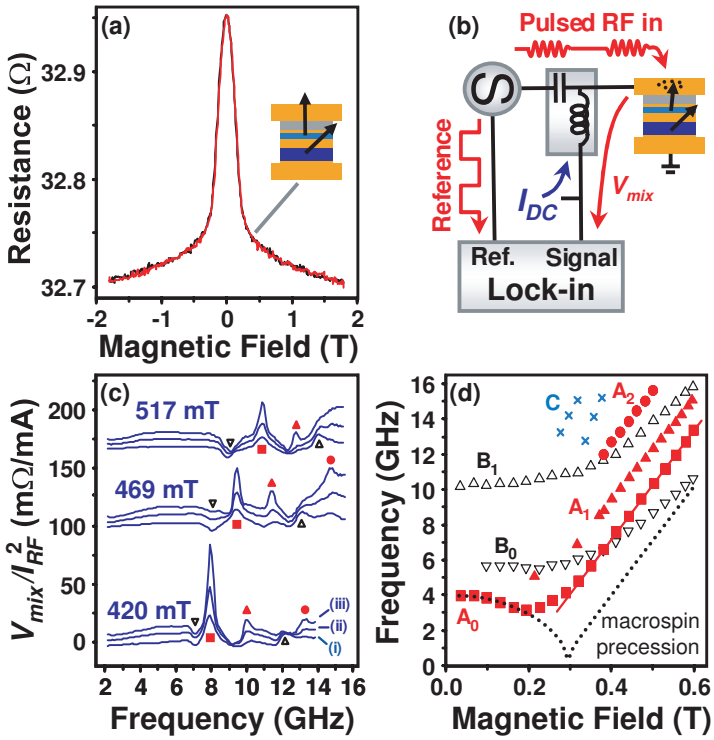


Figure 4.1: (a) Room-temperature magnetoresistance as a function of field perpendicular to the sample plane. (inset) Cross-sectional sample schematic, with arrows denoting a typical equilibrium moment configuration in a perpendicular field. (b) Schematic of circuit used for FMR measurements. (c) FMR spectra measured at several values of magnetic field, at I_{DC} values (i) 0, (ii) 150 μA, and (iii) 300 μA, offset vertically. Symbols identify the magnetic modes plotted in (d). Here I_{RF} = 300 μA at 5 GHz and decreases by $\sim$ 50% as f increases to 15 GHz (refer to appendix 4.5.1). (d) Field dependence of the modes in the FMR spectra. The solid line is a linear fit, and the dotted line would be the frequency of completely uniform precession.

and near frequency sums (modes C).[7]

Based on comparisons to simulations [33,50] and that the lowest-frequency resonances produce the largest resistance signals, we propose that A_0 and B_0 correspond to the lowest-frequency normal mode of the PyCu and Py layer respectively. This mode should have the most spatially uniform precession amplitude (albeit not exactly uniform) [33, 50]. The higher-frequency resonances A_1, A_2, and B_1 must correspond to higher-order nonuniform modes. The observed frequencies and frequency intervals are in the range predicted for normal modes of similarly shaped nanoscale samples [33, 50].

Next we compare the FMR measurements to spontaneous precessional signals that can be excited by I_{DC} alone ($I_{RF} = 0$) [61,62]. The power spectral density of resistance oscillations for DC-driven excitations at 420 mT is shown in Fig. 4.2a. We examine $I_{DC} > 0$, which gives the sign of torque to drive excitations in the PyCu layer only [5]. A single peak appears in the DC-driven spectral density above a critical current $I_c = 0.3$ mA, and moves to higher frequency with increasing I_{DC}. The increase in frequency can be identified with an increasing precession angle, which decreases the average demagnetizing field along $\hat{z}$ [5]. At larger I_{DC}, we observe additional peaks at higher f and switching of the precession frequency between different values, similar to the results of previous measurements [5,61,62] that have not been well explained before.

The FMR signals are displayed in Fig. 4.2b at the same values of I_{DC} shown in Fig. 4.2a. we find that the FMR fundamental mode A_0 that we identified

[7]These extra features are neither sharp nor well-defined peaks, and it is quite difficult to accurately define their central frequency. I suspect that these modes would be much easier to identify if we performed this experiment using the improved RF leveling techniques discussed in the next chapter.

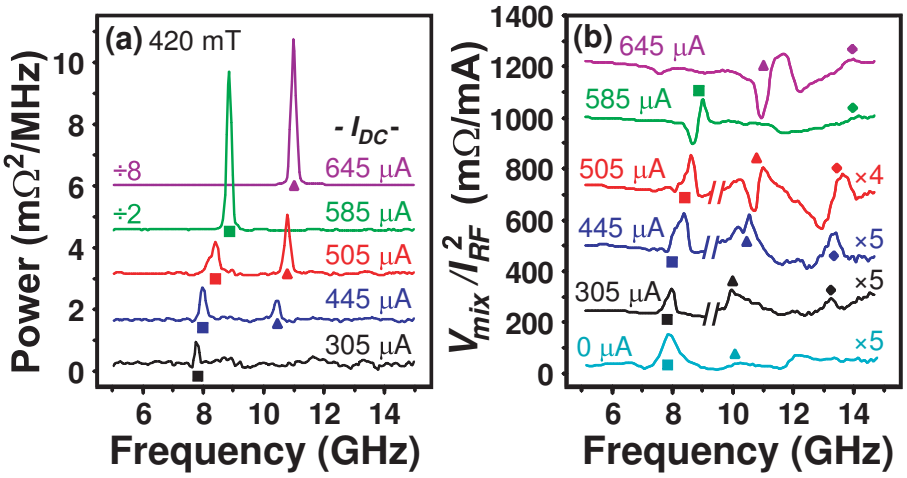


Figure 4.2: Comparison of FMR spectra to DC-driven precessional modes. (a) Spectral density of DC-driven resistance oscillations for different values of I_{DC} (labeled), with $\mu_0 H = 370$ mT and $I_{RF} = 0$. (b) FMR spectra at the same values of I_{DC}, measured with $I_{RF} = 270$ μA at 10 GHz. The high-f portions of the 305, 445, and 505 μA traces are amplified to better show small resonances. The $I_{DC} = 0$ curve is the same as in Fig. 4.1c.

above with the PyCu layer is the mode that is excited at the threshold for DC-driven excitations. When I_{DC} is large enough that the DC-driven mode begins to increase in frequency (585 μA), the shape of this FMR changes from a simple Lorentzian to a more complicated structure with a dip at low frequency and a peak at high frequency. The FMR peaks A_1 and A_2 also vary strongly in peak shape and frequency as a function of positive I_{DC}, in a manner similar to A_0, confirming that A_1 and A_2 (like A_0) are associated with the PyCu layer. The FMR modes B_0 and B_1 that we identified with the Py layer do not shift significantly in f as a function of positive I_{DC}. This is expected, because positive I_{DC} is the wrong sign to excite spin-transfer dynamics in the Py layer [2].

There has been significant debate about whether the magnetic modes which contribute to the DC-spin-transfer-driven precessional signals correspond to approximately uniform macrospin precession or to nonuniform spin-wave instabilities [8,60,69,79]. Our FMR measurements show directly that, at I_c, the DC-driven peak frequency is equal to that of the lowest-frequency RF-driven mode, the one expected to be the most spatially uniform [50]. Higher values of I_{DC} can also excite the spatially nonuniform mode A_1 and even produce mode hopping so that mode $A1$ can be excited when mode A_0 is not.

In order to analyze the FMR peak shapes, we make the simplifying assumption that the lowest-frequency modes A_0 and B_0 can be approximated by a macrospin model, with the Slonczewski form of the spin-transfer torque [2]. The PyCu layer magnetization $\mathbf{m}$ then evolves according to the Landau-Lifshitz-Gilbert-Slonczewski (LLGS) equation:

$$\frac{\partial \mathbf{m}}{\partial t} = \gamma_0 \mu_0 (\vec{H} + \vec{H}_{anis}) \times \mathbf{m} + \alpha \mathbf{m} \times \frac{\partial \mathbf{m}}{\partial t} + \frac{\eta I(t)}{e} \mathbf{m} \times (\mathbf{m} \times \mathbf{M}). \qquad (4.3)$$

Here, γ_0 is the magnitude of the gyromagnetic ratio, $\vec{H}$ and $\vec{H}_{anis}$ are the applied

and anisotropy fields, α is the Gilbert damping parameter, and η (> 0 for our definition of positive current) is a dimensionless spin transfer efficiency factor [2]. A similar equation of motion for the Py layer can be quickly attained by swapping $\mathbf{m}$ and $\mathbf{M}$, and using the appropriate η (< 0). Equations 4.3 and 4.2 together predict a Lorentzian line shape

$$V_{mix}(f) = \frac{\partial R}{\partial \theta} \frac{I_{RF}^2 \eta \sin(\theta)}{8\pi e \Delta_0} \frac{1}{1 + (f - f_0)^2/\Delta_0^2}. \tag{4.4}$$

Here R is the differential resistance, θ is the angle between $\mathbf{m}$ and $\mathbf{M}$, f_0 is the unforced precession frequency, and Δ_0 is the linewidth. For the Py layer (when $\eta < 0$) this equation predicts an inverted Lorentzian signal, similar to that of mode B_0. The width Δ_0 predicted for the PyCu layer in our simple experimental geometry is (to within 1% error for $\mu_0 H > 0.5$ T; see appendix 4.5.2)

$$\Delta_0 = \alpha f_0. \tag{4.5}$$

As predicted by Eq. 4.4, we find that the measured FMR peak for mode A_0 at $I_{DC} = 0$, for sufficiently small values of I_{RF}, is fit accurately by a Lorentzian, the amplitude scales $V_{mix} \propto I_{RF}^2$, and the width is independent of I_{RF}, (Figs. 4.3a and 4.4a). Our minimum measurable precession angle is $\approx 0.2°$. For $I_{RF} >$ 0.35 mA, the peak eventually shifts to higher frequency and the shape becomes asymmetric, familiar properties for nonlinear oscillators [80]. From the magnitude of the frequency shift in similar signals (Fig. 4.3b, inset), we estimate that the largest precession angle we have achieved is approximately 40°.

The peak shape for mode B_0 is also to good accuracy Lorentzian for small I_{DC}, but with negative sign. This sign is expected because when the Py moment precesses in resonance, the positive current pushes the Py moment angle closer to the PyCu moment, giving a negative resistance response. The FMR peak shapes

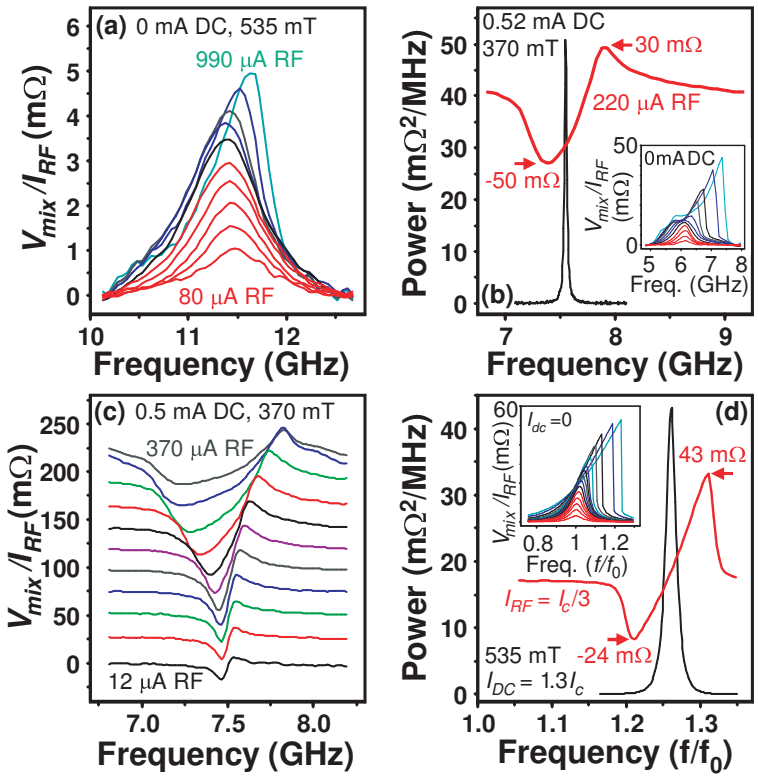


Figure 4.3: (a) FMR peak shape for mode A_0 at $I_{DC} = 0$ and different values of I_{RF}: from bottom to top, traces 1-5 span I_{RF} = 80-340 μA in equal increments, and traces 5-10 span 340-990 μA in equal increments. (b) Bottom curve: spectral density of DC-driven resistance oscillations for mode A_0, showing a peak with half width at half maximum = 13 MHz. Top curve: FMR signal at the same bias conditions, showing the phase-locking peak shape. (inset) Evolution of the FMR peak for mode A_0 at 370 mT, $I_{DC} = 0$, for I_{RF} from 30 μA to 1160 μA. (c) Evolution of the FMR signal for mode A_0 in the phase-locking regime at $I_{DC} = 0.5$ mA, $\mu_0 H = 370$ mT, for (bottom to top) I_{RF} from 12 to 370 μA, equally spaced on a logarithmic scale. (d) Results of macrospin simulations for the DC-driven dynamics and FMR signal 4.5.

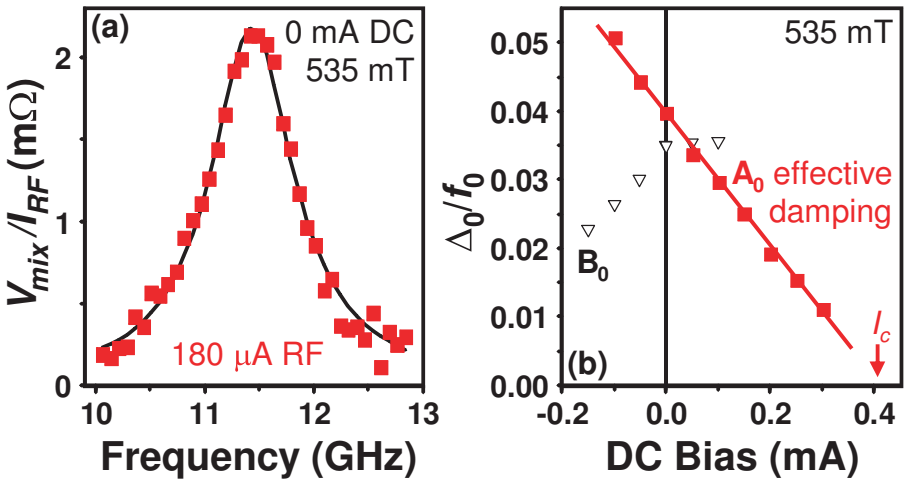


Figure 4.4: (a) Detail of the peak shape for mode A_0, at $I_{DC} = 0$, $I_{RF} = 180$ μA, $\mu_0 H = 535$ mT, with a fit to a Lorentzian line shape. (b) Dependence of linewidth on I_{DC} for modes A_0 and B_0, for $\mu_0 H = 535$ mT. For the PyCu layer mode A_0, Δ_0/f_0 is equal to the magnetic damping α. The critical current is $I_c = 0.40 \pm 0.03$ mA at $\mu_0 H = 535$ mT, as measured independently by the onset of DC-driven resistance oscillations.

for the higher-order modes A_1, A_2, and B_1 are not as well fit by Lorentzians. We plot the spectrum of DC-driven excitations for $I_{DC} = 0.52$ mA, $I_{RF} = 0$ in Fig 4.3b. The width is much narrower than the FMR spectrum for the same mode (inset), confirming arguments that the linewidths in these two types of measurements are determined by different physics (see chapter 3).

We noted above that the FMR peak shape changes from a Lorentzian to a more complex shape for sufficiently large values of I_{DC} (see the detailed resonance shapes in Figs. 4.3b and 4.3c). As shown in Fig. 4.3d, this shape change is reproduced by a macrospin simulation (discussed in appendix 4.5.3), and can be explained as a consequence of phase locking between I_{RF} and the large-amplitude

precession excited by I_{DC} [18, 36, 81, 82]. Due to the demagnetization field in our geometry, the precession frequency increases with precession amplitude. As a result, (confirmed by the simulation) applying RF current on the low-f side of a large-angle DC-driven resonance forces the amplitude to decrease. Under these conditions, the precession phase locks approximately out of phase with the applied RF current ($\delta_f \approx 180°$), giving negative values of V_{mix}. Frequencies on the high-f side force the precession to larger amplitude, producing phase locking approximately in phase with the drive and a positive V_{mix}. Recently, Tulapurkar *et al.* [35] measured similar peak shapes, and proposed that they were caused by simple FMR with a torque mechanism different from the Slonczewski theory. We suggest instead that the peak shapes in [35] may be due either to phase locking with thermally excited precession at room temperature (rather than simple FMR), or to the superposition of two FMR signals from different layers (one positive like that of A_0 and one negative like B_0).

A benefit of measuring the Lorentzian line shape of simple FMR is that the linewidth allows a measurement of the magnetic damping parameter α, using Eq. 4.5. It is highly desirable to minimize the damping in spin-transfer-driven memory devices so as to decrease the current needed for switching [2]. Previously, α in magnetic nanostructures could only be estimated by indirect means [30, 32]. As shown in Fig. 4.4b, for $I_{DC} = 0$ we measure $\alpha = 0.040 \pm 0.001$ for the Py Cu layer. This is larger than the damping for $Py_{65}Cu_{35}$ films in identically prepared large-area multilayers as measured by conventional FMR, $\alpha_{film} = 0.021 \pm 0.003$. The cause of the extra damping in our nanopillars is not known, but it may be due to coupling with the antiferromagnetic oxide along the sides of the device [83]. As a function of increasing I_{DC}, the theory of spin-transfer torques predicts that

the effective damping should decrease linearly, reaching zero at the threshold for the excitation of DC-driven precession [2]. This is precisely what we find for mode A_0 (Fig. 4.4b). In contrast, the linewidth of mode B_0 decreases with decreasing I_{DC}. This is as expected for a Py-layer mode, because the sign of the spin-transfer torque should promote DC-driven precession in the Py layer at negative I_{DC}.

4.4 Conclusions

In this chapter we have demonstrated a new form of ferromagnetic resonance driven by spin transfer (ST-FMR) that is capable of probing individual nanomagnets orders of magnitude smaller than can be achieved through existing methods [73–78]. In contrast to the techniques discussed in chapters 2 and 3, here we apply a microwave-frequency current and measure the magnetic response through a DC mixing voltage generated by the magnetoresistance oscillations. We have shown that this technique provides detailed new information about the dynamics of both the fundamental and higher-order magnetic normal modes in single sub-100-nm-scale magnetic samples, in both linear and nonlinear regimes. We probed more of the normal modes than the DC-driven experiments, have identified which modes are excited by DC-currents, and have observed phase locking between the RF current and the large-angle DC-driven modes. Using the resonance linewidth, we have also achieved a direct and efficient measurement of the magnetic damping in a single nanostructure. We confirmed that the effective damping parameter is tunable by I_{DC}, and decreases linearly toward zero at I_c, as predicted [2]. Spin-transfer-driven FMR will be of immediate utility in understanding and optimizing magnetic dynamics in nanostructures used for memory and microwave signal processing applications. Furthermore, both spin-transfer torques and magnetoresis-

tance measurements become increasingly effective on smaller size scales. The same technique may therefore enable new fundamental studies of even smaller magnetic samples, approaching the molecular limit.

4.5 Appendices

4.5.1 Device Details and Circuit Calibration

The thicknesses of the layers composing our samples are, from bottom to top, 120 nm Cu / 20 nm Py / 12 nm Cu / 5.5 nm $Py_{65}Cu_{35}$ / 2 nm Cu, with a Au top contact. The difference in resistance between parallel and antiparallel magnetic layers for our 30×90 nm^2 sample at 10 K is $\Delta R_{max} = 0.84\ \Omega$.

The RF attenuation in our cables, the bias tee, and the ribbon bonds connecting to the sample is frequency dependent. In order to know the value of I_{RF} at the sample, this attenuation must be calibrated. We calibrate the attenuation of the cables and bias tee by measuring their transmission with a network analyzer. To estimate the losses due to the ribbon bonds, we measure the reflection from ribbon-bonded open, short, and 50-Ω test samples. We observe negligible reflection from the bonded 50 Ω sample, implying that the ribbon bonds produce little impedance discontinuity for frequencies < 15 GHz. We can therefore estimate the frequency-dependent transmission through the ribbon bonds as the square root of the measured reflection coefficient from either the bonded open test sample or the bonded short (a square root because the reflected power travels twice through the ribbon bonds). Finally, we measure the reflection coefficient directly for each of our ribbon-bonded samples before collecting FMR data, and from this determine its impedance and the resulting value of I_{RF}. For the 30×90 nm^2 sample on which we focus in the paper, the frequency dependence of I_{RF} at the sample, referenced to the value at 5 GHz, is shown in Fig. 4.5.

The mixing signal contains a background due to deviations from linearity in the I-V curve of the sample, which we subtract from the data presented in the

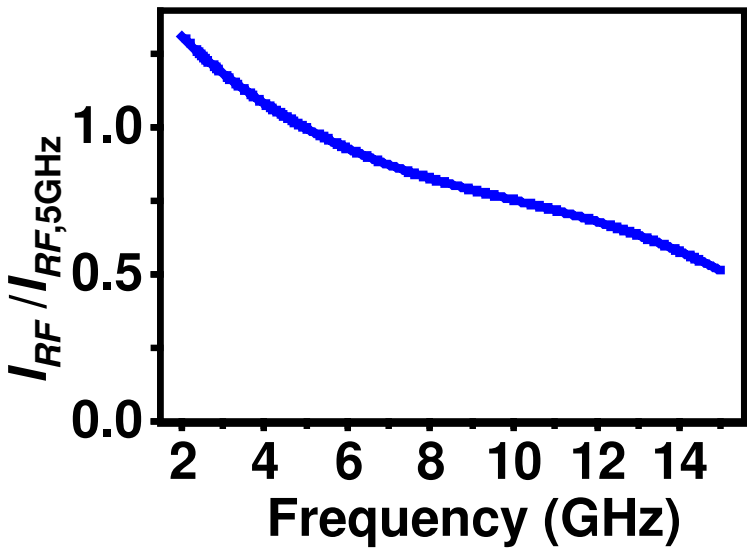


Figure 4.5: Estimated RF current coupled into our device as a function of frequency, relative to the value at 5 GHz.

figures of chapter 4. (At the time this measurement was performed, we had not developed the local mixing calibration techniques of chapter 5.)

4.5.2 Relationship Between Linewidth and Damping

Equation 4.5 of the main text above is an approximation of the true width predicted by Eqs. 4.3 and 4.2:

$$\frac{\Delta_0}{f_0} = \alpha \frac{H/M_s - N_z + N_x/2 + N_y/2}{\sqrt{(H/M_s - N_z + N_x)(H/M_s - N_z + N_y)}} \tag{4.6}$$

We estimate that the effective demagnetization factors for our PyCu layer are N_z = 0.79, N_x = 0.03, and N_y = 0.18, based on a magnetization of 0.39 T [84] and coercive field measurements. However, the result of Eq. 4.6 is quite insensitive to these values, so that for $\mu_0 H > 0.5$ T we have simply $\Delta_0/f_0 = \alpha$ for the PyCu layer to within 1% error. Simulations show that this prediction is also not altered at the 1% level by the 5° offset between $\vec{H}$ and $\hat{z}$ in our measurements.

For the Py layer mode, there is an additional correction required to relate Δ_0/f_0 to α, due to the larger deviation of the precession axis from $\hat{z}$.

4.5.3 Simulation Parameters

In our numerical simulations, we integrate the LLG equation for macrospin precession (Eq. 4.3), using the following parameters: $\alpha = 0.04$, g = 2.2, a PyCu magnetization $\mu_0 M_s = 390$ mT [84], in- and out-of-plane anisotropies 58 mT and 300 mT, and an efficiency parameter $\eta = (0.2)g\mu_B/(2M_sV)$, where μ_B is the Bohr Magneton and V is the volume of a 5.5-nm-thick disk of elliptical cross section 90×30 nm^2. Thermal effects are modeled with a 10 K Langevin fluctuating field [66]. For Fig. 4.3d, $I_c = 0.6$ mA, $f_0 = 8.1$ GHz, and $I_{RF} = 0.1$-1, 1.2, 1.5, 2, 3, and 4 mA. The qualitative results of the simulation are not affected by reasonable variations in device parameters.

4.5.4 Regarding Another Proposed Mechanism for DC Voltages Produced by Magnetic Precession

Berger has proposed that a precessing magnet in a multilayer device may generate a DC voltage directly [85]. This mechanism, derived by calculating the rate of spin flip of conduction-electron spins during precession and solving the spin-diffusion equation in the various layers, could produce another source of signal in our experiments on resonance, in addition to the mixing mechanism we discussed in the main text. However, the maximum magnitude of V_{DC} predicted to be generated by the Berger mechanism is $hf/e = 40$ μeV for $f = 10$ GHz, and our FMR signals can grow much larger than this. Also, we find that at small values of I_{RF} our signals scale as $V_{DC} \propto I_{RF}^2$ as expected for the mixing mechanism (because $|\Delta R_f \propto I_{RF}$),

while the Berger signal would scale $\propto I_{RF}$. On this basis, we argue that only the resistance mixing mechanism is dominant in producing our signal.

Chapter 5

Direct Measurement of the Spin Transfer Torque and its Bias Dependence in Magnetic Tunnel Junctions

The contents of this chapter are adapted from very recent work that we are in the process of publishing.

5.1 Introduction

Nanoscale magnetic tunnel junctions (MTJ, composed of two ferromagnets separated by a tunnel barrier) with MgO barriers can have extremely large magnetoresistance, and for this reason they are under aggressive pursuit for applications in memory technologies and magnetic-field sensing [86–89]. Further, it has recently been demonstrated that the magnetic state of a nanoscale MTJ can be switched by a spin-polarized tunnel current via the spin-transfer torque [90,91], a promising new mechanism for the write operation of nanomagnetic memory elements [92].

While the presence of the spin torque has been unambiguously observed, its quantitative behavior in an MTJ, especially its bias dependence, has yet to be understood in detail. One puzzling observation has been that in contrast to tunnel magnetoresistance (which decreases strongly under bias), the spin torque depends very little on the junction bias [93]. Recent theoretical models attempt to quantify the spin torque's bias dependence in an MTJ, and to explain its relationship with the tunnel magnetoresistance [37,94–96]. To test these model calculations, a direct,

quantitative measurement of how the spin-torque evolves with junction bias is highly desirable. Quantitative understanding of this bias dependence will also be important for the development and optimization of nanostructured MTJ spin-torque devices in memory applications.

Here we demonstrate for the first time that the recently-developed spin-transfer-driven ferromagnetic resonance (ST-FMR) technique [35, 97] described in the previous chapter can be used to achieve a detailed, highly-quantitative understanding of the spin transfer torque in individual nanoscale devices. We apply ST-FMR to MgO-based tunnel junctions similar to those of Tulapurkar *et al.* [35], and directly measure both the magnitude and direction of the spin transfer torque acting upon an individual nanomagnet. We find the torque $\vec{\tau}$ generated by a bias voltage V lies in the plane defined by the magnetizations (in the $\mathbf{m} \times (\mathbf{m} \times \mathbf{M})$ direction with $\mathbf{m}$ and $\mathbf{M}$ defined as the free- and fixed-layer magnetization directions) at small V. The magnitude of the "torkance" [98] for this component, $d\tau_{||}/dV$, is in excellent agreement with the prediction for highly-spin-polarized elastic tunneling. We also measure the evolution of $\vec{\tau}$ under bias. For $|V| < 300$ mV, $d\tau_{||}/dV$ varies by only $\pm 8\%$, and its impact on the free layer magnetization increases at higher voltage, despite the fact that the magnetoresistance decreases by 72% over the same range. We also find that $\vec{\tau}$ rotates under bias; we observe a component perpendicular to the plane (in the $\mathbf{m} \times \mathbf{M}$ direction), $\tau_{\perp}(V)$, that is proportional to the square of bias, becoming as large as 30% of the in-plane component $\tau_{||}(V)$. A torque in this direction is predicted to help the magnetic reversal process by significantly decreasing the switching time and power consumption [99, 100]. Our findings of the rotation and strength of the torque under bias has important implications for memory applications, improving the feasibility of ST-MRAM. Our results can be

interpreted within a simple model.

5.2 Devices and Apparatus

We have studied 8 exchange-biased tunnel junctions (of resistance-area product $\approx 12\ \Omega\ \mu\text{m}^2$ for the parallel magnetic configuration $\mathbf{m} = \mathbf{M}$) with the layers (in nm) 5 Ta / 20 Cu / 3 Ta / 20 Cu / 15 PtMn / 2.5 $Co_{70}Fe_{30}$ / 0.85 Ru / 3 $Co_{60}Fe_{20}B_{20}$ / 1.25 MgO / 2.5 $Co_{60}Fe_{20}B_{20}$ / 5 Ta / 7 Ru deposited on an oxidized silicon wafer by the process described in Ref. [101] (See Fig. 5.1a). The top ("free") magnetic layer is etched to a rounded rectangular cross section with the long axis parallel to the exchange bias from the PtMn layer (the $\hat{y}$ direction), and of size either $50 \times 100\ \text{nm}^2$ or $50 \times 150\ \text{nm}^2$. The etch is stopped at the MgO barrier, so that the bottom ("fixed") layer is left extended on the scale of 10's of microns, and top contacts are made with 5 nm Ti / 150 nm Cu / 10 nm Pt. Contact pads are originally fabricated in a 4-point configuration, but we cut the top electrode close to the sample (Fig. 5.1b, left inset) prior to ST-FMR measurements to eliminate artifacts associated with RF current flow within this electrode rather than through the tunnel junction (see appendix 5.4.1, for more details).

All data in this chapter are from one $50 \times 100\ \text{nm}^2$ device; the other samples gave similar behavior. The bias dependence of the differential resistance dV/dI is shown in Fig. 5.1b for the parallel magnetization orientation (P, $\theta = 0°$, with θ the angle between $\mathbf{m}$ and $\mathbf{M}$, determined as discussed below), antiparallel (AP, $\theta = 180°$), and intermediate angles. At zero bias, the tunneling magnetoresistance ratio (TMR) is $[dV/dI(\text{AP}) - dV/dI(\text{P})]/[dV/dI(\text{P})] = 154\%$. The TMR decreases to 43% at 540 mV bias, a fractional reduction of 72%.

The ST-FMR measurements [35, 97] are performed at room temperature, us-

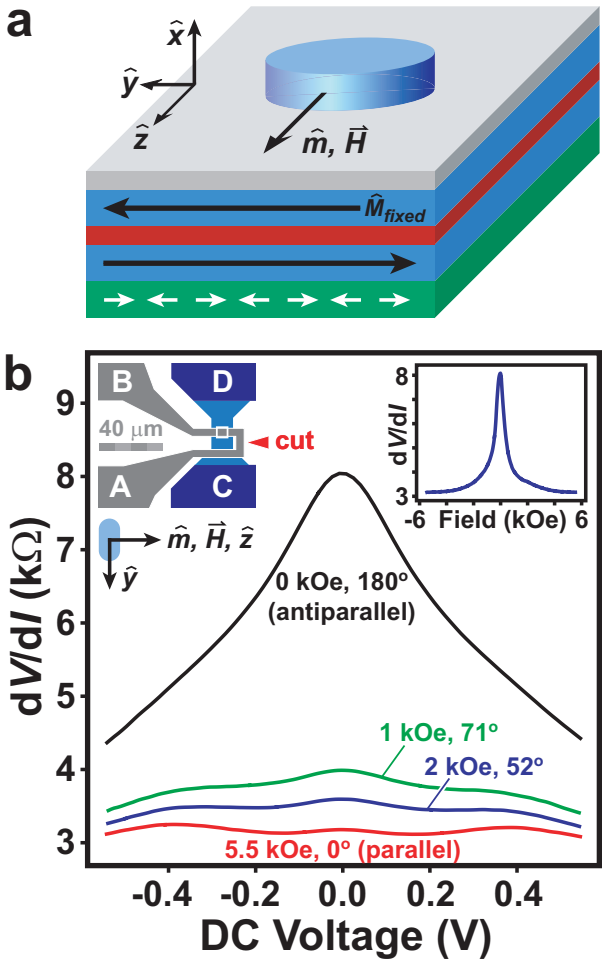


Figure 5.1: Magnetic tunnel junction geometry and magnetic characterization. (a) Schematic of the sample geometry. (b) Bias dependence of differential resistance at room temperature for the parallel orientation of the magnetic electrodes ($\theta = 0°$) and antiparallel orientation ($\theta = 180°$), along with intermediate angles. The angles are determined assuming that the zero-bias conductance varies as $\cos(\theta)$. (Left inset) Layout of the electrical contacts (cropped), showing where the top electrode is cut to eliminate measurement artifacts. (Right inset) Zero-bias magnetoresistance for H along $\hat{z}$.

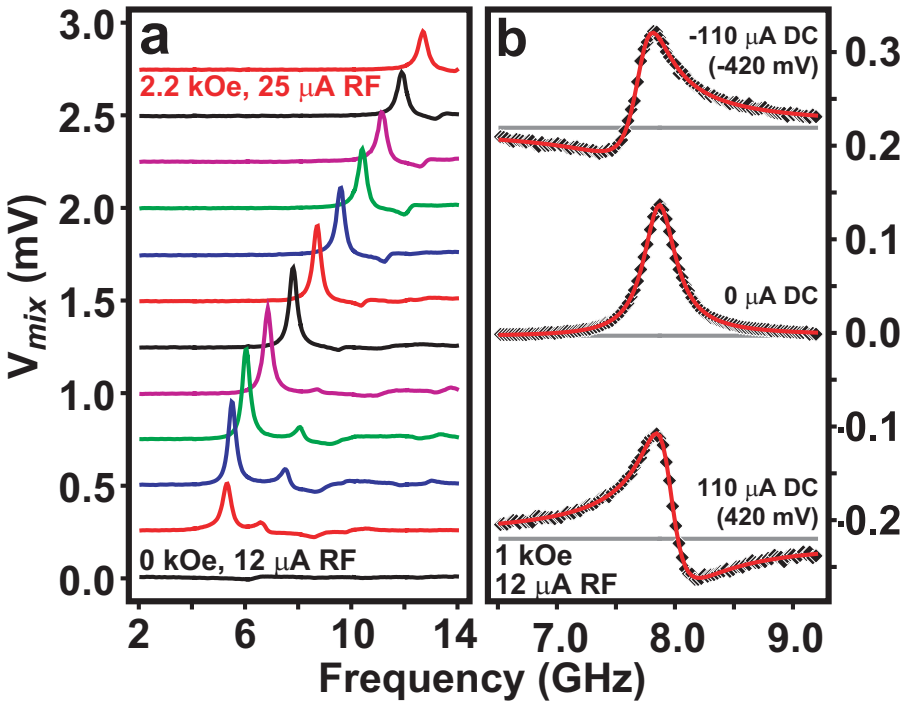


Figure 5.2: ST-FMR spectra at room temperature. (a) Spin-transfer FMR spectra for $I = 0$, for magnetic fields (along $\hat{z}$) spaced by 0.2 kOe. I_{RF} ranges from 12 μA at low field (high resistance) to 25 μA at high field. The curves are offset by 250 μV. (b) Details of the primary ST-FMR peaks at $H = 1000$ Oe and $I_{RF} \approx 12\mu$A for different DC biases. Symbols are data, lines are Lorentzian fits. These curves are not artificially offset; the frequency-independent backgrounds for nonzero DC biases correspond to the first term on the right of Eq. 5.2. A DC bias changes the degree of asymmetry in the peak shape vs. frequency.

ing the procedure described in the previous chapter. A direct current I and a microwave-frequency current I_{RF} are applied simultaneously to the sample at room temperature via a bias-tee. When spin-transfer from I_{RF} excites resonant magnetic dynamics, the resulting resistance oscillations mix with I_{RF} to produce a DC voltage response $\langle V_{mix} \rangle$. To maximize the signal-to-noise of the measurement, we chop I_{RF} at 250 Hz and measure $\langle V_{mix} \rangle$ using a lock-in amplifier. In all cases, we use values of I_{RF} in the range 5-25 μA, small enough that the FMR response is in the linear regime. Our new improved procedures for calibrating I_{RF} and preventing variations in I_{RF} while sweeping frequency are discussed in appendix 5.4.3. We use the convention that positive bias corresponds to electron flow down the pillar, giving a sign of the spin torque that favors AP alignment of $\mathbf{m}$ and $\mathbf{M}$. We apply a sufficiently-strong magnetic field H along the $\hat{z}$ direction (Fig. 5.1b inset) to saturate $\mathbf{m}$, while $\mathbf{M}$ is tilted to a lesser degree away from $\hat{y}$. Representative results for the ST-FMR spectra are shown in Fig. 5.2. We observe several magnetic resonances in the frequency range 2 to 14 GHz. The lowest-frequency resonance has the largest amplitude, and corresponds to the sign of signal expected for excitation of the free magnetic layer (see chapter 4). We assume that other smaller resonances correspond to higher-frequency standing-wave modes of the free or fixed layer, or perhaps coupled modes [97].

Our first major result is that the degree of asymmetry in the ST-FMR peak shape vs. frequency for the lowest-frequency mode depends strongly on the DC bias current I, with peak shapes for $I = 0$ being symmetric, and with the sign of the asymmetry depending on the sign of I (Fig. 5.2b). To analyze quantitatively the magnitudes and the peak shapes of the ST-FMR signals, we assume that the dynamics of the free magnetic layer near the main resonance peak can be

described by a simple macrospin approximation, so that a generalized Landau-Lifshitz-Gilbert (LLG) equation applies:[1]

$$\frac{\partial \mathbf{m}}{\partial t} = -\gamma_0 \mathbf{m} \times \mathbf{H_{eff}} + \alpha \mathbf{m} \times \frac{\partial \mathbf{m}}{\partial t} - \gamma_0 \frac{\tau_{||}(I,\theta)}{M_s Vol} \hat{y} - \gamma_0 \frac{\tau_{\perp}(I,\theta)}{M_s Vol} \hat{x} \qquad (5.1)$$

Here γ_0 is the magnitude of the gyromagnetic ratio, α is the Gilbert damping parameter, $\mathbf{H_{eff}}$ is an effective field as defined in Ref. [102], and $M_s Vol \approx (1.06 \pm 0.16) \times 10^{-14}$ emu is the total magnetic moment of the free layer based on our estimate of the sample geometry and the measured value of $M_s = 1100$ emu/cm^3, consistent with Ref. [101]. The resulting ST-FMR lineshapes have been evaluated [35,97,102,103] and good agreement has been observed in ST-FMR measurements on all-metal spin-valve devices (see chapter 4). By extending the analysis of Ref. [102] to nonzero values of I (see appendix 5.4.2), this formalism predicts that the ST-FMR signal is to a good approximation

$$\langle V_{mix} \rangle = \frac{1}{4} \frac{\partial^2 V}{\partial I^2} I_{RF}^2 + \frac{1}{2} \frac{\partial^2 V}{\partial \theta \partial I} \frac{\hbar \gamma_0 \sin\theta}{4 e M_s Vol \sigma} I_{RF}^2 \left(\zeta_{||} S(\omega) - \zeta_{\perp} \Omega_{\perp} A(\omega) \right). \qquad (5.2)$$

Here $\zeta_{||} = [(2e/\hbar)/\sin(\theta)] d\tau_{||}/dI$ and $\zeta_{\perp} = [(2e/\hbar)/\sin(\theta)] d\tau_{\perp}/dI$ represent the differential torques in dimensionless units, $S(\omega) = 1/[1 + (\omega - \omega_m)^2/\sigma^2)]$ and $A(\omega) = [(\omega - \omega_m)/\sigma] S(\omega)$ are symmetric and antisymmetric Lorentzians, σ is the linewidth, ω_m is the resonant precession frequency, and $\Omega_{\perp} = \gamma_0 (4\pi M_{eff} + H)/\omega_m)$ for our geometry. We use $4\pi M_{eff} = 11 \pm 1$ kOe for the effective out-of-plane anisotropy, as determined from the magnetoresistance for H perpendicular to the substrate. The first term on the right in Eq. 5.2 is a non-resonant background, useful for calibrating I_{RF}. The second term gives the dominant ST-FMR signal; as a function of frequency it has the form of a symmetric Lorentzian $\propto \zeta_{||} \propto d\tau_{||}/dI$, minus an antisymmetric Lorentzian $\propto \zeta_{\perp} \propto d\tau_{\perp}/dI$.

[1] As described in chapter 4, the lowest-frequency mode behaves very much as a uniform magnetization.

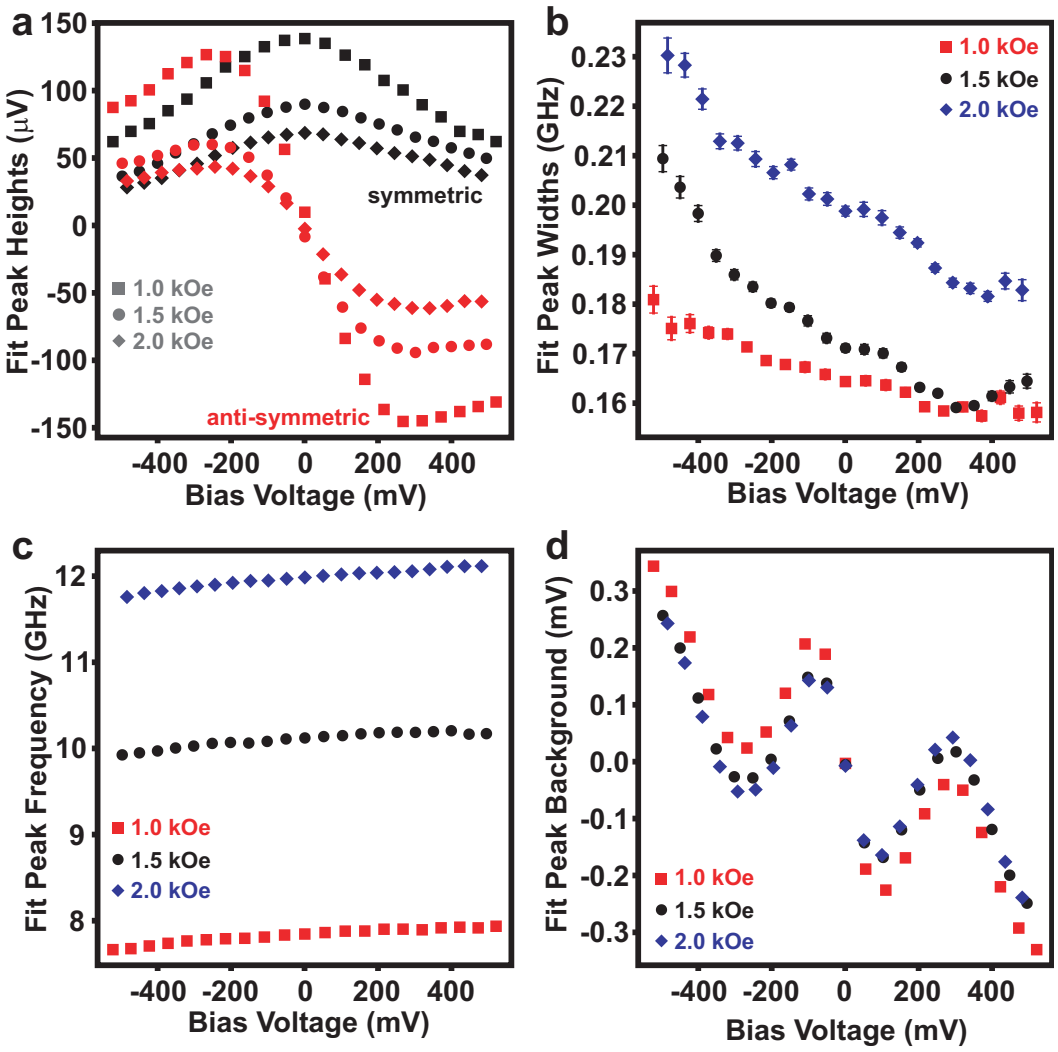


Figure 5.3: Fit parameters for the ST-FMR signals at room temperature, for three values of magnetic field in the $\hat{z}$ direction and $I_{RF} \approx 12\mu$A. (a) Amplitude of the symmetric and antisymmetric Lorentzian component of each peak. (b) The linewidths $\sigma/2\pi$. (c) The center frequencies $\omega_m/2\pi$. (d) Non-resonant background component.

As shown in Fig. 5.2b, the peak shapes for the ST-FMR signals of the lowest-frequency main resonance mode are fit very well by the form expected from Eq. 5.2. From the fits, at each value of H and I we determine with high precision the symmetric and antisymmetric peak amplitudes, the background, the linewidth σ, and the resonant frequency ω_m, as shown in Fig. 5.3. In order to make a quantitative determination of $d\tau_{||}/dI$ and $d\tau_{\perp}/dI$ using Eq. 5.2, it is necessary to calibrate the quantities I_{RF}^2 and $\partial^2 V/\partial\theta\partial I$, both of which depend on I due to the bias dependence of the tunnel-junction impedance. We determine I_{RF}^2 from the non-resonant background signal, together with the value of $\partial^2 V/\partial\theta\partial I$ determined at low frequency (appendix 5.4.3). We calibrate $\partial^2 V/\partial\theta\partial I$ by measuring $\partial V/\partial I$ vs. I at a sequence of magnetic fields in the $\hat{z}$ direction, assuming that the zero-bias conductance varies as $\cos(\theta)$ (and that θ depends negligibly on I), and then numerically differentiating $\partial V/\partial I$ with respect to θ at each value of I and H. These calibrations are sufficiently accurate that the uncertainty in our measurements is dominated by the uncertainty in the determination of $M_s Vol$, not I_{RF} or $\partial^2 V/\partial\theta\partial I$. Typical traces of I_{RF} and $\partial^2 V/\partial\theta\partial I$ vs. bias are shown in appendix 5.4.3.

The most relevant final quantities for physical interpretation are expected to be the "torkances" [98], defined as $d\tau_{||}/dV = (d\tau_{||}/dI)/(dV/dI)$ and $d\tau_{\perp}/dV = (d\tau_{\perp}/dI)/(dV/dI)$. We plot these in Fig. 5.4a, as calculated from the measured values of dV/dI and the values of $d\tau_{||}/dI$ and $d\tau_{\perp}/dI$ determined from the second term on the right side of Eq. (2). ($d\tau_{||}/dI$ and $d\tau_{\perp}/dI$ are plotted in Fig. 5.5.) We first consider the dependence of the torkances on θ. It is predicted [37, 94, 98] that for elastic tunneling $d\vec{\tau}/dV$ should be $\propto \sin(\theta)$. The inset to Fig. 5.4a shows that $(d\tau_{||}/dV)/\sin(\theta)$ is indeed nearly constant over the range of angles measured, $45° < \theta < 90°$. Given this agreement, we divide out a factor of $\sin(\theta)$ in plotting

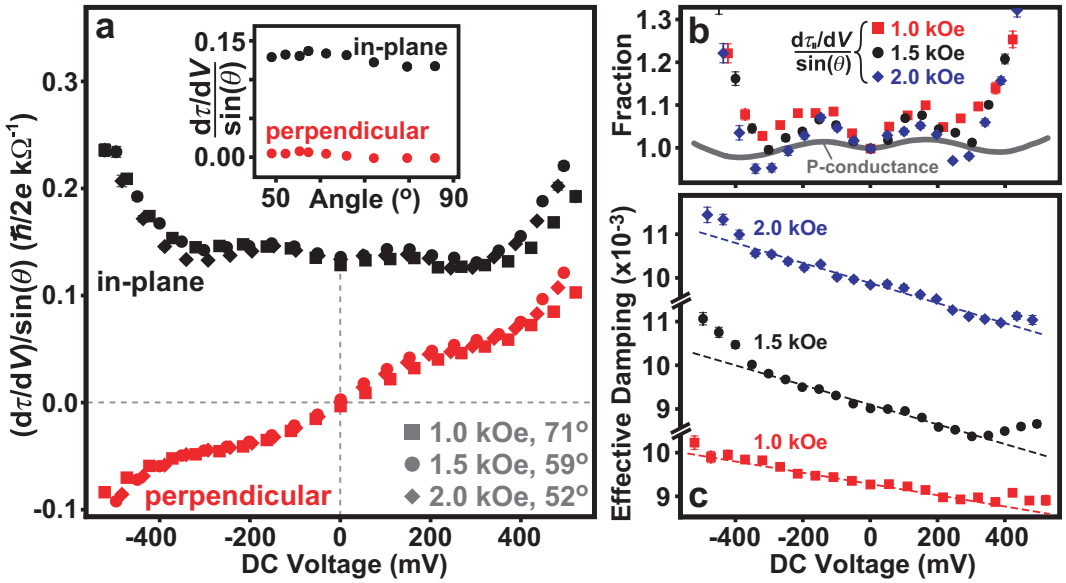


Figure 5.4: Bias dependence of the spin-transfer torkances and magnetic damping. (a) Magnitudes of the in-plane torkance $d\tau_{||}/dV$ and the out-of-plane torkance $d\tau_{\perp}/dV$ determined from the room temperature ST-FMR signals, for three different values of applied magnetic field in the $\hat{z}$ direction. The overall scale for the torkances has an uncertainty of $\sim 15\%$ associated with the determination of the sample's magnetic volume. (Inset) Angular dependence of the torkances at zero bias. (b) Comparison of the bias dependences of $d\tau_{||}/dV$ and $dI/dV(\mathrm{P})$, scaled by the zero-bias values. To aid the visual comparison of the variations, small linear background slopes (discussed in appendix 5.4.2) are subtracted from the torkance values. (c) Symbols: Effective damping determined from the ST-FMR linewidths. Lines: Fit to Eq. 5.5, for $|V| < 300$ mV.

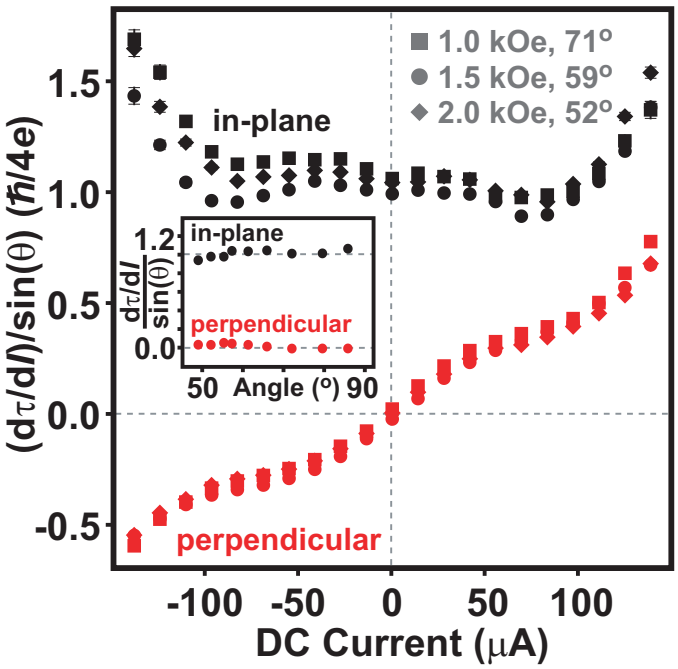


Figure 5.5: Magnitudes of the in-plane and out-of plane differential torques $d\tau_{||}/dI$ (black symbols) and $d\tau_{\perp}/dI$ (lighter symbols) vs. I, determined from fits to room-temperature ST-FMR spectra. The overall scale for the y-axis has an uncertainty of $\sim 15\%$ associated with the determination of the free-layer's magnetic volume. (Inset) Angular dependence of the differential torques at zero bias.

the torkances in the main panel of Fig. 5.4a, so that the plotted results should be independent of angle.

The bias dependence of the dominant, in-plane component of the torkance, $d\tau_{||}/dV$, is shown in the main panel of Fig. 5.4a. At $V = 0$, we find $d\tau_{||}/dV = 0.13 \pm 0.02\hbar/(2e)$ kΩ^{-1}, corresponding to an angular momentum transfer per electron of $(1.01 \pm 0.15)(\hbar/4)\sin(\theta)$. The angular momentum transfer per electron for elastic tunneling in a symmetric junction of polarization P is predicted to be $[2P/(1 + P^2)](\hbar/4)\sin(\theta)$, which is equal to $(\hbar/4)\sin(\theta)$ for perfect polarization and 0.92 $(\hbar/4)\sin(\theta)$ for a polarization of 0.66 (corresponding to our TMR of

154%) [98]. Therefore our measurement is in good agreement with the theoretical prediction, and to within the experimental uncertainty the strength of the torque is already equal to the maximum value predicted for elastic tunneling. Consequently, attempts to manipulate the composition of MTJs to achieve further increases in magnetoresistance are unlikely to lead to significantly stronger torques per unit current.

As a function of bias, we find that $d\tau_{||}/dV$ is constant to within 8% for $|V| < 300$ mV. This is in striking contrast to the magnetoresistance, which decreases by 50% over the same bias range (Fig. 5.1a). Furthermore, the value of $d\tau_{||}/dV$ appears to increase for 300 mV $< |V| <$ 540 mV, whereas the magnetoresistance continues to decrease to just 28% of its full value. The low-bias result confirms with greater sensitivity the conclusions in Ref. [93], in which a combined effect of $\tau_{||}/I$ and $\tau_{\perp}/I$ was measured for $|V| < 350$ mV in $Co_{90}Fe_{10}/MgO/Co_{90}Fe_{10}$ junctions.

The theoretical framework of Ref. [98] provides a means to analyze these results. Both the in-plane spin-transfer torkance and the differential conductance can be written in terms of conductance amplitudes $G_{\sigma\sigma'}$ between spin channels (σ, $\sigma' = \pm$ are spin indices for the bottom and top electrodes). Assuming that the tunneling mechanism itself does not depend on spin operators, we may then write [37, 98]

$$\frac{d\tau_{||}}{dV} = \frac{\hbar}{2e}(G_{++} - G_{--} + G_{+-} - G_{-+})\sin(\theta) \tag{5.3}$$

$$\frac{dI}{dV}(P) = G_{++} + G_{--}, \quad \frac{dI}{dV}(AP) = G_{+-} + G_{-+} \tag{5.4}$$

The amplitudes $G_{\sigma\sigma'}$ can describe both elastic and inelastic tunneling processes. With the assumptions that $G_{+-} \approx G_{-+}$ for a symmetric junction near zero bias and $G_{--} << G_{++}$, these equations imply that, approximately, $d\tau_{||}/dV \propto dI/dV(P)$. The observation that $d\tau_{||}/dV$ is approximately independent of bias for $|V| < 300$

mV can therefore be related to the fact that the differential conductance for parallel moments is approximately independent of bias in this range, as well. Figure 5.4b shows a direct comparison of the fractional changes in $d\tau_{||}/dV$ and $dI/dV(P)$ vs. V (relative to the zero-bias values). For $|V| < 300$ mV, $d\tau_{||}/dV$ and $dI/dV(P)$ display a similar pattern of non-monotonic variations, although the relative changes in $d\tau_{||}/dV$ are greater. At larger biases, 300 mV $< |V| <$ 540 mV, our determined value of $d\tau_{||}/dV$ increases much more rapidly than dI/dV. One possible explanation for this upturn may be heating. Previous studies of magnetic tunnel junctions [93, 104], suggest that the effective temperature of our free layer may be heated 50-100 K or more above room temperature at our highest biases. This could decrease the total magnetic moment of the free layer (M_sVol) thereby enhancing the response of the magnet to a given torkance and artificially inflating our determination of $d\tau_{||}/dV$ for $|V| > 300$ mV.

Within our macrospin ST-FMR model (leading to equation 5.2), the anti-symmetric-in-frequency component of the ST-FMR resonance is proportional to an out-of-plane torkance, $d\tau_{\perp}/dV$. We observe only symmetric ST-FMR peaks at $V = 0$ (Fig. 2b), implying that at zero bias $d\tau_{\perp}/dV = 0$. This differs from a previous experimental report [35]. Fig. 5.4a shows that the asymmetries we measure for $V \neq 0$ correspond to an approximately linear dependence of $d\tau_{\perp}/dV$ on V at low bias. This result is consistent with theoretical expectations [37, 95] that the lowest-order contribution to the bias dependence is $\tau_{\perp}(V)/\sin(\theta) = a_0 + a_2V^2$. For our full range of bias we measure $a_2 = (84 \pm 13)(\hbar/2e)$ GΩ^{-1}V^{-1}. The integrated torque $\tau_{\perp}(V)$ is in the $\mathbf{m}\times\mathbf{M}$ direction, and grows to be 30% of the in-plane torque $\tau_{||}(V)$ at the largest bias we probe. We do not believe that alternative mechanisms such as heating can account for these results, as explained in appendix 5.4.5.

We have also performed ST-FMR measurements on metallic IrMn / Py / Cu / Py spin valves in the same experimental geometry, and in that case we find that the lowest-frequency peaks are frequency-symmetric to within experimental accuracy for all biases $|I| < 2$ mA, from which we conclude that $\tau_\perp$ is always less than 1% of $\tau_{||}$ (see Fig. 5.6). The ratio $\tau_\perp/\tau_{||} < 1\%$ is much smaller than has been suggested based on analysis of the dynamical phase diagram of metal spin valves [105]. The existence of a significant perpendicular component of the spin torque therefore appears to be particular to tunnel junctions.

The measured linewidths σ of our ST-FMR measurements on MgO junctions allow a determination of the magnetic damping. Within our macrospin model (see section 5.4.2, assuming that $\tau_{||}(V,\theta) \propto \sin(\theta)$,

$$\sigma = \frac{\alpha\omega_m}{2}\left(\Omega_\perp + \Omega_\perp^{-1}\right) - \cot(\theta)\frac{\gamma_0\tau_{||}(V,\theta)}{2M_sVol}. \tag{5.5}$$

In Fig. 5.4c we plot the bias dependence of the effective damping defined as $\alpha_{eff} = 2\sigma/[\omega_m(\Omega_\perp + \Omega_\perp^{-1})]$. The zero-bias values give an average Gilbert damping coefficient $\alpha = 0.0095 \pm 0.0010$, consistent with literature reports for similar materials [106]. The lines plotted in Fig. 5.4c show the slopes expected from Eq. (5), using as a fitting parameter that $(d\tau_{||}/dV)/\sin(\theta) = (0.16 \pm 0.03)$ k$\Omega^{-1}\hbar/2e$ (assuming that $d\tau_{||}/dV$ is constant for $|V| < 300$ mV). This estimate agrees with the value determined independently above from the magnitude of the ST-FMR peak.

5.3 Conclusions

We have employed spin-transfer-driven FMR to achieve direct detailed quantitative measurements of both the direction and magnitude of the spin-transfer torque and

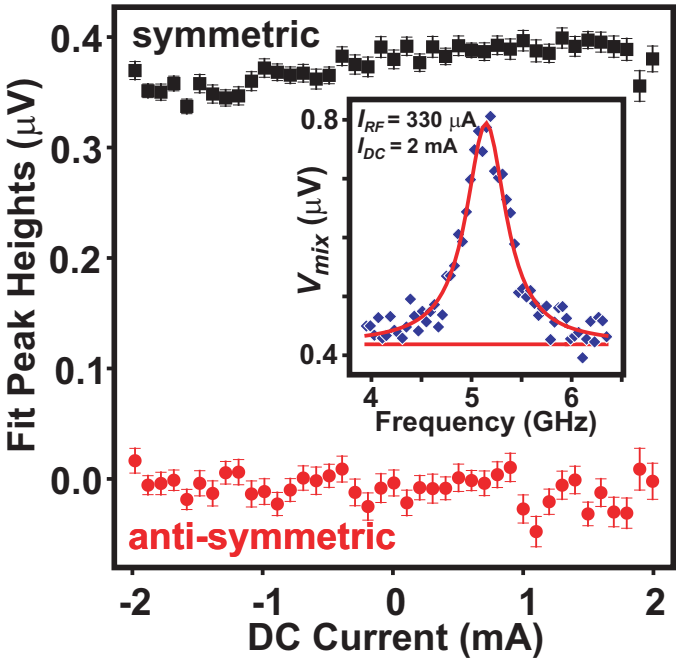


Figure 5.6: ST-FMR signals for a metallic spin valve, (in nm) Py 4 / Cu 80 / IrMn 8 / Py 4 / Cu 8 / Py 4 / Cu 2 / Pt 30, with $H = 560$ Oe in the plane of the sample along $\hat{z}$ and with an exchange bias direction 135 from $\hat{z}$. We estimate $\theta = 77°$ from the GMR. The average anti-symmetric Lorentzian component is $2 \pm 3\%$ the size of the symmetric Lorentzian component over this bias range. Accounting for the out-of-plane anisotropy $4\pi M_{eff} \sim 1$ T in Eq. 5.2 of the main paper, we estimate that the ratio $\tau_{\perp}/\tau_{||} < 1\%$.

magnetic damping in individual $Co_{60}Fe_{20}B_{20}/MgO/Co_{60}Fe_{20}B_{20}$ magnetic tunnel junctions, the type that are of interest for nonvolatile magnetic random access memory applications. We find that the dominant, in-plane component $d\tau_{||}/dV$ has a magnitude at zero bias equal to, within the experimental uncertainty of 15%, the maximum value predicted for highly-spin-polarized elastic tunneling. The torkance $d\tau_{||}/dV$ is independent of bias to within $\pm 8\%$ for $|V| \leq 300$ mV, and shows no evidence of weakening even at higher bias. We also observe for the first time a bias-dependent perpendicular component of the torque in magnetic tunnel junctions with, to a good approximation, $\tau_{\perp}(V) \propto V^2$, in agreement with predictions. This component of the torque is sufficiently strong at high bias that it should be included in device modeling, especially since it may help reduce the switching time and power consumption of the magnetic reversal process. Our findings about the rotation and strength of the torque under bias improve the feasibility of ST-MRAM.

5.4 Appendices

5.4.1 ST-FMR Artifacts Due to the Leads

The capacitance from the large contact pad and lower lead crossing in Fig. 5.1b (inset) draws a substantial RF current across the top lead, compared to the amount passing through these highly-resistive junctions. This RF current flowing across the top lead applies an RF magnetic field with a phase different to the current flowing through the junction, thereby driving the precession and affecting both the symmetry and magnitude of the ST-FMR peaks. It also causes the FMR results to vary depending on which of the two top contacts (A or B) is used, while the results are the same upon interchanging bottom contacts (C or D). Similar effects from RF currents flowing past the tunnel junction may also have affected a previous ST-FMR measurement of MgO devices [35], which showed significantly asymmetric lineshapes even at zero DC bias. To minimize this problem, we cut the top lead near the sample as labeled in Fig. 5.1b (left inset), and then perform the ST-FMR measurements using contacts B and D.

This is not an issue in the metallic spin valves of the previous chapters due to their low resistance.

5.4.2 Derivation of the ST-FMR Signal (Eq. 5.2)

This derivation generalizes arguments in references [35,102,103] in order to consider experiments in which a finite bias is applied to the sample.

We consider only the specific geometry relevant to our experiment and define the coordinate axes as in Ref. [102]. We assume that the orientation $\mathbf{m}$ of the free-layer moment undergoes small-angle precession about the $\hat{z}$ axis, the plane of

the sample is the $\hat{y} - \hat{z}$ plane, the easy axis of the free layer is along $\hat{y}$, and that the orientation $\mathbf{M}$ of the fixed-layer moment is in the plane of the sample, differing from $\hat{z}$ by an angle θ_0 toward $\hat{y}$. Let θ be the angle between $\mathbf{m}$ and $\mathbf{M}$. The small-angle precession of the free layer in response to the current $I(t) = I + \delta I(t)$ (where $\delta I(t) = I_{RF}\Re(e^{i\omega t})$) can be characterized by the transverse components $m_x(t) = \Re(m_x e^{i\omega t})$ and $m_y(t) = \Re(m_y e^{i\omega t})$. Because of the large magnetic anisotropy of the thin film sample, $m_x << m_y$ and changes in the angle θ during precession are to good approximation $\delta\theta(t) = -\Re(m_y e^{i\omega t})$.

The time-dependent voltage $V(t)$ across the sample will depend on the instantaneous value of the current and θ. The DC voltage signal produced by rectification in ST-FMR can be calculated by Taylor-expanding $V(t)$ to second order and taking the time average over one precession period:

$$\langle V_{mix} \rangle = \frac{1}{2}\frac{\partial^2 V}{\partial I^2}\left\langle (\delta I(t))^2 \right\rangle + \frac{\partial^2 V}{\partial I \partial \theta}\left\langle \delta I(t)\delta\theta(t) \right\rangle + \frac{1}{2}\frac{\partial^2 V}{\partial \theta^2}\left\langle (\delta\theta(t))^2 \right\rangle. \tag{5.6}$$

Here $\langle\rangle$ denotes the time average. With this expression, we assume that voltage signals due to spin pumping [103] are negligible in tunnel junctions. Using $\delta\theta(t) = -\Re(m_y e^{i\omega t})$, Eq. 5.6 can be expressed

$$\langle V_{mix} \rangle = \frac{1}{4}\frac{\partial^2 V}{\partial I^2} I_{RF}^2 - \frac{1}{2}\frac{\partial^2 V}{\partial I \partial \theta} I_{RF}\Re(m_y) + \frac{1}{4}\frac{\partial^2 V}{\partial \theta^2}|m_y|^2. \tag{5.7}$$

We calculate the precession angle m_y from the Landau-Lifshitz-Gilbert equation of motion in the macrospin approximation, with the addition of spin-transfer-torque terms transverse to the free-layer moment.

$$\frac{\partial \mathbf{m}}{\partial t} = -\gamma_0 \mathbf{m} \times \mathbf{H_{eff}} + \alpha \mathbf{m} \times \frac{\partial \mathbf{m}}{\partial t} - \gamma_0 \frac{\tau_{||}(I,\theta)}{M_s Vol}\hat{y} - \gamma_0 \frac{\tau_{\perp}(I,\theta)}{M_s Vol}\hat{x} \tag{5.8}$$

where γ_0 is the magnitude of the gyromagnetic ratio, α is the Gilbert damping coefficient, and $M_s Vol$ is the total magnetic moment of the free layer. For our

specific experimental geometry, $\mathbf{H_{eff}} = -N_x M_{eff}\hat{x} - N_y M_{eff}\hat{y}$ with $N_x = 4\pi + (H/M_{eff})$ and $N_y = (H - H_{anis})/M_{eff}$. Here H is the external magnetic field, $4\pi M_{eff}$ is the effective anisotropy perpendicular to the sample plane, and H_{anis} denotes the strength of anisotropy within the easy plane. (If the precession axis is not along a high-symmetry direction like $\hat{z}$, there are additional off-diagonal demagnetization terms in $\mathbf{H_{eff}}$ that will make the general expression for the ST-FMR signal more complicated than the one that we derive here [102].)

For small RF excitation currents, the spin-torque terms can be Taylor-expanded:

$$\tau_{||}(I,\theta) = \tau_{||}^0 + \frac{\partial \tau_{||}}{\partial I}\delta I(t) + \frac{\partial \tau_{||}}{\partial \theta}\delta\theta(t), \quad \tau_{\perp}(I,\theta) = \tau_{\perp}^0 + \frac{\partial \tau_{\perp}}{\partial I}\delta I(t) + \frac{\partial \tau_{\perp}}{\partial \theta}\delta\theta(t) \quad (5.9)$$

We have used a different sign convention than Ref. [102], so that the variables η_1 and η_2 in Ref. [102] correspond at zero bias to $\eta_1 = -(2e/\hbar \sin\theta)/(\partial\tau_{||}/\partial I) \equiv -\zeta_{||}$ and $\eta_2 = -(2e/\hbar \sin\theta)/(\partial\tau_{\perp}/\partial I) \equiv -\zeta_{\perp}$ in our notation.

The oscillatory terms in the equation of motion are

$$\begin{aligned} i\omega m_x &= -m_y(\gamma_0 N_y M_{eff} + i\alpha\omega) - \frac{\gamma_0}{M_s Vol}\left(\frac{\partial \tau_{\perp}}{\partial I} I_{RF} - \frac{\partial \tau_{\perp}}{\partial \theta} m_y\right), \\ i\omega m_y &= m_x(\gamma_0 N_x M_{eff} + i\alpha\omega) - \frac{\gamma_0}{M_s Vol}\left(\frac{\partial \tau_{||}}{\partial I} I_{RF} - \frac{\partial \tau_{||}}{\partial \theta} m_y\right). \end{aligned} \quad (5.10)$$

At this stage, we have neglected the influence of the DC spin-torque terms in shifting the precession axis of the free layer away from $\hat{z}$. For the bias range of our experiment, this is a very small effect. Solving these equations for m_y to lowest order in the damping coefficient α we have

$$m_y = \frac{\gamma_0 I_{RF}}{2M_s Vol}\frac{1}{\omega - \omega_m - i\sigma}\left[i\frac{\partial \tau_{||}}{\partial I} + \frac{\gamma_0 N_x M_{eff}}{\omega_m}\frac{\partial d\tau_{\perp}}{\partial I}\right]. \quad (5.11)$$

Here, the resonant precession frequency $\omega_m = \gamma_0 M_{eff}\sqrt{N_x N_y}$ and the linewidth

$$\sigma = \frac{\alpha\gamma_0 M_{eff}(N_x + N_y)}{2} - \frac{\gamma_0}{2M_s Vol}\frac{\partial \tau_{||}}{\partial \theta}. \quad (5.12)$$

In the expression for the resonant precession frequency, we have neglected a correction $\propto \partial\tau_\perp/\partial\theta$ that is negligible for our experiment. The small shifts in the resonant frequency that we measure as a function of bias – see Fig. 5.3c – may be associated with micromagnetic phenomena that go beyond our macrospin approximation [60].

If we define $S(\omega) = 1/[1 + (\omega - \omega_m)^2/\sigma^2]$, $A(\omega) = [(\omega - \omega_m)/\sigma]S(\omega)$, and $\Omega_\perp = \gamma_0 N_x M_{eff}/\omega_m$, and substitute Eq. 5.11 into Eq. 5.7, we reach

$$\begin{aligned}\langle V_{mix}\rangle &= \frac{1}{4}\frac{\partial^2 V}{\partial I^2} I_{RF}^2 + \frac{1}{2}\frac{\partial^2 V}{\partial\theta\partial I}\frac{\hbar\gamma_0 \sin\theta}{4eM_s Vol\sigma} I_{RF}^2 \left(\zeta_{||} S(\omega) - \zeta_\perp \Omega_\perp A(\omega)\right) \\ &+ \frac{1}{4}\frac{\partial^2 V}{\partial\theta^2}\left(\frac{\hbar\gamma_0 \sin\theta}{4e\sigma M_s Vol}\right)^2 I_{RF}^2(\zeta_{||}^2 + \zeta_\perp^2\Omega_\perp^2) S(\omega). \qquad (5.13)\end{aligned}$$

The final term in Eq. 5.13 represents a DC voltage generated by a change in the average low-frequency resistance due to magnetic precession. This term should be approximately an odd function of bias, and we estimate that it is small in the bias range we explore. It may be the explanation for the small slope in the dependence of $d\tau_{||}/dV$ vs. bias that we subtract off in Fig. 5.4b of the main text of this chapter; however we find that the dominant contribution to the frequency-symmetric component of the ST-FMR signal is symmetric in bias. For these reasons we do not consider this final term in the main text. The first two terms on the right in Eq. 5.13 are then identical to Eq. 5.2 in the main text.

Equation 5.5 in the main text follows from equation 5.12 after using $\omega_m = \gamma_0 M_{eff}\sqrt{N_x N_y}$ and assuming that $\tau_{||}(I,\theta) \propto \sin(\theta)$.

5.4.3 Details of the Calibration of I_{RF}^2

The calibration of I_{RF}^2 is performed in two steps: (1) a flatness correction and (2) accounting for the bias dependence of the sample impedance. The flatness

correction ensures that the microwave current within the sample I_{RF} does not vary with frequency. We apply an external magnetic field H with magnitude chosen so that all magnetic resonances have frequencies higher than the range of interest, and then measure the ST-FMR background signal as a function of frequency for a fixed DC bias ($|I| > 10\mu$A). Due to circuit resonances and losses, this background signal may vary as the frequency is changed. At the same time, we determine $\partial^2 V/\partial I^2$ by measuring $\partial V/\partial I$ versus I with low-frequency lock-in techniques and then differentiating numerically. We can then determine the variations of I_{RF} with frequency using the formula for the non-resonant background (first term in Eq. 5.13):

$$\langle V_{background} \rangle = \frac{1}{4} \frac{\partial^2 V}{\partial I^2} I_{RF}^2. \tag{5.14}$$

We input this information to the microwave source, and employ its flatness-correction option to modulate the output signal so that the final microwave current coupled to the sample no longer varies with frequency.

(2) After step (1), I_{RF} is leveled vs. frequency and its magnitude can be determined for one set of values I_0 and H_0. However, because the sample impedance varies as a function of I and H, we must also determine how I_{RF} varies as these quantities are changed. In order to do this accurately even at points where $\partial^2 V/\partial I^2$ is near zero, we calculate $I_{RF}(I, H)$ by taking into account how variations in dI/dV alter the termination of the transmission line, assuming that the impedance looking out from the junction is 50 Ω:

$$I_{RF}(I, H) = I_{RF}(I_0, H_0) \left[\frac{dV}{dI}(I_0, H_0) + 50\Omega \right] / \left[\frac{dV}{dI}(I, H) + 50\Omega \right]. \tag{5.15}$$

In practice, we generally determine $I_{RF}(I_0, H_0)$ using Eq. 5.14 together with the value of the non-resonant background at one choice of I_0 for each value of magnetic field, and then employ Eq. 5.15 to find the full I dependence.

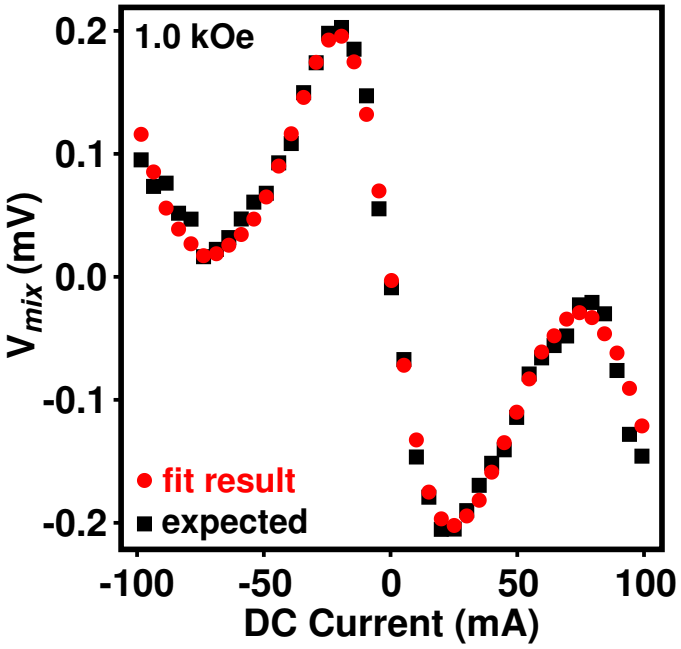


Figure 5.7: Test of the calibration for I_{RF} and the non-resonant background, for $H = 1.0$ kOe in the $\hat{z}$ direction. Circles: Magnitude of non-resonant background measured from fits to the ST-FMR peaks. Squares: the background expected from equations 5.14 and 5.15 after determining $I_{RF} = 11.7$ μA at $I_0 = -30\mu$A.

Figure 5.7 shows that this procedure successfully reproduces the measured non-resonant background signal as a function of I_0, using as input the bias dependence of dV/dI measured at low frequency. This demonstrates that there are no high-frequency phenomena which cause the background signal to deviate significantly from the simple rectification signal caused by non-linearities in the low-frequency current-voltage curve. Figure 5.8 shows the typical change in I_{RF} as described by Eq. 5.15.

5.4.4 Regarding a Possible Alternative Mechanism for the Antisymmetric Lorentzian Component of the ST-FMR Signal

Kovalev *et al.* [102] and Kupferschmidt *et al.* [103] have noted that a component of the ST-FMR signal that is antisymmetric in frequency relative to the center frequency can arise if the precession axis of the free layer moment is tilted out away from the sample plane and not along any of the principle axes of the magnetic anisotropy. In principle, this mechanism could explain an observation of an antisymmetric ST-FMR signal that varies linearly with DC current I, because the in-plane component of spin-transfer torque from I will cause the equilibrium orientation of the free-layer moment to move out-of-plane (until the torque from the demagnetization field balances the in-plane spin-transfer-torque). However, when evaluating this mechanism quantitatively, we find that it predicts an antisymmetric component 50 times smaller than we measure.

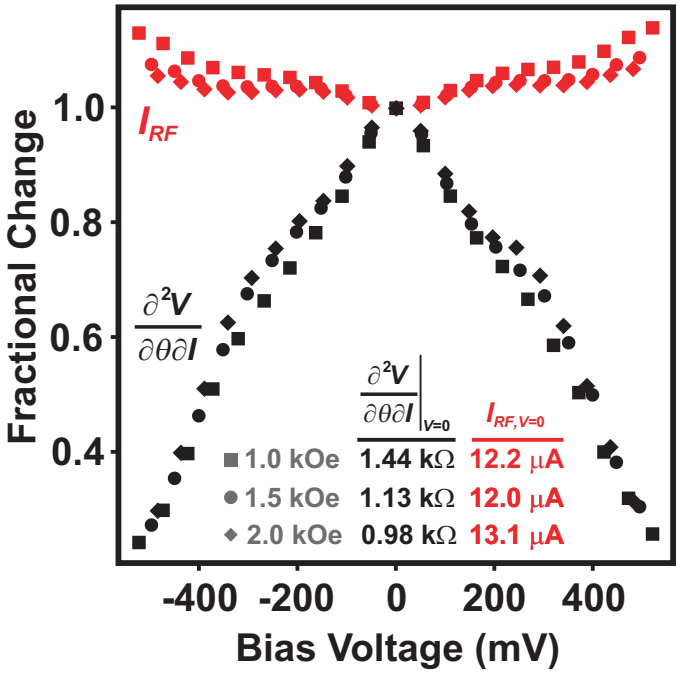


Figure 5.8: Representative examples of the bias dependence of I_{RF} and $\partial^2 V/\partial\theta\partial I$ for H in the $\hat{z}$ direction. Values of I_{RF} and $\partial^2 V/\partial\theta\partial I$ at $V = 0$ are labeled. I_{RF} is determined using the procedure described above. $\partial^2 V/\partial\theta\partial I$ is determined by measuring $\partial V/\partial I$ vs. I at a sequence of magnetic fields in the $\hat{z}$ direction, by assuming that the conductance changes at zero bias are proportional to $\cos(\theta)$ and that θ depends negligibly on I, and then by performing a local linear fit to determine $\partial^2 V/\partial\theta\partial I$ for given values of I and H.

5.4.5 Regarding the Effects of Heating on Measurements of the Perpendicular Torkance

In principle, heating might affect the ST-FMR measurements through several mechanisms. Here we consider only whether a heating effect might be able to explain our observation that the ST-FMR signal contains a perpendicular component with an antisymmetric Lorentzian lineshape, whose magnitude depends approximately linearly on I (i.e., we consider heating as an alternative mechanism to the out-of-plane torkance discussed in the main paper.) If Ohmic heating is the dominant source of heating, then the sample temperature may have an RF component proportional to $dT(t) \sim R(I + I_{RF}(t))^2 \sim 2RI_{RF}I\cos(\omega t + \delta_T)$ (after subtracting the constant contribution $\propto RI^2$ and assuming $I > I_{RF}$), where δ_T is a possible phase lag. If heating changes the resistance of the sample, this would give an additional contribution to the resonant part of the ST-FMR signal of the form $\langle V_{mix}\rangle \propto (\partial V/\partial\theta\partial T)\langle\delta\theta(t)\delta T(t)\rangle \propto (\partial V/\partial\theta\partial T)I_{RF}I\Re(m_y e^{-i\delta_T})$. However, since $\partial V/\partial\theta\partial T$ in this expression is proportional to I, the lowest-order contribution to the ST-FMR signal from this mechanism is proportional to I^2, so that it cannot explain the linear dependence of the asymmetric component on I observed experimentally.

An antisymmetric-in-frequency ST-FMR signal linear in I could result if the Peltier effect, rather than Ohmic heating, were the dominant heating mechanism. However, our differential conductance measurements do not show a large asymmetry with respect to bias that would be expected if this were the case. A resonant signal linear in I could also result if the dominant consequence of heating were not to change the resistance, but to apply a torque to $\mathbf{m}$ by changing the demagnetization or dipole field. We expect that this last mechanisms might be significant if

the free layer were tilted partially out of the sample plane, but we estimate that it is insignificant for our measurements in which the free-layer moment is in plane and aligned within a few degrees of the symmetry axis $\hat{z}$.

For these reasons, we believe it is unlikely that heating, rather than a direct out-of-plane spin-transfer torque, can explain the antisymmetric component of the ST-FMR signal that we observe.

Chapter 6

Appendices

6.1 A Quick Note on Microwave Coupling in Our System

I wanted to add a short section about microwave coupling in our system, since I am responsible for the "spaceship-shaped" leads defined during fabrication (Fig. 6.1). The motivation for the shape of these leads is to (a) allow comfortable contact with the microwave probes (or ribbon bonds) from any of the eight angles in 45° increments, (b) minimize capacitive coupling between the top and bottom leads, and (c) keep the overall device size small, minimizing capacitive coupling between the pads and the silicon (which conducts at microwave frequencies) below the oxide surface of our wafers. We made no attempt to create a "50-Ω impedance-matched waveguide" here, because the wavelengths of the microwave signals we generally deal with are much longer than 500 μm. The rule of thumb is if the entire structure is roughly 5-10 times smaller than the wavelength, it can be treated as a lumped-element termination [47].

6.2 A Quick Note on Pulsed RF Measurements

In as-yet unpublished work, I have developed a technique for applying very short (between $\sim$ 1 ns and 10 ns) pulses of RF ("radio frequency") current to a spin-valve sample to try and resonantly switch it, and have even begun to test the system on a few samples.

In creating a pulse of RF current, there are several issues to address. One might consider simply using the internal pulsing mechanism of the swept signal genera-

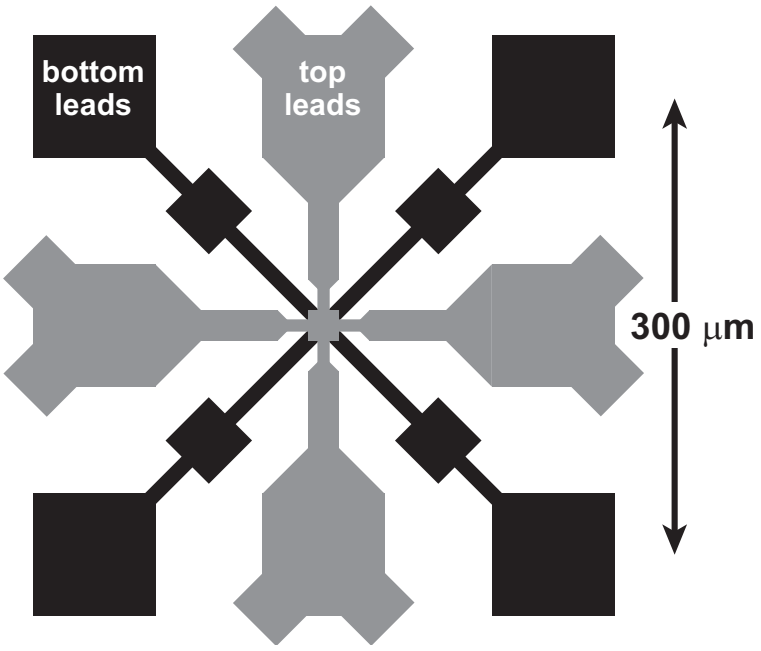


Figure 6.1: Sketch of the photolithographically-defined leads for making high frequency electrical contact to our devices. The whole structure is much smaller than the wavelengths of interest, so we treat it as a lumped-element termination.

tors, but unfortunately the cannot apply fast enough pulses for our application, and the rising edge of the pulse is uncorrelated with the phase of the RF current. In order to get a fast RF pulse, we use a mixer in reverse, a technique explained to us by Robert Schoelkopf. Ordinarily, a mixer takes two high-frequency signals on the LO ("local oscillator") and RF ports and puts out a low-frequency signal at the IF ("intermediate frequency") port; the nonlinear element inside mixes the two high-frequency signals into the sums and differences of their frequencies. If one of the input frequencies is zero and the other is f, then that same element will generate a mixed signal at f. This effectively turns the mixer into a gate that allows high-frequency signals to propagate from LO to RF (or backwards) whenever a DC voltage is applied to IF. The only difference between the three ports on our mixers is the filter. All you need to do is pick a mixer with the appropriate filters: the right frequency range on LO and RF, and a fast enough low-pass on IF to give you the rising edge you desire. The idea is then to apply continuous RF current to the LO (or RF) ports and pulse the IF port.

The second and most difficult issue is that we wish to control the phase of the RF relative to the IF-port pulse, so that we can see how this affects the resonant switching. It is relatively easy to generate a low-frequency rising edge that is phase-coherent (to within less than 5 ps jitter) with the RF source using frequency dividers, which are basically 1-bit processors with the clock timing defined by the RF you feed them.[1] RF Bay Inc. have excellent and cheap frequency dividers to turn 1-15GHz (better than specs) RF source into 0-1 GHz ECL pulses, and then Pulse Research Labs sells nice (but very fragile) variable-division boxes to divide

[1]These are designed to run at clock speeds up to 15 GHz, which is much faster than today's computer processors. They get very hot!

further to the kHz-MHz range, and generate TTL pulses.[2] The resulting signal, however is a continuous square wave, so we need to somehow arm the pulser to take the rising edge we desire as a trigger. Unfortunately, no pulsers I have used are equipped with the option to "arm a pulse and take the next rising edge as a trigger" without running into the problem that occurs (more often than one might expect) when it arms at the same time as the trigger edge arrives and enormous jitter ensues. This issue was a source of great hair loss until finally, Saikat Ghosh told me to use the built-in logic on our DAQ card[3], which can generate a pulse in sync with the output of the frequency divider to use as a gate.

Figure 6.2 shows a schematic of the logic sequences used to generate a pulse. Half of the RF power is sent to the mixer LO port, and the other half is sent to the frequency division circuit, which generates a TTL square wave we use to define the clock of the DAQ card logic, as well as triggering the pulser. When the computer tells the DAQ logic to fire, a few cycles later it produces a pulse two clock cycles long, that we use to gate the pulser. When the voltage at the gate is high, the pulser accepts triggers (falling edges work well in this case) and will fire the fast pulse desired to let a small amount of RF through the mixer. In order to avoid the situation where the DAQ logic and the rising edge arrive at the pulser simultaneously (which can surprisingly cause a trigger event), we require a delay somewhere in the system. There is a natural delay in the DAQ card that takes care of this in some systems, but if they are too close, a simple 100-foot BNC coaxial line on either the clock or the DAQ logic output will take care of it.

There is also a substantial intrinsic delay between the rising edge of the RF

[2]They now have a nice 0-15 GHz box too.

[3]"DAQ" is short for "Data AcQuisition". A DAQ card has many functions, mainly reading voltages quickly into a computer and digital logic described here.

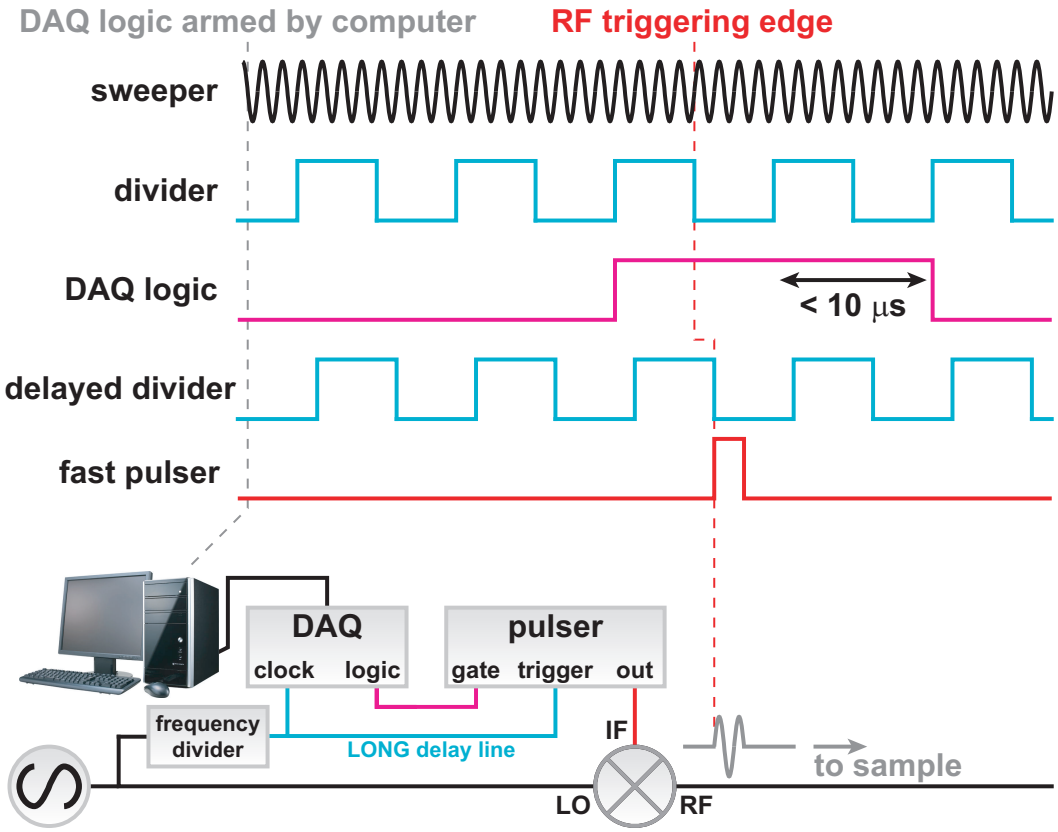


Figure 6.2: Diagram of the sequencing to generate a pulse of RF current. The output of the sweeper is divided to a MHz-frequency TTL square-wave that is fed into the DAQ card as a reference clock. When we tell the computer to fire, it sends a message to the DAQ logic to output a pulse that is 2 cycles long, which is fed into the pulser's gate. When the gate is high, the pulser uses the next descending edge to trigger. By adding delay to the frequency divider prior to the pulse trigger, we can increase the sensitivity of the RF phase to small changes in frequency.

and the divided signal edges. This is *great* in our case, because it means that many RF cycles pass before the pulse hits the mixer, so a small change in RF frequency will produce a large change in the RF phase relative to the pulse. We can control the phase with a small tweak of the frequency, much smaller than the resonant features in our nanomagnetic system. Adding more delay to the divided signal will improve this sensitivity.

Finally, we want to vary the amplitude of the RF pulse. The divider circuit has a specific range of power required to run, so we must keep it in this range while changing the RF power. To take care of this, we use a GPIB-controlled variable attenuator. Essentially, we turn the RF source to very high power and attenuate it on each leg of the circuit. A constant attenuator is used on the way to the mixer, and the variable attenuator is used on the way to the divider. The computer can then automatically adjust it based on simple power-setting rules.

Adding a second pulse underneath this RF pulse is a snap. Just find a second pulser (not as much of a snap) and use the same signals from the DAQ logic and frequency divider to generate a second pulse, and then a splitter/combiner to combine the two signals. Coarse timing adjustments can be made with the pulser, and fine adjustments can be made with small SMA extension connectors. We have used AD811AN op-amps with great success to boost the TTL signals to the necessary levels to trigger both pulsers, but be careful not to overload the pulser inputs! With amplifiers in the mix, it is quite easy to do, and they can only withstand a few volts.

As a last warning, the Picosecond 10,070A pulsers will fire twice if you leave the gate high for more than 10 μs, so watch the length of the gate pulses!

BIBLIOGRAPHY

[1] N. C. Emley, Ph.D. Dissertation, Cornell University (2005)

[2] J. C. Slonczewski, *J. Magn. Magn. Mater* **159**, L1, (1996)

[3] L. Berger, *Phys. Rev. B* **54**, 9353, (1996)

[4] J. C. Slonczewski, *Phys. Rev. B* **71**, 024411, (2005)

[5] S. I. Kiselev, J. C. Sankey, I. N. Krivorotov, N. C. Emley, M. Rinkoski, C. Perez, R. A. Buhrman, and D. C. Ralph, *Phys. Rev. Lett.* **93**, 036601, (2004)

[6] N. W. Ashcroft and N. D. Mermin *Solid State Physics*, 671, (Harcourt College Publishers, 1976)

[7] J. C. Slonczewski, *J. Magn. Magn. Mater* **247**, 324, (2002)

[8] M. D. Stiles, J. Xiao, and A. Zangwill, *Phys. Rev. B* **69**, 054408, (2004)

[9] J. Xiao, A. Zangwill, and M. D. Stiles, *Phys. Rev. B* **70**, 172405, (2004)

[10] E. B. Myers, D. C. Ralph, J. A. Katine, R. N. Louie, and R. A. Buhrman, *Science* **285**, 867, (1999)

[11] J. A. Katine, F. J. Albert, R. A. Buhrman, E. B. Myers, and D. C. Ralph, *Phys. Rev. Lett.* **84**, 4212, (2000)

[12] M. D. Stiles, W.M. Saslow, M. J. Donahue, A. Zangwill cond-mat/0702020 (2007)

[13] G. Bertotti, C. Serpico, I. D. Mayergoyz, A. Magni, M. d'Aquino, and R. Bonin, *Phys. Rev. Lett.* **94**, 127206, (2005)

[14] M. Tsoi, A. G. M. Jansen, J. Bass, W.-C. Chiang, M. Seck, V. Tsoi, and P. Wyder, *Phys. Rev. Lett.* **80**, 4281-4284, (1998)

[15] J. Z. Sun, *J. Magn. Magn. Mater* **202**, 157, (1999)

[16] J. Grollier, V. Cros, A. Hamzic, J. M. George, H. Jaffrs, A. Fert, G. Faini, J. Ben Youssef and H. Legall, *Appl. Phys. Lett.* **78**, 3663, (2001)

[17] P. Guittienne, J. E. Wegrowe, D. Kelly, and J. P. Ansermet, *IEEE Trans. Magn.* **37**, 2126, (2001)

[18] M. Tsoi, A. G. M. Jansen, J. Bass, W.-C. Chiang, V. Tsoi, P. Wyder, *Nature* (London) **406**, 46, (2000)

[19] E. B. Myers, F. J. Albert, J. C. Sankey, E. Bonet, R. A. Buhrman, and D. C. Ralph, *Phys. Rev. Lett.* **89**, 196801, (2002)

[20] J. Z. Sun, *Phys. Rev. B* **62**, 570, (2000)

[21] Z. Li and S. Zhang, *Phys. Rev. B* **68**, 024404, (2003)

[22] J. Miltat, G. Albuquerque, A. Thiaville, and C. Vouille, *J. Appl. Phys.* **89**, 6982, (2001)

[23] S. Zhang, P. M. Levy, and A. Fert, *Phys. Rev. Lett.* **88**, 236601, (2002)

[24] G. Tatara and H. Kohno, *Phys. Rev. Lett.* **92**, 086601, (2004)

[25] *J. Phys. Chem. Solids* **1**2091957

[26] D. V. Berkov and N. L. Gorn, *Phys. Rev. B* **72**, 094401, (2005)

[27] S. I. Kiselev, J. C. Sankey, I. N. Krivorotov, N. C. Emley, A. G. F. Garcia, R. A. Buhrman, and D. C. Ralph, *Phys. Rev. B* **72**, 064430, (2005)

[28] R. H. Koch, J. A. Katine, and J. Z. Sun, *Phys. Rev. Lett.* **92**, 088302, (2004)

[29] S. E. Russek, S. Kaka, W. H. Rippard, M. R. Pufall, and T. J. Silva, *Phys. Rev. B* **71**, 104425, (2005)

[30] P. M. Braganca, I. N. Krivorotov, O. Ozatay, A. G. F. Garcia, N. C. Emley, J. C. Sankey, D. C. Ralph, and R. A. Buhrman, *Appl. Phys. Lett.* **87**, 112507, (2005)

[31] G. D. Fuchs, J. A. Katine, S. I. Kiselev, D. Mauri, K. S. Wooley, D. C. Ralph, and R. A. Buhrman, *Phys. Rev. Lett.* **96**, 186603, (2005)

[32] I. N. Krivorotov, N. C. Emley, J. C. Sankey, S. I. Kiselev, D. C. Ralph, and R. A. Buhrman, *Science* **307**, 228, (2005)

[33] B. Montigny and J. Miltat, *J. Appl. Phys.* **97**, 10C708, (2005)

[34] L. Torres, L. Lopez-Diaz, E. Martinez, M. Carpentieri and G. Finocchio, *J. Magn. Magn. Mater* **286**, 381, (2005)

[35] A. A. Tulapurkar, Y. Suzuki, A. Fukushima, H. Kubota, H. Maehara, K. Tsunekawa, D. D. Djayaprawira, N. Watanabe, S. Yuasa, *Nature* (London) **438**, 339, (2005)

[36] W. H. Rippard, M. R. Pufall, S. Kaka, T. J. Silva, S. E. Russek, and J. A. Katine, *Phys. Rev. Lett.* **95**, 067203, (2005)

[37] J. C. Slonczewski, *Phys. Rev. B* **39**, 6995, (2005)

[38] Ya. B. Bazaliy, B. A. Jones, and Shou-Cheng Zhang, *Phys. Rev. B* **57**, R3213, (1998)

[39] M. D. Stiles and A. Zangwill, *Phys. Rev. B* **65**, 014407, (2002)

[40] J.-E. Wegrowe, A. Fbin, Ph. Guittienne, X. Hoffer, D. Kelly, J.-Ph. Ansermet, and E. Olive, *Appl. Phys. Lett.* **80**, 3775, (2002)

[41] J. Z. Sun, D. J. Monsma, D. W. Abraham, M. J. Rooks, and R. H. Koch, *Appl. Phys. Lett.* **81**, 2202, (2002)

[42] G. E. W. Bauer, Y. Tserkovnyak, D. Huertas-Hernando, and A. Brataas, *Phys. Rev. B* **67**, 094421, (2003)

[43] W. H. Rippard, M. R. Pufall, and T. J. Silva, *Appl. Phys. Lett.* **82**, 1260, (2003)

[44] B. Özyilmaz, A. D. Kent, D. Monsma, J. Z. Sun, M. J. Rooks, and R. H. Koch, *Phys. Rev. Lett.* **91**, 067203, (2003)

[45] S. Urazhdin, Norman O. Birge, W. P. Pratt, Jr., and J. Bass, *Phys. Rev. Lett.* **91**, 146803, (2003)

[46] M. N. Baibich, J. M. Broto, A. Fert, F. Nguyen Van Dau, F. Petroff, P. Etienne, G. Creuzet, A. Friederich, and J. Chazelas, *Phys. Rev. Lett.* **61**, 2472, (1988)

[47] D. M. Pozar *Microwave Engineering* 2nd edn, 566 (John Wiley & Sons, New York, 1996)

[48] C. Kittel *Introduction to Solid State Physics* 7th edn, 505 (John Wiley & Sons, New York, 1996)

[49] M. T. Johnson, P. J. H. Bloemen, F. J. A. den Broeder and J. J. de Vries, *Rep. Prog. Phys.*5914091996

[50] R. D. McMichael and M. D. Stiles, *J. Appl. Phys.* **97**, 10J901, (2005)

[51] C. H. Lee, R. F. C. Farrow, C. J. Lin, E. E. Marinero, and C. J. Chien, *Phys. Rev. B* **42**, 1066, (1990)

[52] M. R. Pufall, W. H. Rippard, Shehzaad Kaka, S. E. Russek, T. J. Silva, Jordan Katine, and Matt Carey, *Phys. Rev. B* **69**, 214409, (2004)

[53] I. N. Krivorotov, N. C. Emley, A. G. F. Garcia, J. C. Sankey, S. I. Kiselev, D. C. Ralph, and R. A. Buhrman, *Phys. Rev. Lett.* **93**, 166603, (2004)

[54] J. C. Sankey, I. N. Krivorotov, S. I. Kiselev, P. M. Braganca, N. C. Emley, R. A. Buhrman, and D. C. Ralph, *Phys. Rev. B* **72**, 224427, (2005)

[55] J. Xiao, A. Zangwill, and M. D. Stiles, *Phys. Rev. B* **72**, 014446, (2005)

[56] A. V. Nazarov, H. S. Cho, J. Nowak, S. Stokes, and N. Tabat, *Appl. Phys. Lett.* **81**, 4559, (2002)

[57] Ya. B. Bazaliy, B. A. Jones, and S. C. Zhang, *J. Appl. Phys.* **89**, 6793, (2001)

[58] J. Grollier, V. Cros, H. Jaffrs, A. Hamzic, J. M. George, G. Faini, J. Ben Youssef, H. Le Gall, and A. Fert, *Phys. Rev. B* **67**, 174402, (2003)

[59] I. N. Krivorotov, *et al.* (submitted to *Phys. Rev. B* **,**, M, (a)rch 2007)

[60] M. L. Polianski and P. W. Brouwer, *Phys. Rev. Lett.* **92**, 026602, (2004)

[61] S. I. Kiselev, J. C. Sankey, I. N. Krivorotov, N. C. Emley,

[62] W. H. Rippard, M. R. Pufall, S. Kaka, S. E. Russek, and T. J. Silva, *Phys. Rev. Lett.* **92**, 027201, (2004)

[63] J. C. Slonczewski, U.S. Patent No 5,695,864 (1997)

[64] W. H. Rippard, M. R. Pufall, S. Kaka, T. J. Silva, and S. E. Russek, *Phys. Rev. B* **70**, 100406(R), (2004)

[65] Ya. B. Bazaliy, B. A. Jones, and S.-C. Zhang, *Phys. Rev. B* **69**, 094421, (2004)

[66] W. F. Brown, *Phys. Rev* **130**, 1677, (1963)

[67] X. Zhu, J.-G. Zhu, and R. M. White, *J. Appl. Phys.* **95**, 6630, (2004)

[68] K. J. Lee, A. Deac, O. Redon, J.-P. Nozires and B. Dieny, *Nat. Mater.* **3**, 877, (2004)

[69] A. Brataas, Y. Tserkovnyak, and G. E. W. Bauer, *Phys. Rev. B* **73**, 014408, (2006)

[70] J. Grollier, V. Cros, and A. Fert, *Phys. Rev. B* **73**, 060409, (2006)

[71] K. J. Lee and B. Dieny, APS March Meeting Contributed Talk http://meetings.aps.org/link/BAPS.2007.MAR.N14.7 (2007)

[72] A. Fbin, C. Terrier, S. Serrano Guisan, X. Hoffer, M. Dubey, L. Gravier, J.-Ph. Ansermet, and J.-E. Wegrowe, *Phys. Rev. Lett.* **91**, 257209, (2003)

[73] S. O. Demokritov and B. Hillebrands, *Top. Appl. Phys.* **83**, 65, (2002)

[74] S. Tamaru, J. A. Bain, R. J. M. van de Veerdonk, T. M. Crawford, M. Covington, and M. H. Kryder, *J. Appl. Phys.* **91**, 8034, (2002)

[75] M. M. Midzor, P. E. Wigen, D. Pelekhov, W. Chen, P. C. Hammel, M. L. Roukes, *J. Appl. Phys.* **87**, 6493, (2000)

[76] R. Meckenstock, D. Spoddig, D. Dietzel, J. Pelzl, and J. P. Bucher, *Rev. Sci. Instrum.* **74**, 789, (2003)

[77] G. Boero, S. Rusponi, P. Bencok, R. S. Popovic, H. Brune, and P. Gambardella, *Appl. Phys. Lett.* **87**, 152503, (2005)

[78] S. E. Russek and S. Kaka, *IEEE Trans. Magn.* **36**, 2560, (2000)

[79] B. Özyilmaz, A. D. Kent, M. J. Rooks, and J. Z. Sun, *Phys. Rev. B* **71**, 140403(R), (2005)

[80] *Mechanics* (Pergamon, Oxford, 1976), Sec. 29

[81] S. Kaka, M. R. Pufall, W. H. Rippard, T. J. Silva, S. E. Russek, and J. A. Katine, *Nature* (London) **437**, 389, (2005)

[82] F. B. Mancoff, N. D. Rizzo, B. N. Engel, and S. Tehrani, *Nature* (London) **437**, 393, (2005)

[83] N. C. Emley, I. N. Krivorotov, O. Ozatay, A. G. F. Garcia, J. C. Sankey, D. C. Ralph, and R. A. Buhrman, *Phys. Rev. Lett.* **96**, 247204, (2006)

[84] R. Watts, D. K. Wilkinson, I. R. Barkshire, M. Prutton, and A. Chambers, *Phys. Rev. B* **52**, 451, (1995)

[85] L. Berger, *Phys. Rev. B* **59**, 11465, (1999)

[86] J. Mathon and A. Umerski, *Phys. Rev. B* **63**, 220403, (2001)

[87] W. H. Butler, X.-G. Zhang, T. C. Schulthess, and J. M. MacLaren, *Phys. Rev. B* **63**, 054416, (2001)

[88] S. S. P. Parkin, C. Kaiser, A. Panchula, P. M. Rice, B. Hughes, M. Samant, and S.-H. Yang, *Nat. Mater.* **3**, 862, (2004)

[89] S. Yuasa, T. Nagahama, A. Fukushima, Y. Suzuki, and K. Ando, *Nat. Mater.* **3**, 868, (2004)

[90] Y. Huai, F. Albert, P. Nguyen, M. Pakala, and T. Valet, *Appl. Phys. Lett.* **84**, 3118, (2004)

[91] G. D. Fuchs, N. C. Emley, I. N. Krivorotov, P. M. Braganca, E. M. Ryan, S. I. Kiselev, J. C. Sankey, D. C. Ralph, R. A. Buhrman, J. A. Katine, *Appl. Phys. Lett.* **85**, 1205, (2004)

[92] M. Hosomi, H. Yamagishi, T. Yamamoto, K. Bessho, Y. Higo, K. Yamane, H. Yamada, M. Shoji, H. Hachino, C. Fukumoto, H. Nagao and H. Kano, *IEDM Technical Digest, IEEE Internation* p. 459, 5-7 Dec. (2005)

[93] G. D. Fuchs, J. A. Katine, S. I. Kiselev, D. Mauri, K. S. Wooley, D. C. Ralph, and R. A. Buhrman, *Phys. Rev. Lett.* **96**, 186603, (2006)

[94] J. C. Slonczewski, *Phys. Rev. B* **39**, 6995, (1989)

[95] I. Theodonis, N. Kioussis, A. Kalitsov, M. Chshiev, and W. H. Butler, *Phys. Rev. Lett.* **97**, 237205, (2006)

[96] P. M. Levy and A. Fert, *Phys. Rev. Lett.* **97**, 186603, (2006)

[97] J. C. Sankey, P. M. Braganca, A. G. F. Garcia, I. N. Krivorotov, R. A. Buhrman, and D. C. Ralph, *Phys. Rev. Lett.* **96**, 227601, (2006)

[98] J. C. Slonczewski, J. Z. Sun, *J. Magn. Magn. Mater* **310**, 169, (2007)

[99] A. D. Kent, B. Özyilmaz. and E. del Barco, *Appl. Phys. Lett.* **84**, 3897, (2004)

[100] K. J. Lee, O. Redon, and B. Dieny, *Appl. Phys. Lett.* **86**, 022505, (2005)

[101] H. Kubota, A. Fukushima, Y. Ootani, S. Yuasa, K. Ando, H. Maehara, K. Tsunekawa, D. D. Djayaprawira, N. Watanabe, and Y. Suzuki, *Appl. Phys. Lett.* **89**, 032505, (2006)

[102] A. A. Kovalev, G. E. W. Bauer and A. Brataas, *Phys. Rev. B* **75**, 014430, (2007)

[103] J. N. Kupferschmidt, S. Adam, and P. W. Brouwer, *Phys. Rev. B* **74**, 134416, (2006)

[104] G. D. Fuchs, I. N. Krivorotov, P. M. Braganca, N. C. Emley, A. G. F. Garcia, D. C. Ralph, and R. A. Buhrman, *Appl. Phys. Lett.* **86**, 152509, (2005)

[105] M. A. Zimmler, B. Özyilmaz, W. Chen, A. D. Kent, J. Z. Sun, M. J. Rooks, and R. H. Koch, *Phys. Rev. B* **70**, 184438, (2004)

[106] C. Bilzer, T. Devolder, J.-V. Kim, G. Counil, C. Chappert, S. Cardoso and P. P. Freitas, *J. Appl. Phys.* **100**, 053903, (2006)